6-5-2014

Remote Sensing Suspended Sediment Concentration in the Yellow River

Liqin Qu
liqin.qu@uconn.edu

Remote Sensing Suspended Sediment Concentration in the Yellow River

Liqin Qu, Ph.D.

University of Connecticut, 2014

ABSTRACT

This study aimed to develop an approach to use publicly accessible satellite imagery to quantify the suspended sediment concentration (SSC) in the Yellow River. The suspended sediment in the river affects to the hydrologic, geomorphologic, and ecologic functioning of river floodplains. Commonly used sampling methods are time consuming, labor intensive, and provide only point data. Current studies using remote sensing have focused mild waters (*e.g.* coastal, estuarine, lagoon, lakes and reservoirs) from where the method developed might not be appropriate for highly turbid inland waters. A laboratory spectrum experiment was conducted to investigate the reflective nature of sediment-laden water and the impact of sediment types on the reflectance. A spectral mixing algorithm based on a spectral linear mixture modeling approach was developed to estimate SSC from reflectance. We found that the models based on the spectral mixing algorithm were able to estimate SSC as high as 20 g/l. A field survey with on-site spectral and SSC measurements was conducted between the river channel and Sanmenxia reservoir on the Yellow River. The results confirmed an exponential relationship between SSC and reflectance. A single-band model was built to estimate SSC using band setting same as the band 4 of Landsat 7 image (760-900 nm)($R^2 = 0.92$, RMSE=0.241 g/l). The application of the spectral mixing approach to the on-site showed that the models based on the spectral mixing

algorithm were performed as better as the single band exponential model ($R^2 = 0.86$, RMSE=0.280 g/l) but the valid range for application was improved from 1.99 g/l to 347 g/l.

The spectral mixing algorithm was also applied to the Landsat-7 ETM+ data for remote sense the SSC in the Yellow River. For calibration and validation purpose, the daily SSC measured by the Yellow River Hydrological Monitoring System were associated with Landsat-7 ETM+ imagery from 1999 to 2010. The results showed that the model based on the spectral mixing algorithmcould obtain a more promising relationship ($R = 0.71$) between SSC and reflectance than the conventional regression of a particular band (max $R = 0.62$). This study provides remote sensing method to estimate SSC with ready-to-use parameters for using Landsat-7 ETM+ imagery in the Yellow River. It could also provide spectral reference for remote sensing SSC in other highly turbid inland rivers.

Remote Sensing Suspended Sediment Concentration in the Yellow River

Liqin Qu

Ph.D. China Agricultural University 2008

B.S. China Agricultural University 2003

A Dissertation

Submitted in Partial Fulfillment of the

Requirements for the Degree of

Doctor of Philosophy

at the

University of Connecticut

2014

APPROVAL PAGE

Doctor of Philosophy Dissertation

Remote Sensing Suspended Sediment Concentration in the Yellow River

Presented by

Liqin Qu, B.S., Ph.D.

Major Advisor _____
Xiusheng Yang

Associate Advisor _____
Daniel Civco

Associate Advisor _____
John Clausen

Associate Advisor _____
Thomas Meyer

Associate Advisor _____
Guiling Wang

University of Connecticut

2014

ACKNOWLEDGMENTS

This work could not have been completed without the assistance of many institutions and individuals. The laboratory experiment and field survey was conducted with support of the Alexander Goetz Instrument Support Program from ASD *Inc*.

I would like to express special thanks to all the members of my committee for the hours of hard work that they put into this effort. Dr. Xiusheng Yang, my advisor, gave me the opportunity to study here and encouraged me for a career in research. It has made all the difference. I offer my deepest gratitude for his ongoing support and his patience during what mush have seemed a study without end. Many thanks to Dr. Daniel Civco, he helped me design the study and provide advice and guidance during data analysis and thesis writing. His help in applying the support from ASD *Inc* was critical to the completion of this project. Dr. Thomas H. Meyers was extremely kind and patient in discussing methodological details with me and in feeding my quires. I benefited tremendously from his understanding of mathematical thinking, and from his patience to introduce me to Latex, Mathematica, and other cool stuffs. I would also like to give special thanks to Dr. John C. Clausen for his guidance during the critical phase of the writing. His appreciation of the value of qualitative data and his insight into the process of hydrology all greatly enhanced the final product. Thanks Dr. Guiling Wang offered important insights on the design of the laboratory experiment. Although Dr. Tingwu Lei in China Agricultural University is not my advisory committee, he has always been a source of support and advice.

I would also like to extend my thanks to other faculty members and staffs in the Department of Natural Resources and the Environment for all their support and encouragement. Dr. Tracy Rittenhouse is the first person outside my Committee who has read my manuscript and offered comments. Her valuable comments improved the writing of the section she read and also provided me inspirations for further revision. Dr. Richard Anyah always kept his door open for me and showed great interests in my research work. I am grateful to Beth and Suzie throughout my study for the excellent logistical support and sustaining encouragement they offered.

I am extremely fortunate to have a wonderful group of colleagues who delighted in discussion. Jason Parent, Qian (Rachael) Lei are the GIS experts who I could always be helped by. When I have statistical questions, smart Zhao Xue was always there with answers. David Rosa, Kersey Lawrence, and Alexander Pivarnik were great for advice on writing and they always cheered up for my progresses.

Many people in China rendered invaluable assistance to me. This long list includes the staff of State Key Laboratory of Soil and Erosion and Dryland Farming in China, the graduate students in Prof Leis group in China Agricultural University, and ongoing support from Dr. Xinxiao Yu, Dr. Zhongbao Xin in Beijing Forest University. I highly appreciated invaluable help from Mr. Jun Zhao and Ms. Shaohua Huangin in setting up a laboratory experiment. Dr. Shumei Zhou and Dr. Yiqing were the joyful and creative companions in the experiment and fieldwork, and their support was essential for success of the laboratory study. Special thanks to Mr. Xinwu Tu in the Hydrology and Water Resources Bureau of Sanmenxia Reservoir Region for help me in setting up the field work and collecting the hydrological data, who also enriched my understanding of hydrological monitoring and culture about the Yellow River through his own unique perspective.

I would also like to extend my thanks to my friend Dong Zhao, Dr. Rui Mei, Dr. Ying Wang, Mingming Xia, Wenqiang Bao, Dr. Yuntao Dong, Anwesha Chakrabarti, Radhika Shiradkar, Premika Srinivasan, and Li Zuo, who supported with the help in writing and baby sitting, comforted me at hard time, and incented me to strive towards my goal.

Finally, I am truly indebted to my family that is my end and my beginning. Words cannot express how grateful I am to my mother, father, mother-in-law, father-in-law, brother, sister-in-laws for all of the sacrifices that they have made on my behalf. Their best wishes and concrete supports for me was what sustained me thus far. My husband, Xuejun Zhang, has remained patient and supportive throughout this very long process. He was always my support in the moments when there was no one to answer my queries. In the end, I would like to thank my son Jason for being an amazing companion to transform the hardship to joyful moments.

Contents

List of Figures

List of Tables

Chapter 1

Introduction

The objective of this study is to develop the remote sensing approach to quantify the suspended sediment concentration (SSC) in highly turbid Yellow River flow. Specifically, it includes:

Chapter 2: Quantifying Suspended Sediment Concentration in River Flow Using Remote Sensing Techniques: A Review

Suspended sediment is the most common pollutant in river systems. Quantification of suspended sediment in rivers is important in studying the hydrologic, geomorphologic, and ecologic functioning of river flood plains and deltas. The traditional measurements of suspended sediment concentration (SSC) in rivers are time consuming and labor intensive, and results are often limited to point locations. Satellite remote sensing can provide retrospective and spatial information of suspended sediment concentration. Various visible and NIR band combinations have been proposed as SSC indicators in coastal, estuarine, lagoon, lake and reservoir environments. Recent advances in satellite technology, sensory, image quality, and data accessibility

have made the remote sensing approach very promising in quantifying SSC in highly-turbid inland waters. This study was aimed to provide a systematic review on the use of remote sensing in quantifying SSC for inland waters, covering the basic theoretical considerations, widely accepted empirical models and semi-empirical models, effects of soil and water properties on model performance, developments in sensors, and applications of the technology in various environmental conditions. Currently, the empirical model is still the most widely used tool to infer SSC from remotely sensed data. Mechanistic models are increasingly being developed to make the technology applicable to highly turbid Case II and Case III waters with complex sediment compositions. With the rapid advances in satellite remote sensing technology, such mechanistic models (semi-empirical in nature) are expected to gain more attentions. More studies are called for evaluating the effects of sediment and water properties on the performance and more surface data are demanded for calibration and validation of the models.

Chapter 3: Spectral Mixing Algorithm for Quantifying Suspended Sediment Concentration (SSC) in the Yellow River: Simulation based on Controlled Laboratory Experiment

We investigated the upper limit of suspended sediment concentration (SSC) with respect to the relationship between SSC and reflectance to develop an SSC remote sensing model for the highly-turbid Yellow River. An SSC quantification model was generated by using the spectral mixing index of sediments in water and sediment mixtures. In this study, laboratory experiments were made to measure the spectral curves of sediment-laden water with a high-resolution spectroradiometer. River-bed deposited sediments from two sites, one on the Yellow River at Huayuankou (HYK) and the other on the Wei River at Yangling (YL), and their sand, silt and clay parti-

cle groups were used for laboratory experiments to measure the spectral responses of sediment laden water. The correlation analysis depicted stable correlation between SSC and reflectance at wavelengths ranging from 450 nm to 1000 nm, in which, spearman rank correlation coefficient (r_s) for all sediments were above 0.7 while the HYK natural sediment had Spearman coefficients exceeded 0.9. Experimental results revealed the curves of the relationship between SSC, up to 40 g/l. A physical-based exponential model ($R^2 > 0.9$) at each simulated Landsat band effectively interpreted the relationship between SSC and reflectance. The highest upper limit SSCs at 21 g/l and 15 g/l in natural YL and HYK sediments, respectively, were observed in Landsat Band 4. A spectral mixing algorithm was used to build the model and estimate the SSC from reflectance at correlated wavelength bands . The spectral mixing algorithm can generate a uniform model that disregards the effects of sediment type by adopting the reflectance curve at the upper-limit SSC to represent the standard reflectance of sediment. This study is useful in understanding the spectral characteristic of high SSC in water and in applying remote sensing techniques to monitor SSC in the Yellow River.

Chapter 4: Estimation of Suspended Sediment Concentrations by Spectral Reflectance: a Field Spectral Survey on the Yellow River

The dynamic sediment distribution on large rivers with dams constructed often attract wide attention due to their possible adverse environmental impacts. Sedimentation modeling and environmental consequence of man-made projects are often hindered by the lack of sediment measurements with spatial details. This study aimed to investigate the method to estimate the suspended sediment concentrations (SSCs) from on-site spectral measurements. The study investigated the spectral signature of river water from the natural channel and Sanmenxia reservoir on the Yellow River. A field

spectral survey was conducted with on-site spectral measured by a spectraoradimeter and SSCs by sampling. Reflectance at 750 nm to 950 nm, with all r between SSC and reflectance being above 0.7, seemed to be the proper range for SSC estimation. Simulated Landsat ETM+ band 4 (760 nm to 900 nm) was employed to build the single band model for estimating SSC. The result confirmed that the exponential model based on the relationship between SSC and reflectance ($R^2 = 0.92$, RMSE=0.241 g/l) were better than the linear model between reflectance logarithm transformed SSC ($R^2 = 0.90$, RMSE=0.310 g/l). We also apply the Spectral Mixing Algorithm (SMA) from the tank experiment to the on-site spectral measurements. The result shows the SMA models were performed as better as the single band exponential model ($R^2 = 0.86$, RMSE=0.280 g/l) but the valid range for application was improved from 1.99 g/l to 347 g/l. This study could provide critical instructional assistance for estimating SSC directly from remote sensing data.

Chapter 5: Estimation of Suspended Sediment Concentrations in the Yellow River using Landsat ETM+: Application of a Spectral Mixing Algorithm

Using remote sensing to estimate suspended sediment concentrations (SSC) in inland waters has been less successful than for oceanic, coastal, and lake waters. In this study, we developed a spectral mixing algorithm for quantifying SSC in highly turbid inland waters. The daily SSC measurements from the field monitoring and satellite data from Landsat 7 ETM+ were used for developing an spectral mixing algorithm to remotely sense SSC in the Yellow River. The results showed that the relationship between SSC and an integrated spectral mixing index of sediment (SMI_s) that was derived from reflectance by using the spectral mixing approach, was more accurate and applicable than those from the conventional regression methods ($r = 0.71$ vs.

$r = 0.62$, respectively). Our study indicated that the consideration of the two primary components (water and sediment) in spectral mixing algorithm was adequate to estimate SSC in the Yellow River. Our study also showed that the satellite image-derived standard reflectance spectra of reference natural clean water could reduce the effect from lack of information on phytoplankton. We also used a spectral mixing algorithm based remote sensing approach to map out the SSC along the river for different seasons. These results indicated a high potential for the spectral mixing algorithm in effectively separating contribution of different primary components on the total reflectance.

Chapter 2

Quantifying SSC in River Using Remote Sensing Techniques: A Review

2.1 Introduction

Sediment concentration and its distribution are essential for studying the interrelationships among physical, chemical, biological, and environmental processes in river systems. Suspended sediment concentration (SSC) that describes the amount of solid material suspended in water-sediment mixture, usually expressed in milligrams per liter (mg/l), is a common measure of sediment transport in overland and river flow. The terms SSC and total suspended solids (TSS), also referred to as suspended particulate matter (SPM)(Ouillon et al., 2008), are often used interchangeably in the literature. SSC data are produced by measuring the dry weight of all the sediments from a known volume of water-sediment mixture. The TSS data can be produced by

various methods, most of which entail measuring the dry weight of sediment from a known volume of a subsample of the original (Gray et al., 2000). In general, when all other factors are kept the same (such as particle density and composition), the analytical procedures may result in different values for SSC and TSS, with the SSC being a little higher than TSS (Gray et al., 2000). Another related definition is the suspended sediment flux (SSF) that is the product of velocity and suspended sediment concentration (SSC) (Pang et al., 2011). In this paper, we use the term SSC to represent solid-phase material suspended in a water-sediment mixture.

Globally, in situ sampling and laboratory analysis are the most commonly used method for sediment observation (Edwards and Glysson, 1988). This method involves site selection, water sampling, transportation of the samples, laboratory processing (drying and weighing, for example), and post analysis. It is time consuming, labor intensive, and provides only point data at gauging stations. Because the construction of gauging stations and the maintaining of a monitoring system is costly, it has been estimated that three quarters of the world cannot afford a full-scale monitoring infrastructure for water quality control and will not be able to construct this infrastructure in the near future (GEMS, 2003; Villar et al., 2012). Wren et al. (2000) provided a detailed review on the field techniques for suspended-sediment measurement with emphasis on new technologies for SSC measurement including acoustic method, pumping sampling, laser diffraction method, nuclear method, and methods based on focused beam reflectance, optical backscattering, optical transmission, and spectral reflectance. Although some new technologies have been used with varying degrees of success, most of them were only successful in laboratory or for a small catchment. High cost of facility and maintenance discourages the implementation of hydrological monitoring networks to provide long-term, large scale, and uninter-

rupted observations, which are needed for soil erosion and water quality studies under increasing natural and anthropogenic changes all over the world.

Recently, remote sensing technology has been used for SSC measurement and shown potential in providing synoptic, continuous and long-term global observation. Various visible and NIR band combinations have been proposed as SSC indicators on coastal, estuarine, lagoon, lake and reservoir environments. Recent advances in satellite technology, sensory, image acquisition and processing, and data accessibility have drawn much attention in using remote sensing approach in determining SSC, especially in highly-turbid inland waters. This paper summarizes the current developments in using remote sensing technology in quantifying SSC for inland waters, focusing on the theoretical considerations and application potentials of this emerging method.

In the perspective of remote sensing, waters can be generally divided into different classes (Morel and Prieur, 1977). Case I waters are those dominated by phytoplankton (e.g. open oceans). Case II refers to such waters that contain not only phytoplankton, but also other constituents such as suspended sediments, dissolved organic matters, and anthropogenic substances. The extremely turbid waters are referred to as Case III waters, which have not been widely studied (Stumpf and Pennock, 1991). In this paper, we focus on Case II and Case III waters, especially the river water with relatively high SSC.

The early studies in remote sensing of SSC was mainly focused on discovering and demonstrating the existence of connections between suspended sediments and spectral reflectance, on which empirical methods are based (Ritchie et al., 1987; Ritchie and Cooper, 1988; Ritchie et al., 1990; Chen et al., 1992; Harrington Jr et al., 1992; Schiebe et al., 1992).

Most documented relationships between spectral reflectance and SSC in surface waters are linear. Ritchie et al. (1976) found a linear correlation ($R = 0.85$) between integrated spectroradiometer reflectance ($700 - 800\ nm$) and amounts of SSC in Mississippi reservoirs. Curran et al. (1987) analyzed spectral radiance recorded by an airborne multispectral scanner and found a positive correlation between SSC and radiance. Chen et al. (1991) found that the relationship between SSC and reflectance was log-linear at wavelengths of 450 to 700 nm and linear at wavelengths of 700 to 1050 nm. Novo et al. (1991) reported that, for oxisol sediment, the relationship between total suspended solid concentration and reflectance was linear and constant from 450 to 900 nm. Chen et al. (1992) examined the usage of derivative reflectance spectra in estimating SSC and recommend using the derivative spectra for the estimation of SSC when continuous spectra are available. In their study, there was a strong inverse correlation between SSC and derivative spectral reflectance both in the laboratory (max $R^2 = 0.98$) and at sea (max $R^2 = 0.83$), and the error in SSC estimates using derivative spectral reflectance in laboratory was less than 8% of the mean value.

In order to use satellite imagery in quantifying SSC, the relationships between the integrated data of satellite band/bands and sediment concentration in surface waters have been investigated (Han and Rundquist, 1994; Lodhi et al., 1998). Harrington Jr et al. (1992) reported that reflectance at Landsat MSS 3 (NIR) is linearly related with SSC within the range of $0 - 500 mg/l$, but the relationship became nonlinear at higher SSC. Wang and Lu (2010) found that water reflectance of MODIS Band 2 (841 to 876 nm) has a linear relationship with SSC within the range of $74 - 600 mg/l$ and a nonlinear relationship in the range of $600 - 881 mg/l$. In addition to single bands, ratios of reflectance in NIR to visible band (red, green and blue), and that in red to

green band, have also been proposed to estimate SSC Topliss et al. (1990); Yuming and Min (1992); Doxaran et al. (2009). Doxaran et al. (2002) pointed out that use of reflectance ratios could reduce the effects of sky reflection, particle size, and refractive index variations. However, Binding et al. (2005) argued that reflectance ratios worked well only for highly turbid waters where scattering is sufficient to overcome the strong absorption by other optically active materials in water at these wavelengths.

2.2 SSC Remote Sensing Models

The essential part for quantifying SSC using remote sensing approach is the model that infers SSC from satellite sensing information. From the perspective of radiation transfer, the satellite sensing information, such as the radiance, reflectance coefficients, and diffuse attenuation, are apparent optical properties (AOPs) and they depend on the medium and the geometric structure of the source fields. The parameters that depend only on the substances comprising the water mass but not the geometric structure of the various light fields are inherent optical properties (IOPs), such as the absorption and the scattering coefficient (Mobley and Mobley, 1994). Theoretically, when the inverse of the radiative transfer equation (RTE) is applied to local radiometric spectra in quantifying SSC, the inherent optical properties (IOPs) are also needed.

In general, models for remote sensing of SSC can be classified as empirical or semi-empirical (Ma and Dai, 2005). Empirical models normally establish the relationship between AOP and SSC directly by statistical analysis on data (such as linear and nonlinear regression). Semi-empirical models are also based on radiation theory that

integrates IOPs with AOPs (Ma et al., 2006a,b).

2.2.1 Empirical models

According to Curran and Novo (1988) and Ritchie et al. (2003), the empirical models in general take the following forms:

$$Y = A + BX \tag{2.1}$$

$$Y = A + B \ln X \tag{2.2}$$

$$\ln Y = A + BX \tag{2.3}$$

$$\ln Y = A + B \ln X \tag{2.4}$$

where X is the spectral measurement from remote sensing or spectroradiometer (i.e., radiance, reflectance, energy), and Y is the water quality parameter of interest, SSC in this study. Specifically, the spectral measurement (X) could be reflectance in a single band, ratio of reflectance in two bands (Bowker and Witte, 1975; Tassan and Sturm, 1986; Topliss et al., 1990; Yuming and Min, 1992; Doxaran et al., 2009), or a linear combination of such parameters (Khorram, 1985; Raaj et al., 2008; Wang et al., 2012). Shown in Table 2.1 to 2.4 are examples of the empirical models in literature for remote sensing SSC in different water bodies.

The existence of a linear or nonlinear relationship between SSC and reflectance is not difficult to explain with the theory of radiation transfer. Without consideration of any atmospheric effect, the reflectance at any wavelength λ, $R(\lambda)$ can be expressed as a function of the optical cross section values of the co-existing concentrations of

pure water and constituents in the water (such as chlorophyll α and dissolved organic carbon). Focusing on suspended sediments, this could be expressed as:

$$R_{(0-,\lambda} = C\frac{b_w(\lambda) + b_m SSC + b_x}{a_w(\lambda) + a_m SSC + a_x} \tag{2.5}$$

where a_w represents the absorption coefficient of water; a_m is the cross section value of absorption coefficient of suspended sediments, a_x is the absorption coefficient of other co-existing constituents; b_w is the backscattering coefficient of water; b_m is the cross section value of the backscattering coefficient of suspended sediments; and b_x is the absorption coefficient of other co-existing constituents. Because backscattering by water is relatively small compared with absorption, the backscattering coefficient can generally be ignored. Then,

$$R_{(0-,\lambda} = C\frac{b_w(\lambda) + b_x}{a_w(\lambda) + a_m SSC + a_x} \tag{2.6}$$

It is reasonable that a linear relationship between reflectance and SSC could be obtained when the SSC is relatively small. In that case, the absorption is dominated by water when a_w is far outweigh $a_m SSC$. With increasing SSC in water, the linear relation will weaken by the contribution of absorption by suspended sediments in water.

In nonlinear models, factors such as suspended particles' size, shape and color can have significant influences on water-sediment optics (Baker and Lavelle, 1984; Stumpf and Pennock, 1989; Kirk, 1984; Sydor and Arnone, 1997). Often a second-order polynomial (Lodhi et al., 1998) or an exponential function model is used to estimate the SSC from spectral data. For example, Schiebe et al. (1992) suggested

an empirical exponential model:

$$R_i = B_i(1 - e^{\frac{c}{S_i}}) \tag{2.7}$$

where R_i is the reflectance (i. e., from Landsat, SPOT digital data) in wave band i, c represents SSC, B_i is the reflectance saturation level at high suspended sediment concentrations in wave band i, and S_i is a reference concentration value at reflectance equal to 63% of saturation in wave band i. With statistically determined coefficients (B_i and S_i), Schiebe et al. (1992) successfully applied this model in estimating SSC in Lake Chicot, Arkansa. In the application, it was mentioned that a theoretical foundation exists for the observed exponential relationship between remotely sensed data and suspended sediment concentration in surface water. However, no further exploration of the theoretical foundation was provided.

Recent studies on spectral mixture modeling (Tyler et al., 2006; Oyama et al., 2007; Matsushita and Fukushima, 2009) and neural networks (Schiller and Doerffer 1999; Panda et al. 2004; for example) have improved the predictability of the empirical models. Zawada et al. (2007) showed that satellite-based observations are useful for inferring TSS in estuarine areas at Chesapeake Bay using a spectra-matching optimization algorithm from Sea-viewing Wide-Field-of-view Sensor (SeaWiFS) satellite imagery. Oyama et al. (2007) developed a spectral decomposition algorithm (SDA) based on a linear spectral mixture modeling approach for estimating chlorophyll α concentrations and non-phytoplankton suspended sediments from multispectral satellite data. This method considers the mixed reflectance spectrum of a given pixel as a linear combination of those three primary components: clear water, non-phytoplankton suspended sediments (NPSS), and phytoplankton. A group of de-

composition coefficients is defined for each component. The decomposition equation can be expressed as:

$$R_(\lambda) = \sum_{i=1}^{n} C_i P_i(\lambda) \tag{2.8}$$

where n is the number of constituents considered, C_i is the decomposition coefficient for constituent i, which directly relates to its mass or concentration, and $P_i(\lambda)$ is the standard wavelength-specific reflectance for constituent i, representing the distinctive spectral pattern or signature. The decomposition coefficient is then used as an independent variable in the model, replacing the single band reflectance, reflectance ratio, or any combination used in conventional empirical models. Oyama et al. (2009) applied this method to estimate chlorophyll α and NPSS, in which the SDA based model was shown to be superior to conventional empirical models. An artificial neural network model was developed and successfully applied in evaluation of SSC in Hangzhou Bay, China using MODIS derived radiances (Wang et al. 2009; Wang et al. 2012). The results indicated that application of artificial neural networks technique with one hidden layer appeared to yield better results ($R^2 = 0.98$; $n = 25$) compared with a conventional regression model.

The biggest advantages of empirical models are the simplicity and rapidity in data processing, which are necessary for processing large data sets such as satellite images. However, due to the nature of regression, it is generally only applicable to waters with characteristics similar to those used in the model development. The applicability of remote sensing approach based on empirical relations can be quite limited and may result in significant errors if not used properly.

2.2.2 Semi-empirical Models

Over the past decades, the increased spectral and spatial resolution of remote sensors have encouraged the investigation on using new techniques for monitoring Case II waters such as rivers and lakes. The availability of high resolution data promote improvements in models based on radiative transfer theory and estimation of IOPs (Stumpf and Pennock, 1991; Carder et al., 1993; Doerffer and Fischer, 1994; Hoge and Lyon, 1996; Carder et al., 1999). Dekker et al. (1997) found that the following reflectance model is more accurate for turbid waters:

$$R_{(0-)} = F\frac{b_b}{a + b_b} \tag{2.9}$$

where $R_{(0-)}$ is the subsurface irradiance reflectance of water, a is the absorption coefficient and b_b is the backscattering coefficient of water. The parameter F is comprised of the reflectance and transmittance properties of the water surface, which was found to be much more variable for inland waters than for coastal and ocean waters.

Eleveld et al. (2008) presented a single band algorithm for estimating near-surface suspended particulate matter (SPM) concentrations derived by parameterizing Gordons approximation of the radioactive transfer model for turbid Case II waters of the southern North Sea ($R^2 = 0.87$). The semi-analytical model of Lee et al. (1998, 1999), based on a study of Maritorena et al. (1994), Maritorena et al. (1994), has shown promise in determining SSC along water depth. Santini et al. (2010) fine-tuned a physical model for the highly turbid Venice lagoon waters. In their study, an inverse method based on a two-step optimization procedure was developed to determine water quality parameters from remotely sensed hyperspectral data. In the first step,

they linearized a non-linear analytical relationship between water optical properties and remote sensing data. In the second step, they used the results of the linearized formulation as initial values in a non-linear least squares-based evaluation. Volpe et al. (2011) developed a semi-empirical model based on radiative transfer theory to relate satellite radiance measurements and in situ turbidity observations at Venice lagoon. Kilham et al. (2012) proposed a theoretical approach to estimate SSC using remote sensing data, which accounts for the effects of particle-size distribution of sediments suspended during floods and the dominant mineralogy. The estimations of the proposed model produced errors less than $10mg/l$, which was within the error range of field measurements. Their study suggested that semi-emipirical models based on optical theory and radiative transfer are promising for quantifying SSC in rivers during flood conditions when empirical relationships are mostly no longer valid. Several approaches with different degrees of complexity have also been proposed for inverting the RTE (radiative transfer equations) for semi-empirical models, including look-up tables and polynomial interpolations.

In general, the accuracy of semi-empirical models is better than that of empirical algorithms (Bukata et al., 1995), and these models are more applicable for different water types with the capability to take the effects of water depth, particle size, and water-air interface into account. The predictability of semi-empirical models depends on the estimation of IOPs for sediment substances. The IOPs are determined by types of sediment, depth of water and other factors that affect the relationship between SSC and remotely sensed spectral optical properties (Curran and Novo, 1988). Because IOPs are constituent specific and are sensitive in simulation of RTE, the performance of most semi-empirical methods relies on accurate determination of the radiative properties of sediment constituents.

The fundamental IOPs of water such as volume attenuation, absorption, and backscattering coefficients can be obtained from actual measurements or analytical models. The attenuation and absorption coefficients are measurable with spectrometers (ac-9 WET labs) or double-beam spectrophotometers (Dekker et al., 2002), and the backscattering coefficients can be determined with a Hydroscat 6s sensor (Hobi Labs Inc.) (Santini et al., 2010). IOPs not readily measurable as the sub-surface irradiance reflectance $R_{(0-)}$ can, in certain cases, be inferred from a combination of field spectro-radiometric data. A detailed description of the determination of IOPs was provided by Mobley and Mobley (1994).

The analytical models of IOPs can be constructed by considering contributions from a number of components, such as:

$$a = a_0 + \sum_{j=1}^{n} a *_j C_j \tag{2.10}$$

$$b = b_{b0} + \sum_{j=1}^{n} b *_{bj} C_j \tag{2.11}$$

where $a*_j$ and $b*_{bj}$ represent the absorption and backscattering coefficients, respectively, per unit concentration of constituent j, a0 and bb0 are the coefficients for pure water, and C_j is the concentration of the j^{th} constituent.

The absorption coefficient and backscattering coefficient for both dissolved water and clear water have been studied by various researchers (Smith and Baker, 1981; Buiteveld et al., 1994; Morel and Maritorena, 2001; Morel et al., 2007). Many studies have also reported on the inherent optical properties for waterborne substances such as colored dissolved organic matter CDOM (Lee et al., 2002; Mannino et al., 2008; Zhu et al., 2011), phytoplankton (Roeslerl and Perry, 1995; Bri), and sediment (Dekker

et al., 2001; Doxaran et al., 2002; Onderka and Rodný, 2010).

It is noteworthy that the IOPs could also be applied in an empirical relationship to improve accuracy or robustness of the model. Binding et al. (2005) observed a strong relationship between irradiance reflectance at 665 nm and mineral suspended sediment concentrations (MSSC) in the Irish Sea ($R^2 = 0.918$), and found that the relationship varied with changes in the mass-specific scattering coefficient caused differences in particle properties such as grain size and composition. Santini et al. (2010), using a non-linear analytical relationship between water optical properties and remote sensing reflectance, refined an existing model for the highly turbid Venice lagoon waters. Lorthiois et al. (2012) also reported that the particulate backscattering coefficient (b_{bp}) is a robust proxy of SPM concentration in a river plume ($b_{bp}(770) = 0.0076 \times SPM$, $R^2 = 0.80$, $n = 56$).

2.3 Effects of Sediment, Water, and View Geometry

The relationship between remotely sensed radiative properties and SSC is affected by many parameters of sediment composition (such as type and size distribution), water body (depth, vertical variation in sediment concentration, and bottom reflection, for instance), and view geometry. To some degree, the air-water interface and atmospheric conditions also add to the complexity (Novo et al., 1989b,a; Bhargava and Mariam, 1991; Chen et al., 1992; Han and Rundquist, 1994; Gray et al., 2000; Schmugge et al., 2002).

Novo et al. (1989b) conducted a laboratory study on the effect of sediment type on reflectance. They found that the strength of the relationship was affected by sediment

type, and the reflection of fine (white) sediment was much different from that of coarse (red) sediment. Han and Rundquist (1996) compared the standard reflectance spectra generated from two texture types of clay soil and found that the increase in reflectance was greater for fine soil than for coarse soil. Bhargava and Mariam (1991, 1990) investigated the impact of sediment type and size on reflectance, and reported that reflectivity increases with a decrease in particle size. They also found that there was a linear relationship between turbidity and reflectance for bentonite clay and black cotton soil, but a curvilinear association for kaoline and gray soil. Lodhi et al. (1997a) studied the application of remote sensing technology for suspended loess soils in surface waters and found that the visible spectral range of 580 to 690 nm provided the most information on the type of suspended sediments, but it was the NIR spectral range of 714 to 880 nm that produced best estimates of the amount of suspended sediment in surface waters. Binding et al. (2005) studied the relationship between irradiance reflectance and mineral suspended sediment (MSS) concentrations in the Irish Sea, and found that the variability in the reflectance-MSS relationship was related to the changes in the mass-specific scattering coefficient caused by particle size and composition.

Compared to field measurements or simulations with numerical models, the image-derived SSC represent only the concentration of suspended sediment within a surface layer. A depth-integrated load of SSC necessitates the understanding of the impact of water depth. There are a few studies in the literature on the effects of water depth, substrate type, suspended concentration and surface turbulence by remote sensing of river channel morphology (Legleiter et al., 2009, 2004, 2011). Future studies along these directions are anticipated to provide more information regarding the effect of water body on SSC modeling.

The view geometry also affects the relationship between remotely-sensed reflectance and SSC (Novo et al., 1989a; Ferrier, 1995). Han and Rundquist (1994) investigated the effect of view geometry on responses of underwater light field and surface reflectance to varying SSC. Ferrier (1995) demonstrated the effectiveness of using a polarizing filter to remove the variation in the SSC-reflectance relationship due to changing the viewing angle and particle shape. In a recent study, Santini et al. (2010) also shaped an underwater light field through an analytical formulation of radiative transfer and numerical simulations.

Study attentions are also paid to account for transmittance across the air-water boundary (Mobley and Mobley, 1994). For most of the empirical models, it is unnecessary to account for the impact from air-water interface effects. For semi-empirical models, this could be estimated by RTE tools such as Hydrolight software.

2.4 Remote Sensors

The quantity and quality of the remote sensor are essential for the success of SSC remote sensing methods. Over the past 30 years, many satellite and airborne sensors have been developed to gather information on the biological activities occurring within water body. Although ocean color sensors such as Coastal Zone Color Scanner (CZCS), the Sea-viewing Wide Field-of view Sensor (SeaWiFS) have short revisit times with high spectral resolution and sensitivity, the spatial resolution($> 1km$) is typically too coarse to describe inland water features adequately. The Landsat series ($30m$) and the Moderate Resolution Imaging Spectroradiometer (MODIS) ($250m$) are more commonly used in surface water quality studies.

Most investigators take advantage of Landsat for its longest time series and the free data accessibility. Landsat satellites were the firstly equipped with Multispectral Scanners (MSS), with four bands that cover the green to near infrared (NIR) portion of the spectrum ($500 - 1000\ nm$) at $80m$ resolution. Later Landsat satellites have Thematic Mapper (TM) and Enhanced TM (ETM) sensors onboard with improved resolution (spatial resolution of 30 m) and more spectral bands (Vrieling, 2006). MSS data are able to generate reliable estimates of suspended sediment concentrations between $50 - 250\ mg/l$, beyond which under-estimation has been a problem (Ritchie and Cooper, 1988; Liu et al., 2003). The improved spectral, spatial, and radiometric resolution for TM and ETM imagery has substantially improved the accuracy of SSC quantification and other water quality parameters such as Secchi disk depth, chlorophyll α concentration, and turbidity (Lathrop 1986).

MODIS is a key instrument aboard the Terra (EOS AM) and Aqua (EOS PM) satellites. MODIS and Terra/Aqua view the entire Earth's surface every 1 to 2 days and thus offer near daily global coverage (`http://modis.gsfc.nasa.gov`). MODIS acquires data in 36 spectral bands, covering wavelength from 400 to 14400 nm. Two bands (Band 1, $620 - 670\ nm$ and Band 2, $841 - 876\ nm$) have a nominal resolution of 250 m at nadir, five bands (Band 3-7 covering $459 to 2155\ nm$) at 500 m, and the remaining 29 bands (bands $8 - 36$) at 1 km. Even for the bands with best spatial resolution, the retrieval reflectance from the river surface using MODIS data is hampered by the low spatial resolution, which may result in few pure (non-mixed) water pixels, depending on the river width and image acquisition geometry. Spectral mixing has been described extensively in the literature and occurs when different materials are present in the same pixel. In the context of this study, spectral mixing may occur among water, vegetation or sand banks. Villar et al. (2012) applied an algorithm to

derive the water end member reflectance in each image with spectral mixing occurring between water and vegetation or sand banks. Because the aerosol information can be retrieved from MODIS image data, it makes MODIS image possible to work with other imagery to conduct atmospheric corrections. With the aid of aerosol information retrieved from concurrent MODIS surveys, Yu et al. (2012) implemented an atmospheric correction for CCD images from a Chinese Satellite system (The environment and disaster monitoring and forecasting small satellite Constellations: HJ-1A/1B satellites).

SPOT, MERIS, EO-1 ALI, IRS (India), HJ-1A/1B (China) and THEOS (Thailand), all with different spectral and spatial-temporal resolutions can also provide synoptic water quality data (Chen et al., 2004). The spectral information for commonly used sensors is shown in Figure 2.1. SPOT data are available in three bands covering green to NIR wavelength (a shortwave IR band was added to SPOT-4 and SPOT-5) at a spatial resolution of $20m$ (SPOT 4) and $10m$ (SPOT 5). The green band is least correlated with water quality parameters, whereas the red band and NIR band are more closely correlated and are more sensitive at a higher level of suspended sediment concentration (Liu et al., 2003) Caution must be exercised in using SPOT data owing to the coarse spectral resolution (finest 70 nm).

The Indian Remote Sensing (IRS) satellite system has one of the largest constellations of remote sensing satellites in operation, with 10 operational satellites currently in orbit. IRS 1C and 1D have identical payloads with a 23.5 m resolution multispectral sensor called LISS-3 that covers visible and NIR.(`http://bhuvan.nrsc.gov.in/bhuvan/content/indian-remote-sensing-satellites-earth-observation-india-high-resolution-satellite-data`).

Avinash et al. (2012) have attempted to develop a site-specific algorithm following

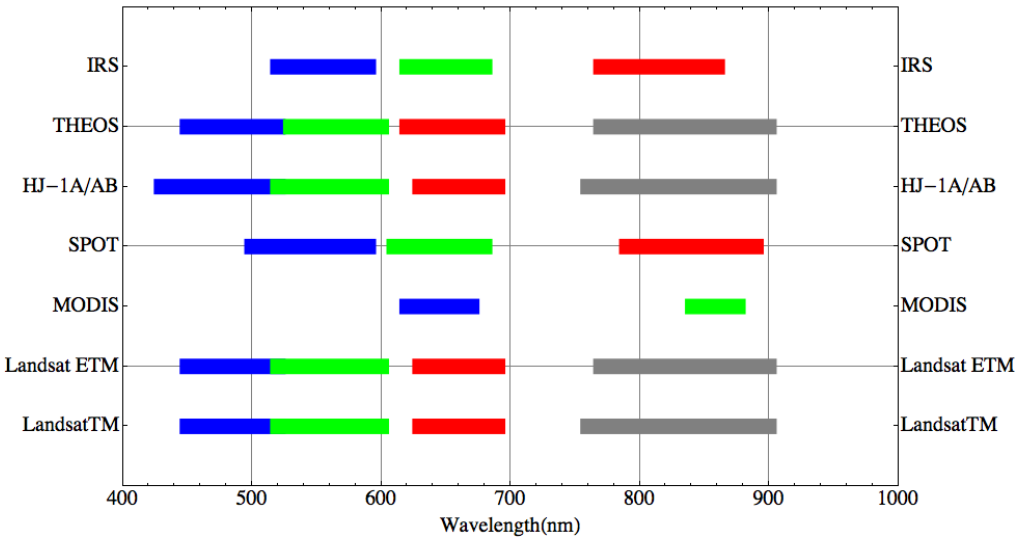

Figure 2.1: Spectral bands and bandwidth of common used satellite

Tassan (1994) in Case II waters off southern Karnataka using IRS-P4 Ocean Color Monitor (OCM) data. The coefficients of the tuned algorithm obtained by the least square fitting yielded significant statistical relationship ($p < 0.05$ at 95% confidence level) between in situ SSC and OCM derived remote sensing reflectance ($R^2 = 0.98$).

The environment and disaster monitoring and forecasting small satellite constellations (HJ-1A/1B satellites), launched by China on September 6, 2008, are equipped with two charge-coupled device (CCD) cameras with the same nadir symmetry, design parameters, and characteristics. The constellation of the two satellites generates multispectral CCD images with a spatial resolution of 30 m and short revisit time of 2 days (`http://www.cresda.com/n16/n92006/n92066/n98627/index.html`). The HJ-1A/1B CCD imagery contains four spectral bands ($430-520\ nm$, $520-600\ nm$, $630-690\ nm$, and $760-900\ nm$) with a scan swath of $360km$ ($700km$ with 2 sensors). Considering the great similarity in the waveband design and spatial resolution between China HJ1A/1B satellites and Landsat TM, Li et al. (2011) conducted a comparative

analysis on data of aspects of track parameter, spectral response characteristics and imaging quality between the two systems, and concluded that HJ1A-CCD1 has a wider threshold value than TM in the blue and red wavebands, but a weaker capability to receive high radiance than TM in the green and near infrared wavebands. Yu et al. (2012) used the HJ-1A/1B (CCD) imagery in monitoring the total suspended sediment (TSS) concentrations in dynamic water bodies of Poyang Lake, the largest freshwater lake in China.

Thailand Earth Observation System (THEOS) payloads Panchromatic and Multispectral push broom scanning optical instruments, which covers four bands (Band 1, $450 - 520\ nm$; Band 2, $530 - 600\ nm$; Band 3, $620 - 690\ nm$; and Band 4, $770 - 900\ nm$) at 15 m resolution and a panchromatic band at 2 m resolution with spectral range from $450 - 900\ nm$. The reception visibility cone of THEOS covers southeast Asian countries, mainland China and east Asian countries enabling Asian users to have a direct and quick access to THEOS images. THEOS image acquisition is performed on users requests (Kaewmanee et al., 2007). Asadpour et al. (2012) studied the precision of a proposed algorithm in achieving total suspended sediment concentration by utilizing THEOS satellite imagery over Penang area, Malaysia and the obtained results were found accurate at $R^2 = 0.97$ and RMSE (root mean square error) $= 7.43\ mg/l$.

2.5 Applications

An increasing number of works have progressed to the next stage of producing maps for providing useful information on hydrological process or dynamics of water systems.

Martinez et al. (2009) quantified the mean annual sediment discharge in the Amazon River as well as it's inter and intra-annual variability using SSC derived from MODIS reflectance data. Chen et al. (2011a,b) applied a MODIS-remote sensing model of TSS concentration for an environmental assessment of the impact of Hurricane Frances in Apalachicola Bay, USA. They examined the sediment re-suspension and distribution in the Bay by comparing TSS concentrations before, during and after a storm. Fang et al. (2010) obtained the spatial distributions of TSS concentration in the Pearl River Estuary, southern China from Earth Observing-1 (EO-1) Advanced Land Imager (ALI) satellite imagery by using the relationships between the reflectance and total suspended solids (TSS) at 549 nm ($R^2 = 0.91$, $P < 0.001$). Pavelsky and Smith (2009), using remotely sensed SSC, estimated the river flow velocity and lake recharge in the Peace-Athabasca Delta, Canada. The remotely sensed SSC was mapped from SPOT and ASTER satellite images based on relationships between in situ SSC and remotely sensed visible/near infrared reflectance. Acker et al. (2004) estimated the neritic sediment mass transport from carbonate platforms for two hurricane-forced events Their study indicated an potential use of remote sensing technology in estimating carbonate flux from coral reefs, banks and atolls as an augmentation to in situ studies. By using SSC from ocean color remote sensing data, Pang et al. (2011) developed a method to realize a 3D suspended sediment flux field. In their study, the suspended sediment concentration at the surface was generated from SeaWiFS remote sensing data, with a local inversion algorithm following Tassants model (Tassan, 1994). Comparison between the retrieval data and in situ measurements showed that the average relative error for SSC estimation was about 25.4%. Warrick et al. (2007) also used 705 water samples from 36 ship-days in combination with MODIS satellite remote sensing, three buoy meteorological observations, 21 drifters, and radar array

current measurements to evaluate the dispersal patterns and dynamics of freshwater plumes (freshwater with suspended sediment) within the Southern California Bight.

Avinash et al. (2012) demonstrated the potential application of a regionally-tuned algorithm to SSC mapping in studying the spatial and seasonal pattern in shallow waters off southern Karnataka. A global empirical SSC algorithm (Tassan 1994) that derives SSC from spectral reflectance at 490, 555 and 670 nm was modified to regional scale by adopting statistical/graphical criteria to characterize the spatial and seasonal distribution of SSC. The results indicated that spatial variation was statistically not significant, and notably higher concentrations have been observed in the near-shore shallow waters in comparison with offshore waters.

Chen and Quan (2012) developed a quantitative integrated remote sensing model for suspended sediment to predict the multi-year averages of suspended sediment concentration in Xiamen Bay. The comparison between model prediction and observed data showed that the multi-year averaged SSC in the study area and the concentration difference between neighboring sites can be predicted by the remote sensing model with an error rate of 21.61% or less, which can satisfy the engineering requirements for channel deposition calculations. Lorthiois et al. (2012) studied the daily and seasonal dynamics of suspended particles in the Rhne River plume based on remote sensing and field optical measurements. The study is regarded as a solid contribution to improve hydrodynamic modeling by incorporating temporal and spatial variations of sediment fluxes based on data from remote sensing.

Apart from pursuing the closeness of the models and the accuracy of quantification, current applications have shown a tendency to apply the remote sensing technology to observe before and after storm variations, and to map the spatial distribution of sediment load. These works have the potential to promote the studies on soil

erosion, water resources management, and ecological functions under naturally and anthropogenically induced climate changes.

2.6 Conclusions

This paper summarized the current development in using remote sensing technology to quantify SSC, especially for inland water. Although the technology has been widely employed in mapping and monitoring sediments in large water bodies (oceans and lakes), the application of remote sensing method to river systems is at its developing stage. Attentions should be paid in the following aspects:

Firstly, inland waters are mostly Case II and Case III waters, and the SSC is typically high and the impacts of sediment type are more significant. Most methods relied upon empirical relationships between sediment concentration and surface water reflectance captured by the remote sensing instrument are hampered by the high turbidity and significant effect of sediment types in Case II and Case III waters. Research needs to focus on understanding the effects of SSC on optical properties of surface waters so that physically-based models can be developed to improve the predictability with remotely sensed data.

Secondly, current studies are generally limited to the application of easy accessible satellite data such as Landsat and MODIS. New satellites (EOS, WorldView etc.), in orbit or being planned to launch are equipped with new sensors (hyperspectral, high spatial resolution) which allow us to discriminate between SSC and other water quality parameters, and consequently, to develop a better understanding of the light/water/substance interactions. Such development encourages us to move further

from empirical approaches to more accurate and adaptable theoretical models.

Lastly, instead of replacing surface measurements, the aim of the remote sensing method at present time is to complement existing sampling programs over a broader spectrum of time and space scales. Surface hydrological records are especially necessary in calibration and validation of the remote sensing approaches. More and better surface observations are therefore continuously needed.

Table 2.1: Empirically Developed Models Relating to Suspended Sediment Concentration(Coastal)

Sensors	Location	Models	Range(g/l)	R	Samples	Reference
Landsat TM	Moreton Bay(Australia)	$TSS = 16.826 - 5.2369\frac{R_1}{R_2}$	0.69-9.2	0.83	53	Islam et al. (2003)
EO-1 AL1	Pearl River Estuary(China)	$TSS = -1229.5R_{549} + 53.795$	12-33.2	0.91	11	Fang et al. (2010)
SPOT	Gironde Estuary(France)	$SPM = 27.423e^{0.0279\frac{R_3}{R_1}}$	15-2500	0.89	132	Doxaran et al. (2003)
Landsat	Gironde Estuary(France)	$SPM = 29.022e^{0.0335\frac{R_4}{R_2}}$	15-2500	0.88	132	Doxaran et al. (2003)
SPOT	Loire Estuary(France)	$SPM = 18.895e^{0.0322\frac{R_3}{R_1}}$	10-2600	0.93	68	Doxaran et al. (2003)
Landsat	Loire Estuary(France)	$SPM = 26.083e^{0.0336\frac{R_4}{R_2}}$	10-2600	0.93	68	Doxaran et al. (2003)
MODIS	Hangzhou bay(China)	$lnSSC = 43.233R_2 + 1.369$	17-2500	0.87	25	Wang et al. (2009a)

Note: Equations are written as they are published, where SPM = Suspended Particulate Matter, SSC = Suspended Sediment Concentration, and TSS = Total Suspended Solids. Ri is the reflectance of the water at the given wavelengths(ith band).

Table 2.2: Empirically Developed Models Relating to Suspended Sediment Concentration(Lakes and Reserviors)

Sensors	Location	Models	Range(g/l)	R	Samples	Reference
Landsat MSS	Enid Reservoir(US)	$lnSSC = -9.2\frac{R_1}{R_2} + 2.71(\frac{R_1}{R_2})^2 + 8.45$	2-168	0.82	77	Ritchie and Cooper (1991)
Landsat ETM	Tailu Lake(China)	$TSM = 0.221R_4 + 60.293$	0.12-37.64	0.911	11	Ma and Dai (2005)
Landsat MSS	Lake Chicot(US)	$R_3 = 0.18(1 - e^{-\frac{SSC}{88.8}}$	25-	0.62	310	Schiebe et al. (1992)
Landsat TM	Frisian lakes(Netherlands)	$TSM = 0.7581e^{61.683(\frac{R_1+R_2}{2})}$	3-50	0.99	10	Dekker et al. (2001)
Landsat TM	Lake Michigan(US)	$TSS = 0.0167e^{12.3\frac{R_3}{R_1}}$	-35			Lathrop (1986); Lathrop Jr and Lillesand (1989)

Note: Equations are written as they are published, where SSC = Suspended Sediment Concentration, TSM = Total Suspended Matter, and TSS = Total Suspended Solids. Ri is the reflectance of the water at the given wavelengths(ith band).

Table 2.3: Empirically Developed Models Relating to Suspended Sediment Concentration(Rivers)

Sensors	Location	Models	Range(g/l)	R	Samples	Reference
MODIS	Yangtze River(China)	$SSC = -23.03 + 60.24(R_2 - R_5)$	74-81	0.73	153	Wang et al. (2010)
MODIS	Yangtze River(China)	$ln(SSC) = 4.117 + 0.262(R_2 - R_5)$	45-909	0.78	35	Wang and Lu (2010)
Landsat TM	Yangtze River(China)	$ln(SSC) = 3.18263ln(R_4) - 1.40060$	22-2610	0.88	24	Wang et al. (2009b)
MODIS	Ganges and Brahmaputra Rivers(Bangladesh)	$SSC = 69.39R_3 - 201$	0-1200	0.98	10	Islam et al. (2001)
MODIS	Kangerlussuaq Fjord(Greenland)	$R_1 = 7.5log(SSC) + 1.6$		0.90	22	Chu et al. (2009)

Note: Equations are written as they are published, where SSC = Suspended Sediment Concentration. Ri is the reflectance of the water at the given wavelengths(ith band).

Table 2.4: Empirically Developed Models Relating to Suspended Sediment Concentration(Laboratory)

Sensors	Location	Models	Range(g/l)	R	Samples	Reference
	Clay	$SSC = 16.956 + 14.711R_{855} + 192.0R_{855}^2$	50-1000	0.96	10	Lodhi et al. (1997b)
	Silty	$SSC = -23.367 + 116.869R_{852} + 24.04R_{852}^2$	50-1000	0.99	10	Lodhi et al. (1997b)
	Clay(organic)$< 63\ \mu m$	$SSC = 12.32(\frac{R_{555}}{R_{754}})^-0.31$	17.2-75.2	0.92	7	Gin et al. (2003)
	Clay(organic)$< 20\ \mu m$	$SSC = 16.72(\frac{R_{555}}{R_{754}})^-0.42$	23-166.5	0.99	8	Gin et al. (2003)
	Clay(organic)$< 10\ \mu m$	$SSC = 8.18(\frac{R_{555}}{R_{754}})^-0.26$	20.8-96.3	0.90	7	Gin et al. (2003)
	Clay(inorganic)$< 63\ \mu m$	$\frac{R_{595}}{R_{754}} = 0.04SSC + 2.06$	7-31.8	0.53	8	Gin et al. (2003)
	Clay(inorganic)$< 20\ \mu m$	$\frac{R_{595}}{R_{754}} = 0.01SSC + 3.25$	10.8-53	0.86	8	Gin et al. (2003)
	Clay(inorganic)$< 10\ \mu m$	$\frac{R_{595}}{R_{754}} = 0.03SSC + 3.6$	5.5-31.25	0.72	7	Gin et al. (2003)

Note: Equations are written as they are published, where SSC = Suspended Sediment Concentration. Ri is the reflectance of the water measured using spectroradiometer at the given wavelengths(nm).

Chapter 3

Simulation based on Controlled Laboratory Experiment

Abstract

We investigated the upper limit of suspended sediment concentration (SSC) with respect to the relationship between SSC and reflectance to develop an SSC remote sensing model for the highly-turbid Yellow River. An SSC quantification model was generated by using the spectral mixing index of sediments in water and sediment mixtures. In this study, laboratory experiments were made to measure the spectral curves of sediment-laden water with a high-resolution spectroradiometer. River-bed deposited sediments from two sites, one on the Yellow River at Huayuankou (HYK) and the other on the Wei River at Yangling (YL), and their sand, silt and clay particle groups were used for laboratory experiments to measure the spectral responses of sediment laden water. The correlation analysis depicted stable correlation between

SSC and reflectance at wavelengths ranging from 450 nm to 1000 nm, in which, spearman rank correlation coefficient (r_s) for all sediments were above 0.7 while the HYK natural sediment had Spearman coefficients exceeded 0.9. Experimental results revealed the curves of the relationship between SSC, up to 40 g/l. A physical-based exponential model ($R^2 > 0.9$) at each simulated Landsat band effectively interpreted the relationship between SSC and reflectance. The highest upper limit SSCs at 21 g/l and 15 g/l in natural YL and HYK sediments, respectively, were observed in Landsat Band 4. A spectral mixing algorithm was used to build the model and estimate the SSC from reflectance at correlated wavelength bands . The spectral mixing algorithm can generate a uniform model that disregards the effects of sediment type by adopting the reflectance curve at the upper-limit SSC to represent the standard reflectance of sediment. This study is useful in understanding the spectral characteristic of high SSC in water and in applying remote sensing techniques to monitor SSC in the Yellow River.

3.1 Introduction

Knowledge of the suspended sediment concentrations (SSC) in a river is essential for water quality assessment (Ritchie et al., 2003), hydraulic facility operations (Wang et al., 2005), and water resources management (Walling and Fang, 2003). The *in situ* sampling method that involves site selection, water sampling, sample transportation, laboratory processing, and post analysis is the most commonly used method for SSC observation (Edwards and Glysson, 1988). This sampling method is time-consuming, labor-intensive and provides only point data at gauging stations. Thus, studies have

focused on the development of new technologies for SSC measurements. A detailed review on the new techniques for suspended-sediment measurements by Wren et al. (2000) compared bottle sampling, pumping sampling, acoustic method, focused beam reflectance, laser diffraction, nuclear, optical backscatter, optical transmission, and spectral reflectance approaches. Although these methods provide accurate point-based measurements, they cannot capture the spatial variations (**??**).

The remote sensing method based on the relationship between the amount of radiation reflected by a body of water and the properties of that water may provide a spatial and synoptic view of sediment concentration. Various visible and near-infrared radiation-band (NIR-band) combinations acted as SSC indicators in coastal, estuarine, lagoon, lake and reservoir environments (Bhargava and Mariam, 1991; Choubey, 1994; Novo et al., 1989a, 1991; Schiebe et al., 1992).

The empirical models for SSC estimation generally took the following forms (Curran and Novo, 1988; Long and Pavelsky, 2013; Ritchie et al., 2003):

$$SSC = A + BRr \tag{3.1}$$

$$SSC = A + B \ln Rr \tag{3.2}$$

$$\ln SSC = A + BRr \tag{3.3}$$

$$\ln SSC = A + B \ln Rr \tag{3.4}$$

where Rr was the spectral measurement obtained from remote sensing or a spectroradiometer (i.e., radiance and reflectance), and SSC was the water quality parameter of interest. Specifically, the spectral measurement (Rr) could be reflectance in a single band, the ratio of reflectance in two bands (Bowker and Witte, 1975; Tassan and

Sturm, 1986; Topliss et al., 1990; Yuming and Min, 1992; Doxaran et al., 2009), or the linear combination of these parameters (Khorram, 1985; Raaj et al., 2008; Wang et al., 2012). The linear and nonlinear relationship between SSC and reflectance was explained by the radiative transfer theory in chapter 2.

The sediment load in the Yellow River is considered the second highest in the world for the last several thousand years. Annual sediment load in the Yellow River was $1.08 \times 10^{12}\ kg/yr$ (Milliman and Meade, 1983), which represents 6% of the estimated global river sediment flux to oceans. The water of the Yellow River is dominated by a high load of suspended sediments, e.g. the average SSC at the Huangpu gauging station from 2002 to 2007 was 313 g/l (Peng et al., 2010).

To implement the remote sensing technology within a highly turbid river, the valid range of the relationship between SSC and spectral reflectance have to be evaluated. The correlation between SSC and reflectance in highly-turbid water is stronger thanthat in low turbidity pure waters (Kirk, 1984; Mobley and Mobley, 1994) because the suspended sediments actively scatter the light. However, the application of remote sensing methods in highly turbid rivers was limited compared with those in coastal, estuarine, lagoon, lake, and reservoir environments. The results obtained from those relatively mild and placid waters may be inappropriate for highly-turbid inland river flows. The few studies on rivers involved short river reaches with mild and moderately turbid waters, such as the Ganges-Brahmaputra Rivers (Islam et al., 2001), the Danube River (Onderka and Pekrov 2008), and Yangtze River (Wang et al., 2009b; Wang and Lu, 2010). According to a recent review of empirically developed models that relate SSC or turbidity to reflectance from the water surface, most models focused on low SSCs with a cutoff of approximately 2.5 g/l (Long and Pavelsky, 2013).

The effect of sediment variations along the river on the remote sensing model must also be determined. Several factors such as soil type, viewing geometry, the bottom reflectance, and air-water interface may affect the relationship between SSC and reflectance. The effects of these factors were not properly addressed in the widely-used empirical models (Bhargava and Mariam, 1991; Chen et al., 1992; Gray et al., 2000; Han and Rundquist, 1994; Novo et al., 1989b; Schmugge et al., 2002). The variety of sediments produced according to sediment-sourced soil type is a foremost concern in the application of the remote sensing method to large river systems because the influence of the sediment type cannot be ignored when the sediments are sourced from large areas measuring hundreds to thousands of square kilometers. Han and Rundquist (1996) compared the standard reflectance spectra generated from two types of clay soil with different textures and found that the reflectance from finer soil increased with SSC more dramatically than the reflectance from coarse soil. Novo et al. (1989b) found that the strength of the reflectance-SSC relationship was affected by sediment type and the fine (white) sediments differ from coarse (red) sediments. Reflectivity increased with decreasing particle size and the shape of the relationship curve depends on soil type (Bhargava and Mariam, 1991). Turbidity in bentonite clay and black cotton soil was linearly related to reflectance, whereas the turbidity of kaoline and gray soil is curvilinearly related to reflectance (Bhargava and Mariam, 1990). Sediment variability is increasingly significant in river waters because of the increase in sediment variety originates from runoff with eroded soil in runoff from a vast agricultural areas. Most current studies focused only on regression-based relationships between SSC and reflectance do not consider the effects of sediment type variability, particularly in large river systems.

In terrestrial studies, the spectral mixing algorithms have been widely used, which

consider a given pixel as a liner combination of primary components (e.g. vegetation, soil, and water). The spectral mixture model is advantageous for maximizing the use of the spectral information in satellite imagery (Oyama et al., 2007; Matsushita and Fukushima, 2009; Tyler et al., 2006). Zawada et al. (2007) reported that satellite-based observations can estimate total suspended solid concentrations in estuarine areas, such as Chesapeake Bay, by using a spectra-matching optimization algorithm based on Sea-Viewing Wide-Field-of-View Sensor satellite imagery. Oyama et al. (2007) developed a spectral composition algorithm (SDA) based on a linear, spectral mixture-modeling approach to estimate chlorophyll α concentration and non-phytoplankton suspended sediments (NPSS) from multispectral satellite data. Oyama et al. (2009, 2010) applied and tested the aforementioned SDA to estimate the chlorophyll α and NPSS and indicated that SDA-based models were superior to conventional empirical models.

Our research ultimately aimed to model SSC in a large river system. Our objectives were: (1) to investigate a SSC upper limit, which can be estimated from the correlation between SSC and reflectance; and (2) to develop a spectral mixing algorithm for remote sensing SSC in the Yellow River, which considers the impact of sediment variability in terms of particle distribution.

3.2 Materials and Methods

3.2.1 Sediment Preparation and Experiment Setup

The experiment was conducted at the State Key Laboratory of Soil Erosion and Dryland Farming in Loess Plateau, Institute of Soil and Water Conservation, Chinese

Academy of Sciences. The dry sediments that were used to make the sediment-laden water sample in the laboratory was collected from two locations in central reach of the Yellow River: Yangling (YL; $108°2'29.50''E$, $34°14'1.53''N$), and Huayuankou (HYK; $113°40'5.74''E$, $34°54'22.68''N$). YL is situated on the Wei River that is the largest Yellow River tributary. HYK is a primary hydrological station located in Zhenzhou, Henan province, on the mainstream of the Yellow River.

The sediment preparation involved four steps: (1) drying in air and pulverization; (2) filtration by passing through 2 mm mesh sieves to remove gravels; (3) mixing with water to filter the tiny residues floating up on the surface of the water, and (4) drying in an oven at $105°C$ for 12 hours.

Portions of pre-possessed YL and HYK sediments were further divided into clay, silt and sand by using the wet sieving method to enable the investigation of the effect of particle size on the spectral profiles of sediment-laden water. Eight sediment types were generated (i.e., natural, clay, silt, and sand sediment types for YL and HYK), where "natural" represents the original sediment with natural particle distribution. The particle size distributions for YL and HYK sediments were shown in Table 3.1.

Table 3.1: The particle size distributions for Huayuankou (YHK) and Yangling (YL) sediments

Sediments	Particle Size			D_{50}
	$< 0.002mm$	$0.002 - 0.05mm$	$> 0.05mm$	
	%	%	%	mm
HYK-Natural	27.97	59.52	12.51	14.03
YL-Natural	18.48	67.32	14.20	21.59

[1] The median grain size, D_{50}, is the size for which 50% of the particle mass consists of finer particles.

The experiment was conducted in a dark room to avoid the influence from the atmosphere and illumination variability. A container that was 13.2 cm in diameter and 16.0 cm deep, and with a volume of 2.3 l, was used for all experiments. The interior of the container was wrapped with black waterproof tape to minimize extraneous light reflectance (Han and Rundquist, 1994; Gin et al., 2003; Oyama et al., 2007). The container was filled with water and sediment mixture at a depth of 15.0 cm and a volume of approximately 2.0 l.

Spectral data were collected by using a FieldSpec® HandHeld 2™ Spectroradiometer (ASD Inc. Boulder, Colorado, USA). This instrument acquired data from 325 nm to 1075 nm at 1 nm intervals. A 25° field-of-view optic fitted to the spectroradiometer provided an 8.8 cm-diameter instantaneous field of view of the water surface, which was within the diameter of the container. The spectroradiometer sensor was positioned over the center of the container 20 cm above the water surface, and observations were made via a nadir view angle (Figure 3.1). Two 500 W halogen lamps were positioned face-to-face at sensor height and inclined at 45° to avoid shadowing the target area.

A 5"×5" spectral reflectance panel (SRM-990 Spectralon®, LabSphere, Inc. North Sutton, NH) diffusely reflected nearly 100% of the incident light throughout the spectral range. This panel served as the calibration standard to convert the radiance to reflectance. Radiance was measured three times for each sample and once (before sample measurements) for the reference panel. The mean of measurements were used in the analyses. Wavelength-specific reflectance $Rr(\lambda)(\%)$ was calculated by using the following equation:

$$Rr(\lambda) = \frac{L(\lambda)}{L_0(\lambda)} Cal(\lambda) \tag{3.5}$$

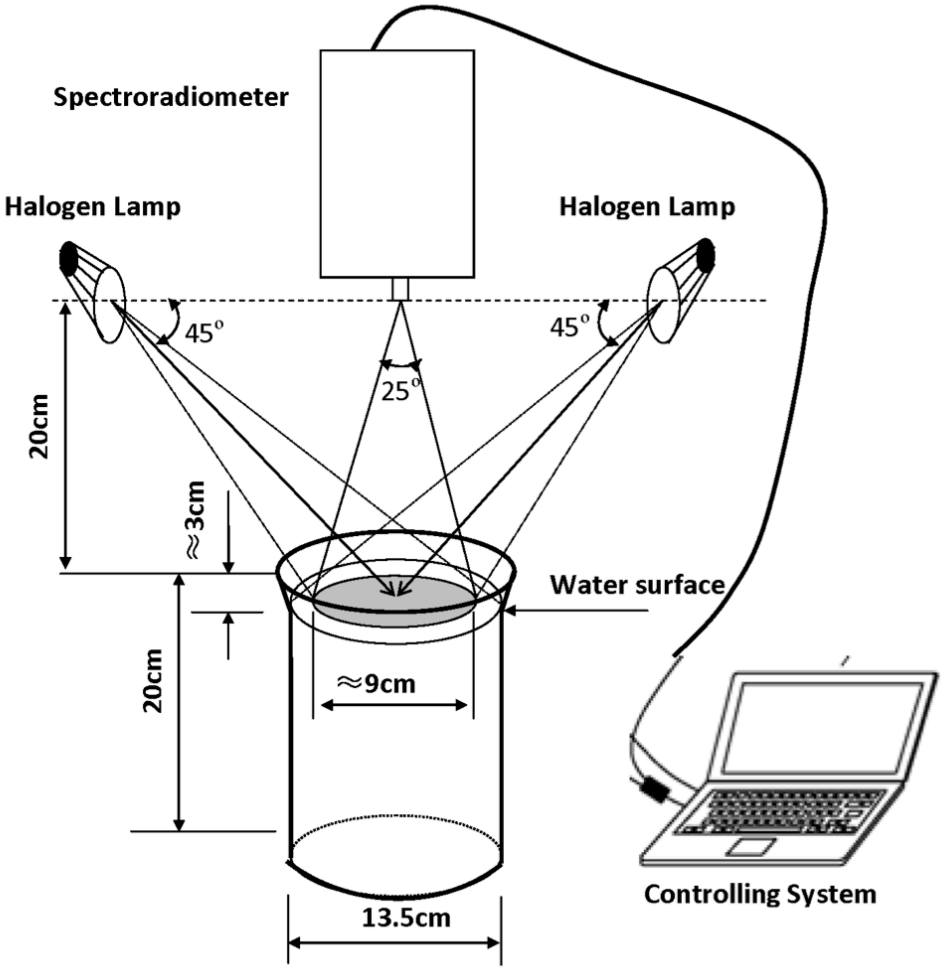

Figure 3.1: Schemetic design for the controlled experiment in the laboratory

where $L(\lambda)$ was the wavelength-specific radiance from the water surface, for each sample, which was measured by the spectroradiometer; $L_0(\lambda)$ denoted the white reference by placing the reference panel above the water surface. The white reference was updated before measuring each water sample. $Cal(\lambda)$ was the reflectance panel calibration factor that was provided by the manufacture.

A total of 34 SSC samples (0 to 40 g/l) for each sediment type was produced by adding certain amounts of sediment consecutively into 2 l water. The water initially without sediments, and then the SSC increased to the designed concentration stepwise. The SSC increments in the sample generation process were as follows: 0.1 g/l from 0 to 1.0 g/l, 0.2 g/l from 1.0 to 2.0 g/l, 1.0 g/l from 2.0 to 10.0 g/l, 2.0 g/l from 10.0 to 20.0 g/l, and 4.0 g/l from 20.0 to 40.0 g/l. Reflectance was measured 3 times at each SSC level to obtain the averaged value to get the reflectance profile with increasing SSC. A total of 34×8 samples (corresponding 34 SSC levels and 8 sediment types) was measured by using the spectroradiometer.

The reflectance of dry sediments for each sediment type was also measured by using the spectroradiometer by placing 2 cm-deep dried sediments at water sample height. The reflectance of the dry sediments was then calculated by using Eq.(3.5). Figure 3.2 showed dry sediment reflectance curves of all sediment types and clean water ($SSC = 0$).

3.2.2 Correlation Analysis

The spearman correlation coefficient (r_s), defined as the Pearson correlation coefficient (r) between the ranked variables, is a nonparametric measure of statistical dependence between two variables. The r_s between SSC and reflectance, at each λ wavelength

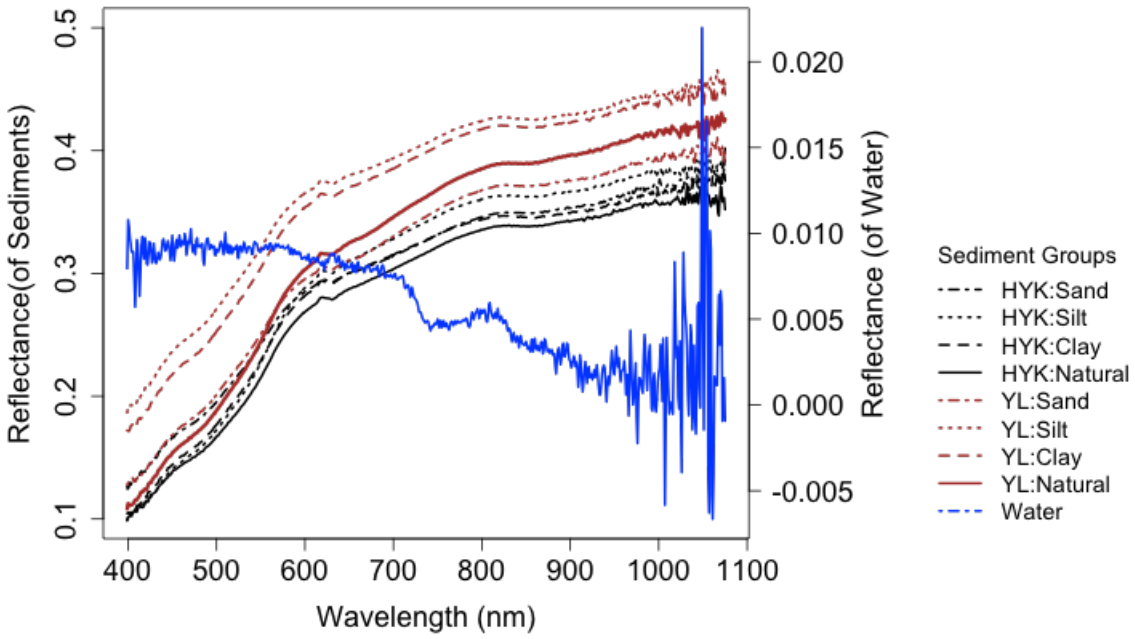

Figure 3.2: Spectral profiles of clean water and dry sediment

ranging from 325 nm to 1075 nm at 1 nm intervals, was calculated as follows:

$$r_s = \frac{\sum_{i=1}^{n}(x_i - \overline{x})(y_i - \overline{y})}{\sqrt{\sum_{i=1}^{n}(x_i - \overline{x})^2}\sqrt{\sum_{i=1}^{n}(y_i - \overline{y})^2}} \tag{3.6}$$

where x and y are the ranked SSC and reflectance at a certain wavelength, respectively, and n is the number of SSC levels, 34 in this case. SSC and reflectance values was tested for normality by using the Shapiro-Wilk statistics. R software was used for statistical analysis (R Core Team, 2013).

The results of our experiment were able to reveal the complete patten of the relationship between SSC and reflectance with SSC from 0 to 40 g/l. A physical-based exponential model (Schiebe et al., 1992) expressed this relationship.

$$Rr(\lambda) = C_1(\lambda)(1 - e^{-\frac{SSC}{C_0(\lambda)}}) \tag{3.7}$$

where $Rr(\lambda)$ was the wavelength-specific reflectance, $C_1(\%)$ and $C_0(g/l)$ were the coefficients obtained by nonlinear regression. The exponential equation indicated that reflectance increases with increasing SSC and that the reflectance slope decreased with increasing water turbidity. Reflectance approached to an asymptotic value ($C_1(\lambda)$) with the continuos increases of SSC. $C_1(\lambda)$ may denote the reflectance saturation level, beyond which reflectance did not change with increasing SSC. $C_0(\lambda)$ was the concentration parameter that represents the velocity to approach the saturation level. The concentration parameter was mathematically equal to SSC when reflectance was 63% of the saturation level. The 90% saturation level $C_{90}(\lambda)$ was introduced to represent the SSC upper limit because $C_1(\lambda)$ was a asymptote that could be continually approaching but does not meet at any finite distance. The SSC upper limit can be estimated based on reflectance, and was the valid correlation range between SSC and reflectance. The predictable SSC was the maximum SSC upper limit value at wavelengths ranging from 400 nm to 1000 nm.

$$C_{90}(\lambda) = -\ln(0.1)C_0(\lambda) = 2.3C_0(\lambda) \tag{3.8}$$

$$C_{90} = Max[C_{90}(\lambda)] \tag{3.9}$$

The spectroradiometer measured data between 400 nm and 900 nm were converted to Landsat ETM+ bands by averaging each bandwidth (Band 1: 450 nm to 520 nm, Band 2: 520 nm to 600 nm, Band 3: 630 nm to 690 nm, and Band 4: 760 nm to 900 nm).

3.2.3 Spectral Mixing Algorithm

The spectral mixing algorithm proposed in our study was composed of two key steps. First, the water reflectance at each SSC was translated to the spectral mixing index of primary water constituents on the basis of the assumption that the mixed-reflectance spectrum of a given pixel is a linear combination of these constituents, including water. The spectral radiance/reflectance of a volume of turbid water can be conceptualized into a composite signal by using the weighted sum of the primary water components , such as clean water, non-phytoplankton suspended sediments, and phytoplankton (Goodin et al., 1993). Distilled water and dry sediment were the only components of water sample in our experiment.

$$Rr(\lambda) = SMI_w P_w(\lambda) + SMI_s P_s(\lambda) \tag{3.10}$$

where SMI_w and SMI_s are spectral mixing indexes of water and sediment, respectively. These indexes were directly related to their masses/concentrations. $P_w(\lambda)$ and $P_s(\lambda)$ represented the distinctive spectral patternsof clean water and sediment.

The spectral mixing index for sediment (SMI_s) and water (SMI_w) in simulated Landsat (TM ETM+) data at each concentration (34 SSCs from 0 to 40 g/l) could be estimated by solving the following equations by the least squares method.

$$Rr(B_1) = SMI_w P_w(B_1) + SMI_s P_s(B_1) \tag{3.11}$$

$$Rr(B_2) = SMI_w P_w(B_2) + SMI_s P_s(B_2) \tag{3.12}$$

$$Rr(B_3) = SMI_w P_w(B_3) + SMI_s P_s(B_3) \tag{3.13}$$

$$Rr(B_4) = SMI_w P_w(B_4) + SMI_s P_s(B_4) \tag{3.14}$$

where $Rr(Bi)$, $P_w(B_i)$, $P_s(B_i)(i = 1, 2, 3, 4)$ were the reflectance, standard water reflectance spectra, and standard sediment reflectance spectra at the ith simulated Landsat ETM+ band, respectively.

Selecting the standard reflectance spectra of the water and sediment (P_s and P_w) was very important. The standard clean water reflectance (P_w) was measured by the spectroradiometer in our laboratory experiment. Two methods were tested to obtain the standard sediment reflectance spectrum (P_s) in this study. First, the dry sediment reflectance measurement was used to represent the standard sediment reflectance spectrum (Oyama et al., 2007, 2009, 2010). Second, the reflectance saturation level [C_1 in Eq.(3.7)] was introduced into each simulated Landsat ETM+ band as the standard sediment reflectance spectra on the basis of our experiment findings regarding the SSC upper limit in the SSC-reflectance relationship. We then obtained the following expression:

$$P_s(\lambda) = C_1(\lambda) \tag{3.15}$$

The SMI_s obtained in the first step was applied to construct the SSC estimation model in the second spectral mixing algorithm step:

$$SSC = a\ e^{b\ SMI_s} \tag{3.16}$$

$$\ln(SSC) = A + B\ SMI_s \tag{3.17}$$

where a, b and A, B were regression coefficients, and $A = \ln a$, $B = b$.

We also tried an exponential model that was obtained by replacing the $Rr(\lambda)$ in

Eq.(3.7) to SMI_s :

$$SMI_s = C_1(1 - e^{-\frac{SSC}{C_0}}) \tag{3.18}$$

where C_1 and C_0 are regression coefficients, SMI_s replace the $Rr(\lambda)$ in Eq.(3.7) to integrate the information at all available bands. Or, Eq.(3.18) could be transformed to an explicit form for SSC estimation:

$$SSC = C_0 lnC_1 - C_0 ln(C_1 - SMI_s) \tag{3.19}$$

3.3 Results

3.3.1 Reflectance Spectrum Profiles

The spectral profiles of reflectance curves along the entire measured bandwidth (325 nm to 1025 nm) were generated to determine the spectral characteristics of the sediment-laden water (Figure 3.3 for YL sediments). The overall reflectance in all eight sediment types (YL and HYK: natural, clay, silt, sand), increased as SSC increased from 0 to 40 g/l. The reflectance showed an obvious increasing trend from coarse to fine particles (sand, silt to clay). The magnitude of the spectrum profile showed an evidently increasing trend from coarse to fine particle (sand and silt to clay). The natural types in both YL and HYK sediments displayed the highest magnitude; thus the particle mixture among different types enhanced reflectance. Reflectance increased with decreasing particle size from sand to silt and then to clay in sediment types with uniform particles ; therefore, fine particles displayed higher reflectance.

The reflectance of highly-turbid water (SSC above 10 g/l and 14 g/l for HYK

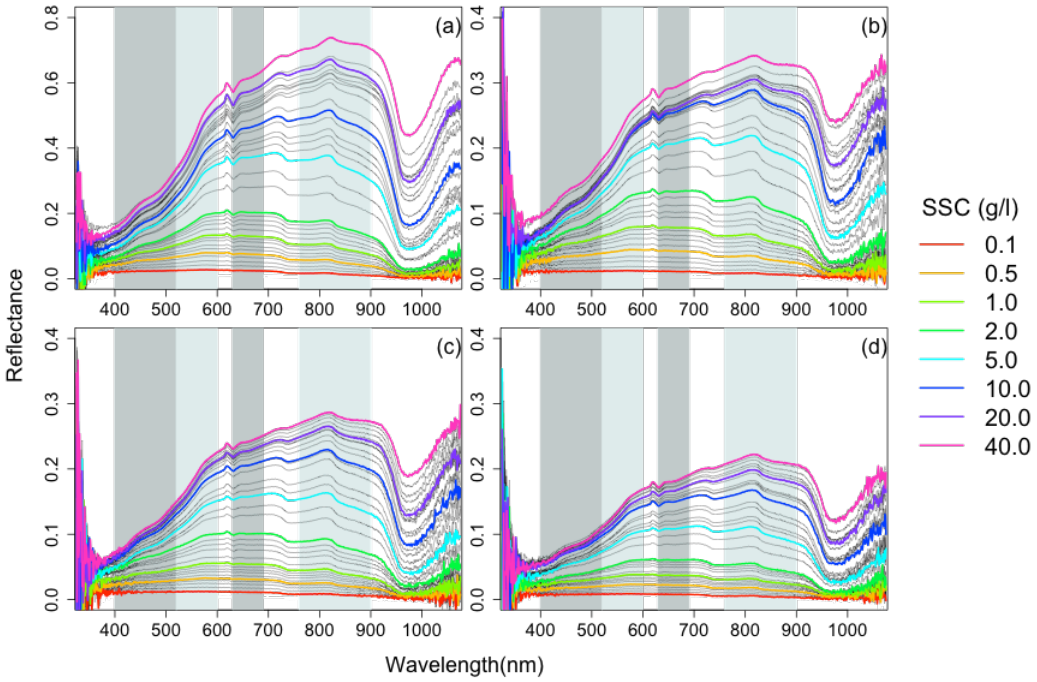

Figure 3.3: Reflectance profiles of sediment-laden water made from the YangLing(YL) sediment. The colored curves represent the SSC changing from 0 to 40 g/l for sediment types of (a) natural, (b) sand, (c) silt, and (d) clay, respectively. The y axis (Reflectance) in (b), (c) and (d) were scaled to present the detail of the corresponding dataset.

and YL sediments, respectively) was greater than reflectance of the dry sediment at wavelengths ranging from 400 to 920 nm. HYK sediments dispersed more than YL sediments.Troughs in the reflectance over the measured bandwidth (325 nm to 1075 nm) were observed at approximately 620 nm to 675 nm and 950 nm to 1000 nm, whereas a peak appeared at approximately 600 nm to 700 nm and 800 nm to 950 nm for low and high SSCs, respectively. The trough at 950 nm to 1000 nm became more obvious with increasing water turbidity.

A detailed comparison of reflectance curves among different sediment types showed that the reflectance curves pattern gradually transformed with increasing SSC (Figure 3.4)(The scale in each subplot was different to show the detail of the curves clearly). The reflectance curves were relatively even over the wavelength when SSC is 0.1 g/l. A peak was observed at a wavelength of approximately 600 nm with increasing SSC. A secondary peak was revealed at a wavelength of approximately 800 nm and became dominant when SSC exceeded 5.0 g/l. Our results showed that the reflectance of mildly turbid sediment-laden water (SSC $<$ 1.0 g/l) was high at short-wavelength bands, such as green and red bands [Band 2 and 3 of Landsat ETM+]. NIR-bands [Band 4 of Landsat ETM)] may be used to estimate SSC in highly-turbid water (SSC$>$ 5.0 g/l).

3.3.2 Relationship between Reflectance and SSC

The Spearman rank correlation coefficient (r_s) was calculated for all sediment types over the measured bandwidth (350 nm to 1075 nm) to investigate the relationship between reflectance and SSC (Figure 3.5). The r_s value exceeded 0.7 at wavelengths ranging from 450 nm to 1000 nm and were stable; r_s values notably varied at wave-

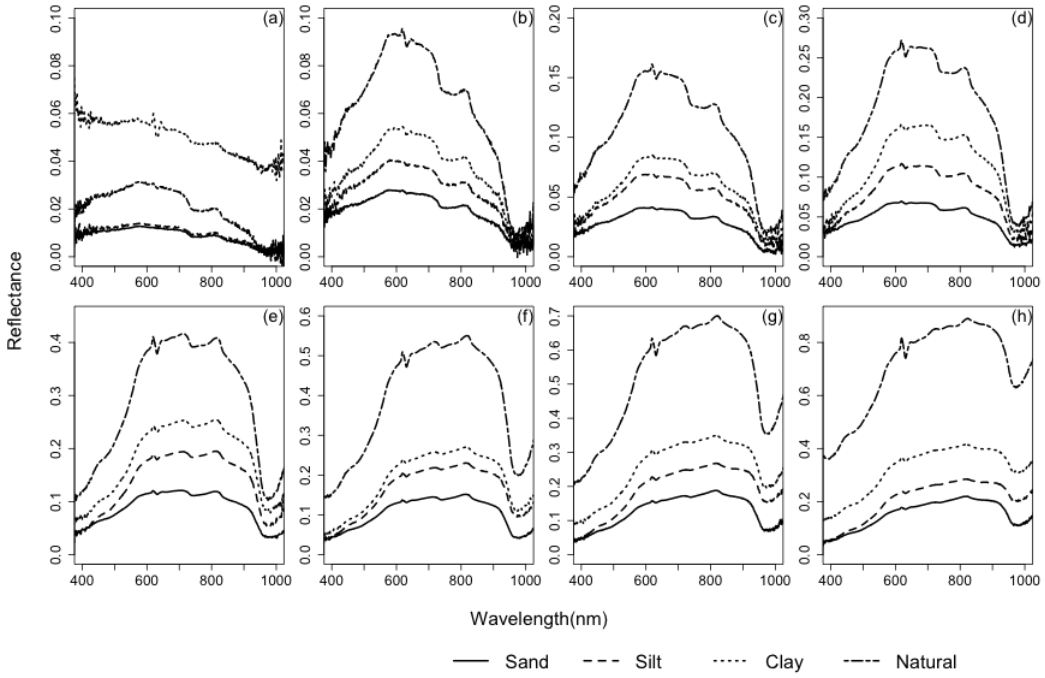

Figure 3.4: Comparison of the spectral curve of reflectance curve among different sediment types for Huayuankou (HYK) sediment, (a) to (h) were SSC at 0.1, 0.5, 1.0, 2.0, 5.0, 10.0, 20.0, and 40.0 g/l, respectively.

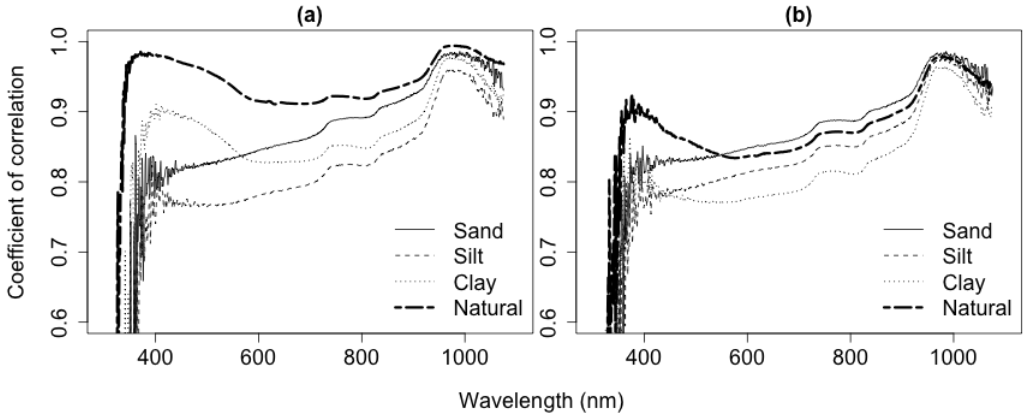

Figure 3.5: The Spearman rank correlation coefficient between SSC and reflectance from 325 nm to 1075 nm for sediment from HYK (a) and YL (b)

lengths beyond this range.

The Shapiro-Wilk test indicated that reflectance and SSC values did not follow normal distributions Therefore, the exponential equation Eq.(3.7) was used to describe the relationship between SSC and reflectance. SSC was log (natural) transformed to develop the relation with SMIs Eq. (3.17).

The r_s values of natural HYK and YL sediment exceeded 0.9 at wavelengths above 400 nm and 900 nm, respectively. The averaged value over 400 nm to 900 nm were 0.93 and 0.85 for HYK natural sediment and YL natural sediment, respectively. This result indicated that the reflectance-SSC relationship in HYK natural sediment was stronger than that in YL natural sediment. However, the r_s value for the uniform particle groups were not change much between HYK sediment (sand 0.85, silt 0.79, and clay 0.86) and YL sediment (sand 0.85, silt 0.82, and clay 0.79) The correlation curves of sand and silt types showed a similar pattern, whereas clay had relatively high r_s values at short wavelengths (350 nm to 600 nm). The natural type followed the clay pattern. Our results indicated that clay in sediment composition played an

important role in determining correlation curve patterns, while sand and silt affected the magnitude of the correlation curves.

Reflectance as measured by the spectroradiometer was simulated in Landsat ETM+ bands [Band 1 (blue): 450-520 nm, Band 2 (green): 520-600 nm, Band 3 (red): 630-690 nm, Band 4 (NIR): 760-900 nm] by averaging the the measured reflectance along the certain band.

The reflectance at all bands exponentially changed with SSC (Figure 3.6.) according to the relationship in Eq.(3.7). The standard deviations of HYK natural and YL clay sediments were quite large, particularly when the SSC and its increment changed from from 20 g/l to 24 g/l and 2 to 4 g/l, respectively, during sample generation. Abnormally large standard deviations seems to be arose from the sample generation process because the sediment and water mixture was stirred manually.

The reflectance for each band and the corresponding SSCs was fitted by using Eq.(3.7) given the regression coefficients shown in Table 3.2. Our results indicated that reflectance at all bands was correlated with SSC [$R^2 > 0.9$ in Table (3.2)]. Reflectance tended to become asymptotic when the SSC exceeded a certain level (approximately 20 g/l). Reflectance did not change greatly as SSC increases, thus revealing the upper limit that determines SSC based on reflectance. The upper limit of the reflectance-SSC correlation may be represented by the 90% saturation level of the exponential curve. Landsat ETM+ Band 4 estimated high SSC most effectively because this band had the highest C_{90} value (Table 3.2). The SSC upper limit varied in different soil types; the natural generated the highest value ($2.3 \times C_0 = 21.52$ g/l and $2.3 \times C_0 = 15.77$ g/l for HYK and YL, respectively), followed by the sand, silt and clay types for HYK sediments and sand, clay, and silt types for YL sediments. Coarser sediments corresponded to better the particle mixtures among different sizes

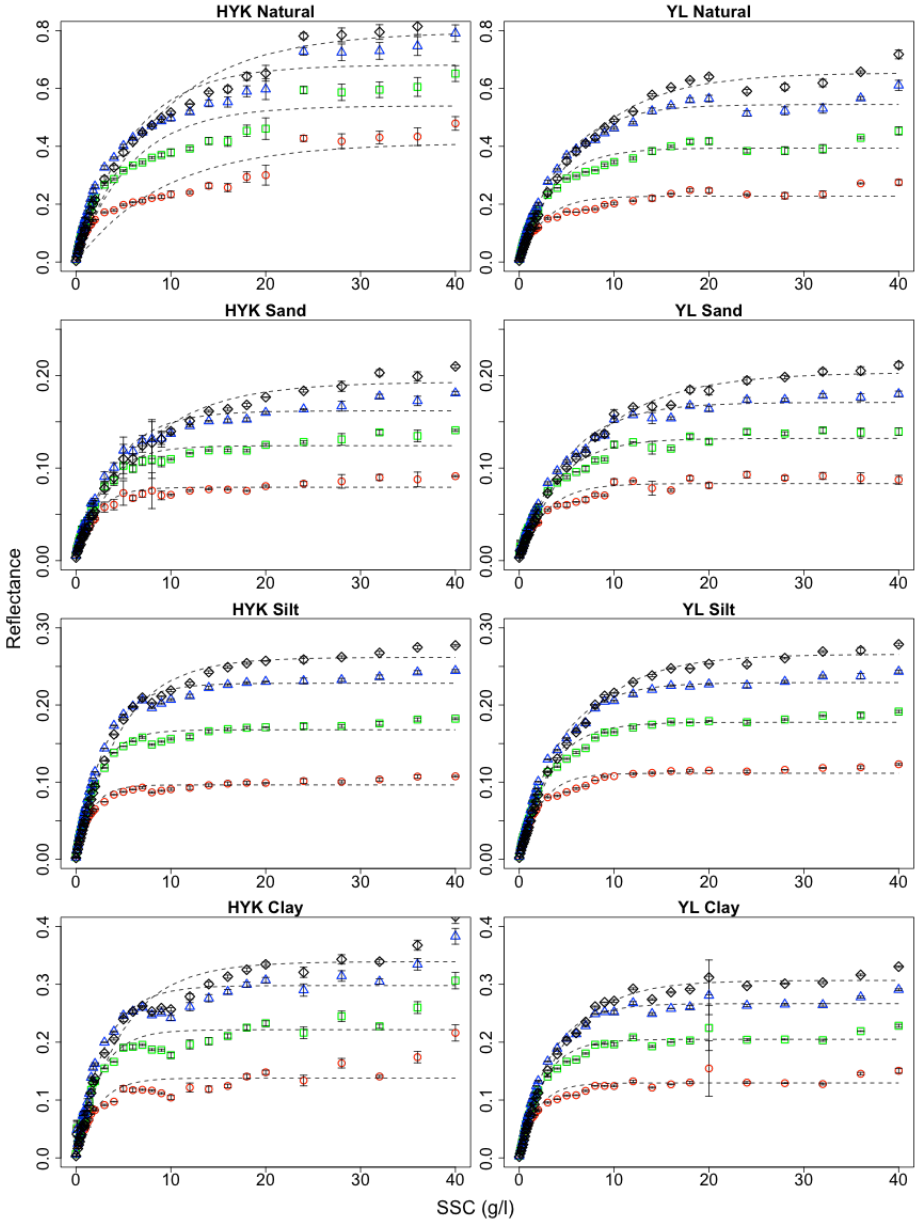

Figure 3.6: The relationship between SSC and reflectance for simulated Landsat bands. The symbol circle, square, triangle, and diamonds indicate averaged reflectance on Bands 1 (450-515 nm), Bands 2 (525-605 nm), Band 3 (630-690 nm) and Band 4 (750-900 nm), respectively. The dashed lines were fitting curves according to the exponential model. The Standard Deviation (SD) of three measurements were calculated and showed as the vertical bars on the data points). Plots for each sediment type were scaled independently for best presenting.

and allowed reflectance to estimate higher SSC.

Table 3.2: Coefficients for Simulated Landsat(TM ETM+) Bands

Sediment Type		**Huyuankou(HYK)**				**Yangling(YL)**			
		Band1	Band2	Band3	Band4	Band1	Band2	Band3	Band4
Natural	C_0	9.358	5.723	5.799	8.591	2.533	3.482	4.428	6.859
	C_1	0.409	0.552	0.681	0.794	0.224	0.407	0.545	0.652
	R^2	0.953	0.974	0.985	0.993	0.984	0.993	0.996	0.998
	$F_{(\mathrm{ANOVA})}$	20.36	23.42	66.03	142.80	59.62	146.77	273.79	443.44
		* * *	* * *	* * *	* * *	* * *	* * *	* * *	* * *
Sand	C_0	2.051	2.954	3.959	6.845	2.719	3.842	4.818	7.384
	C_1	0.078	0.127	0.162	0.192	0.082	0.136	0.171	0.203
	R^2	0.991	0.993	0.995	0.996	0.989	0.995	0.997	0.998
	$F_{(\mathrm{ANOVA})}$	107.90	148.57	183.54	253.45	86.59	189.37	330.06	652.36
		* * *	* * *	* * *	* * *	* * *	* * *	* * *	* * *
Silt	C_0	1.549	2.270	2.960	4.587	2.150	3.146	3.923	1.500
	C_1	0.095	0.173	0.228	0.261	0.110	0.182	0.229	0.265
	R^2	0.995	0.997	0.998	0.998	0.994	0.997	0.998	0.999
	$F_{(\mathrm{ANOVA})}$	198.24	392.59	554.03	647.65	176.20	336.15	603.11	1332.36
		* * *	* * *	* * *	* * *	* * *	* * *	* * *	* * *
Clay	C_0	2.187	2.423	2.933	4.687	1.835	2.476	3.055	4.536
	C_1	0.136	0.228	0.298	0.339	0.128	0.210	0.267	0.306
	R^2	0.960	0.982	0.989	0.991	0.992	0.997	0.998	0.999
	$F_{(\mathrm{ANOVA})}$	23.83	55.18	85.98	105.08	124.76	323.79	599.36	796.50
		* * *	* * *	* * *	* * *	* * *	* * *	* * *	* * *

[1] For regression ANOVA, the statistic F has an F distribution with degrees of freedom equals to m and $N-2$, m is number of explanatory variables (SSC and Rr in our study) and N is the total degree of freedom that equals to the sample size 34 in our study. $\int_0^{F_a} F(m,n)\mathrm{d}v = 1-\alpha$, $m=2$ and $n=32$ are degree of freedom for model and variable, respectively. The criteria value F_α at significant level (α) are 0.05, 0.01, and 0.001 are 3.32, 5.49, and 8.77, respectively.

3.3.3 Spectral Mixing Algorithm

Spectral mixing algorithm was introduced to maximize the correlation between reflectance and SSC in all bands. One equation from each band [Eq. (3.11) to Eq. (3.14)] was generated to solve the spectral mixing indexes SMI_s and SMI_w by using

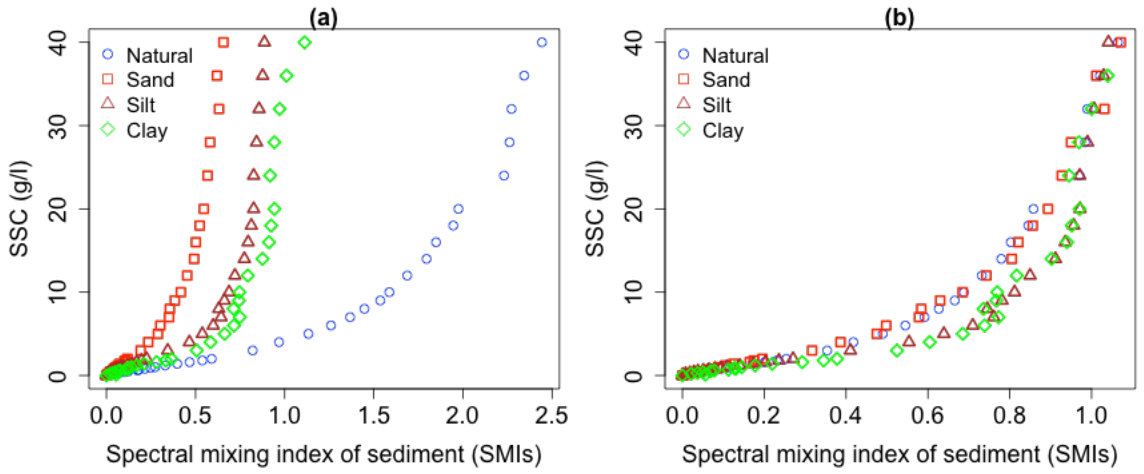

Figure 3.7: Relationship between SSC and spectral mixing index of sediment (SMI_s) for HYK sediments, (a) using dry sediment reflectance as the standard reflectance, (b) using saturated reflectance as the standard reflectance.

the least squares method. The standard sediment reflectance spectrum at each band [$P_s w(B_1)$, $P_s w(B_2)$, $P_s(B_3)$, and $P_s(B_4)$] was applied in two instances: in the spectral measurement of the dry sediment and in the saturated reflectance (C_1) estimation by Eq. (3.7).

Figure 3.7 (a) showed the relationships between SMI_s and SSC in different sediment types in the first application. The plots of SMI_s and SSC in different sediment types were separated from each other. The natural type had the least slopes followed by the clay, silt, and sand types. Our results indicated that the particle size variety of sediment type in terms of particle size is a considerable factor that affected the SSC estimation model considerably when the spectral measurements of dry sediment were incorporated into the spectral mixing algorithm.

Figure 3.7 (b) depicted the relationships between SMI_s and the SSC in all sediment types when standard reflectance spectra were estimated by saturated reflectance in spectral mixing algorithm. With the Y axis (SMI_s) having the same scale, the

comparison of the data range on X axis [around 2.0 in Figure 3.7 (a) and 1.0 in Figure 3.7 (b)]indicated that the relationship curve had lower slope in Figure and narrow plot divergences among the sediment types was exhibited when the standard reflectance spectra were estimated by saturated reflectance in the spectral mixing algorithm reflectance.

The SSC estimation model Eq.(3.16) was parameterized by using $SMIs$ and the corresponding SSCs (0 to 21 g/l and 0 to 15 g/l for HYK and YL sediments, respectively,) according to the estimated upper limit (C_{90} in Table 3.2) to predict SSC. These SSC ranges were applicable to this model and represented the limit for all other possible models based on the correlations between SSC and reflectance. The fitted SSC model summary (Table 3.3) confirmed the strong correlation between SSC and SMI_s in all sediment types ($R^2 > 0.96$).

We also tried the exponential model for SMI_s as Eq.(3.18), the result showed that the exponential model were as good as the logarithm transformed model Eq.(3.16), the R^2 values for the regression was above 0.99 for the both HYK and YL natural sediments. To compare the possible application of the model for different sediment types, the data from two sediment groups were combined for regression. The comparison between observed/designed SSCs and estimated SSCs from the sediment-combined regression models showed that the logarithm transformed model ($R^2 = 0.906$, $F = 523$, $p < 2e - 16$) is more suitable for application across sediment groups than the exponential model ($R^2 = 0.862$, $F = 338$, $p < 2e - 16$)

To further investigate the accuracy of the logarithm transformed model obtained from one site to other sites, the SSC of YL sediment was predicted by measuring its reflectance by Eq. (3.16) and parameters derived from the HYK sediment. The predicted and actual SSCs (designed SSCs) were compared in Figure 3.8. For SSC

less than 10 g/l, the prediction of SSCs agreed well with the true values well. For higher SSC, the prediction tends to underestimate the SSC slightly.

3.4 Discussion

3.4.1 Correlation and Particle Size

A valid correlation range between SSC and spectral reflectance must be established before remote sensing technology can be applied to a high turbid river. Maximum SSC was approximately 2.5 g/l according to the remote sensing SSC estimation models for estimating SSC (or turbidity that could be approximately converted to SSC.) empirically developed previously(Long and Pavelsky, 2013). This SSC cutoff was derived from the SSC status in individual studies rather than from a theoretical foundation. Most previous studies were conducted on costal waters, lakes, and lagoons where SSC is usually low compared with inland rivers. Some researchers might question about the necessity investigating high SSC (40 g/l), and current studies infer high SSC levels to be several g/l (Long and Pavelsky, 2013). The annual average SSC in the middle portion of the Yellow River is 23.69 g/l (Peng et al., 2010). Therefore the correlation between SSC and reflectance must be established before building a reliable model for the remote sensing of SSC in highly turbid waters. For sediment from the Yellow River in our experiment, the relationship between SSC and reflectance for simulated Landsat(TM ETM+) bands was observed even if SSC for sediment from the Yellow River was as high as 20 g/l. The range obtained in the laboratory experiment should be validated by *in situ* or satellite data even though our findings encouraged the application of remote sensing SSC in river with SSC within 20 g/l. Our results

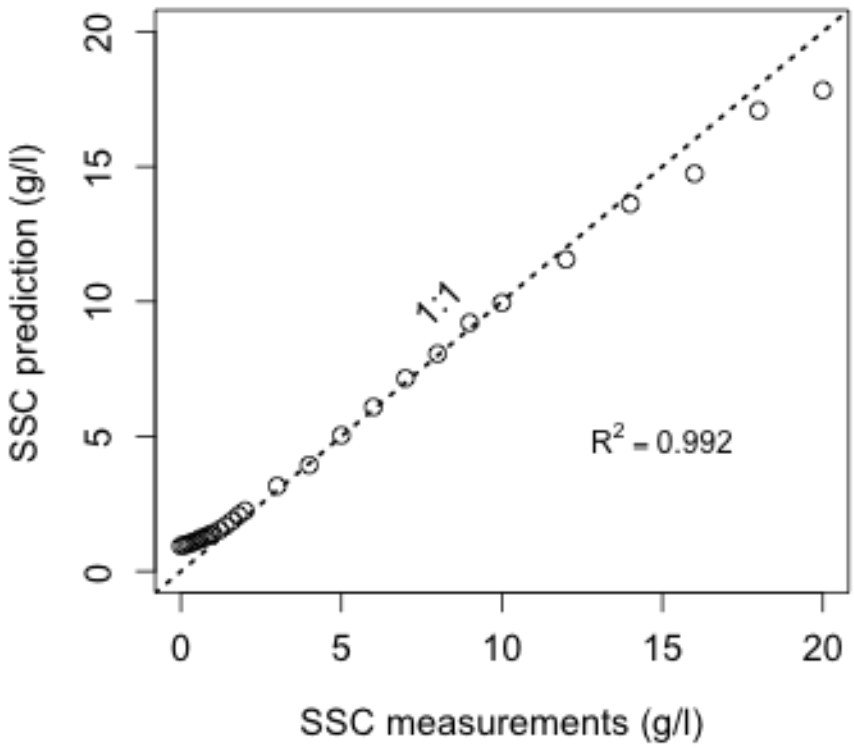

Figure 3.8: The predicted SSC for natural sediment from YL using the Spectral mixing model and parameters from sediment of HYK. The prediction were applied to 0 20 g/l according to the predicable range of SSC from Eq. (3.9) (21.15 g/l for YL natural sediment)

also indicated that an empirical approach based on the correlation between SSC and reflectance is inadequate for water bodies with SSCs higher than 20 g/l.

The relationship between SSC and reflectance became nonlinear when SSC is particularly high. Ritchie and Zimba (2005) reported that the reflectance at almost all wavelength were linearly related to SSC when SSC is between 0 and 0.05 g/l. For the best correlation along the wavelengths or the available bands from a satellite image. This threshold from linear to nonlinear was reported to be 0.6 g/l in a laboratory study by Harrington Han and Rundquist (1994), 0.5 g/l by using Landsat MMS Band 3 according to Harrington Harrington Jr et al. (1992), and 0.6 g/l by using MODIS Band 2 according to Wang and Lu (2010). Our findings indicated that SSC and reflectance followed an exponential law (Eq.3.7). The derivative of reflectance with respect to SSC measures the sensitivity of Rr to SSC.

$$Rr' = \frac{C_1 e^{-\frac{SSC}{C_0}}}{C_0} \tag{3.20}$$

Reflectance and SSC may be linear only if Rr' is almost constant. With acceptable accuracy for practical use (such as: 5% relative errors involved), a linear relationship could be valid under the following condition:

$$Rr' >= 0.95\frac{C_1}{C_0} \tag{3.21}$$

By solving the conditional equation, a linear relationship between SSC and Rr can be reasonably approximated when the following was true:

$$SSC <= 0.051 C_0 \tag{3.22}$$

The SSC threshold that denoted the progression of the correlation between SSC and reflectance from linear to nonlinear was represented by coefficient C_0 in Eq.3.7. The thresholds from linear to nonlinear were 0.44 ($= 0.051 \times C_0$) g/l and 0.35 ($= 0.051 \times C_0$) g/l for HYK and YL sediments in the laboratory setting, respectively, in Landsat(TM ETM+) band 4 (C_0 corresponded to the coefficients in Table 3.2).

3.4.2 Spectral Mixing Algorithm and Limits

Our result confirmed that the sediment type influences the relationship between SSC and reflectance (Chen et al., 1992; Novo et al., 1989b). We suggested the use of an spectral mixing algorithm model for use in large rivers given the increased certainty introduced by sediment varieties. The research of Oyama et al. (2007, 2009)'s research on the remote sensing of chlorophyll α concentrations and non-phytoplankton suspended sediments demonstrated that the spectral mixing modeling approach ($R^2 = 0.96$) estimated non-phytoplankton suspended sediments (1 mg/l to 100 mg/l) more accurately than the traditional empirical model (1 mg/l to 100 mg/l). Our result confirmed that the spectral mixing algorithm can enhance the relationship of reflectance and SSC up to 21 g/l (HYK sediment). The advantage of the spectral mixing algorithm is to combine the SSC estimation curves for different sediment groups (Figure 3.7) when the spectral measurement of saturated level in the Rr-SSC curve represented the standard reflectance spectra of sediment.

The possible influence of chlorophyll, CDOM, or detritus on the optical properties of the water had not been considered in the current study because the samples used in the study were made with distilled water and dry sediment. Clean water ($SSC \approx 0$) from a river may be low in suspended sediment content but still contain

other substances. Thus, the effects of other constituents may be estimated in future studies. The careful selection of image-derived standard water reflectance spectra in spectral mixing algorithm enhanced the possible application of this method in natural water bodies such as rivers if water quality related components (aside from suspended sediments) in the Yellow River were constant.

SSC in the Yellow River was collected from point-integrated samples that collected at relatively water depth of 0.2, 0.6 and 0.8 (Ministry of Water Resources of China, 1992). In this study, we assumed a depth integrated, constant SSC throughout the water column without consideration to variations in depth. The effect of this simplification on SSC compared with the measurements from the traditional sampling method should be evaluated further.

3.5 Conclusion

Two basic questions regarding the estimation of SSC in the highly turbid Yellow River by using remote sensing were addressed. First, the the up limit of SSC that accommodates the application of the remote sensing method is determined. The results of our experiment on sediment from the Yellow River indicated that the SSC remote sensing model may be applied to SSCs of up to 21 g/l for the finer HYK sediment and 15 g/l for YL sediment that are relatively coarse. This value is also the limit for any correlation-based empirical model. Landsat (TM ETM+) Band 4 is recommended in SSC estimation if a single-band model is using in the Yellow River. Second, the effect of sediment types on the SSC remote sensing model is clarified and addressed. The particle size distribution in sediment evidently affects the relationship

between SSC and reflectance. A spectral mixing algorithm model was proposed in this study that can integrate the correlations for all available satellite bands and reduces the variations caused by sediment types variety in the model parameters. This spectral mixing algorithm is promising to remotely sense the SSC over the extensive stream reach of the Yellow River by using onsite spectral measurement or satellite imagery.

Table 3.3: The statistic summary of fitted SSC model between SSC and Spectral Mixing Index of Sediment (SMI_s)

Sediment Type		**Huayuankou (HYK)**			**Yangling (YL)**		
		Estimate	Standard Error	F Value	Estimate	Standard Error	F Value
Natural	a	0.94	0.087	118.2***	0.98	0.214	21.1***
	b	3.43	0.110	965.9***	3.17	0.250	160.9***
	R^2	0.993			0.966		
	$F_{(\text{ANOVA})}$			1803.49***			387.88***
Sand	a	0.92	0.065	196.5***	0.87	0.086	102.7***
	b	3.48	0.086	1636.5***	3.57	0.119	879.9***
	R^2	0.996			0.994		
	$F_{(\text{ANOVA})}$			3672.03***			2136.96***
Silt	a	0.32	0.069	21.2***	0.58	0.117	24.0***
	b	4.28	0.237	325.8***	3.80	0.233	264.4***
	R^2	0.998			0.985		
	$F_{(\text{ANOVA})}$			1099.03***			861.07***
Clay	a	0.30	0.084	13.0***	0.21	0.104	3.9**
	b	4.36	0.306	202.9***	4.71	0.551	73.2***
	R^2	0.978			0.963		
	$F_{(\text{ANOVA})}$			602.69***			350.16***

[1] The coefficients were regressed by Eq.(3.16) as $SSC = a\ e^{b\ SMI_s}$, SSC was the suspended sediment concentration (g/l) and SMI_s was the spectral mixing index of sediment. For application of logarithm transformed SSC and SMI_s as Eq.(3.17): $\ln(SSC) = A + B\ SMI_s$, the coefficient were $A = \ln a$ and $B = b$. $*$, $**$,$***$ denotes level of significant at 0.05, 0.01, 0.001, respectively.

[2] For regression ANOVA, the statistic F has an F distribution with degrees of freedom equals to m number of explanatory variables and $N - 2$ (N is the total degree of freedom that 29 as the sample size for regression). $\int_0^{F_a} F(m,n)\mathrm{d}v = 1 - \alpha$, $m = 2$ and $n = 27$ are degree of freedom for model and variable, respectively. The F_α at significant level (α) being 0.05, 0.01and 0.001 are 3.49, 8.77, and 9.95 respectively.

Chapter 4

Field Spectral Survey on the Yellow River

Abstract

The dynamic sediment distribution on large rivers with dams constructed often attract wide attention due to their possible adverse environmental impacts. Sedimentation modeling and environmental consequence of man-made projects are often hindered by the lack of sediment measurements with spatial details. This study aimed to investigate the method to estimate the suspended sediment concentrations (SSCs) from on-site spectral measurements. The study investigated the spectral signature of river water from the natural channel and Sanmenxia reservoir on the Yellow River. A field spectral survey was conducted with on-site spectral measured by a spectraoradimeter and SSCs by sampling. Reflectance at 750 nm to 950 nm, with all r between SSC and reflectance being above 0.7, seemed to be the proper range for SSC esti-

mation. Simulated Landsat ETM+ band 4 (760 nm to 900 nm) was employed to build the single band model for estimating SSC. The result confirmed that the exponential model based on the relationship between SSC and reflectance ($R^2 = 0.92$, RMSE=0.241 g/l) were better than the linear model between reflectance logarithm transformed SSC ($R^2 = 0.90$, RMSE=0.310 g/l). We also apply the Spectral Mixing Algorithm (SMA) from the tank experiment to the on-site spectral measurements. The result shows the SMA models were performed as better as the single band exponential model ($R^2 = 0.86$, RMSE=0.280 g/l) but the valid range for application was improved from 1.99 g/l to 347 g/l. This study could provide critical instructional assistance for estimating SSC directly from remote sensing data.

4.1 Introduction

Spatial and temporal information of suspended matter in rivers is the essential to study sediment-associated environmental changes such as alterations of channel morphology, degradation of water quality, and construction and operation of on-river hydrological facility (Schiebe et al., 1992; Wang and Lu, 2010; Walling et al., 2008). Globally, *in situ* sampling and laboratory analysis is the most commonly used method for sediment observation (Edwards and Glysson, 1988; Wren et al., 2000). This method is labor intensive and time consuming, and the spatial coverage of the monitoring is limited to sparse points. As Syvitski et al. (2000) indicated, most rivers in the world have either not been gauged, or their sediment data are not readily available. Although the Yellow River is one of the five rivers (Yellow, Yangtze, Mississippi, Haihom, and Danube) that have the delivery of sediment adequately documented

(Milliman and Meade, 1983), the adjacent monitoring stations are usually hundreds kilometers apart.

The remote sensing method for SSC monitoring, in the spatial context, is promising to provide synoptic, continuous, and regional observation. The foundation of remote sensing approach for SSC estimation is that the amount of sediment in water directly affects the reflectance of solar radiation in the visible and near-infrared portions of the spectrum. In general, the more the suspended sediments in water, the higher the reflectance usually is (**?**Ritchie et al., 2003).

Most current studies developed unique empirical relationships by relating field measurements of SSC to reflectance data from satellite imagery. However, the exact form of the relationship between SSC and reflectance also depends on the mineralogy, color, and size of the sediments (Bowers and Binding, 2006; Novo et al., 1989b). Because these factors can be highly various in natural environments, the applicability of an SSC-reflectance relationship is usually limited to the setting where the data were collected. Long and Pavelsky (2013) compared 31 published empirical model between SSC and reflectance using *in situ* measurements, their results suggested the potential for spatial transferability of SSC-reflectance models have to meet three criterions: (1) the use of a combination of a near infrared band with one or more visible bands, (2) development based on SSCs with a maximum similar to the maximum SSC observed in the target area, and (3) a nonlinear equation form.

Qu et al. (2014, Under Review) conducted an experiment to examined the SSC-reflectance curve from 400 nm to 1000 nm in the laboratory with designed SSC being up to 40 g/l. A physical-based exponential model (Schiebe et al., 1992) was proposed to present the relationship between SSC and reflectance. To apply the correlations at all wavelength/bands and to eliminate the effect from variations of the sediment

types, they introduced a spectral mixing algorithm (SMA) approach to estimate the SSC. The foundation of the SMA approach is that the spectral radiance/reflectance of a volume of turbid water can be conceptualized to the weighted sum of the primary components in water such as clear water, non-phytoplankton suspended sediments (NPSS), and phytoplankton(Oyama et al., 2007, 2009; Goodin et al., 1993). There are two key steps in the SMA approach. First, to translate the reflectance at each band to spectral mixing index based on the assumption that the mixed reflectance spectrum of a given pixel is a linear combination of the primary components in water. Second, to apply the spectral mixing index of sediment (SMI_s) from the first step to the conventional SSC estimation model, in which the single band reflectance, band ratio, and arithmetic calculation of bands were widely used.

To apply the SMA approach developed in the laboratory to a general natural setting, the applicability and transferability of the model should be investigated. The Sanmenxia Reservoir($111°8'10.32''E$, $34°47'33.36''N$) (Figure 4.1) on the Yellow River exhibits a wide range of SSCs with water body extended from the reservoir to the natural channel. It is an ideal setting for studying the transferability and application of SSC-reflectance model obtained from the laboratory. The present study focused on highly turbid water between the natural channel and the reservoir of Sanmenxia on the Yellow River. Through *in situ* spectral and SSC measurements on the rivers, this study aimed to measure the reflectance spectra of the turbid waters in natural condition, to correlate measured spectral data with sampled SSC, and to establish the model for estimating the SSC by using spectra data.

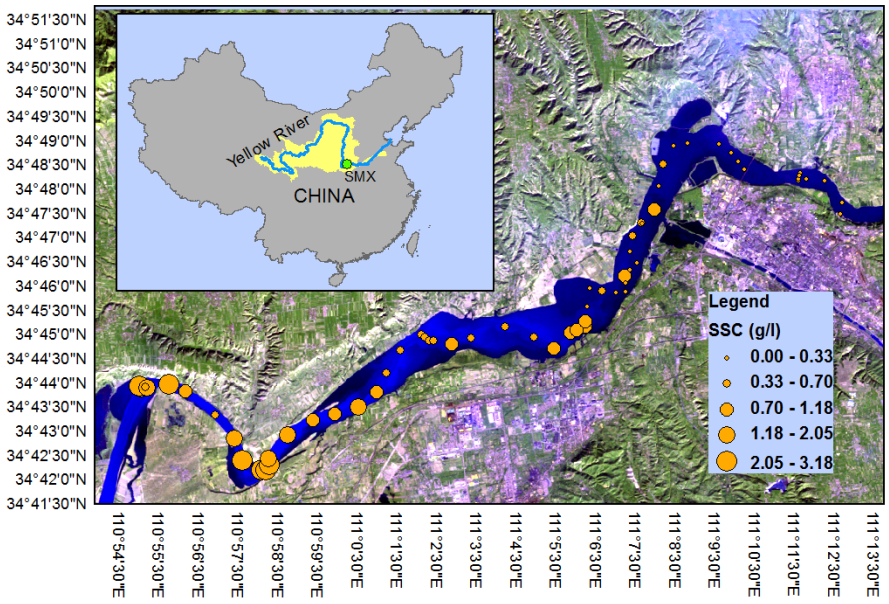

Figure 4.1: Study Area

4.2 Materials and Methods

4.2.1 Study Area and Field Measurements

A field survey were carried out by a sampling boat on 15 Nov 2011 to collect the on-site spectral data and water samples for SSC measurement in laboratory. The field survey were carried out on Sanmenxia reservoir ($111°8'10.32''E$, $34°47'33.36''N$), and 20 km up to the natural channel of the Yellow River (Figure 4.1). The geographic locations for spectral measurement and water sampling were recorded by using a GPS receiver. Field spectral data were collected using ASD FieldSpec® HandHeld 2^{TM} spectroradiometer (ASD Inc. Boulder, Colorado, USA), which measures radiance between 325 nm and 1075 nm at 1 nm intervals. Three reflectance measurements

were collected at each location, and the mean value were used to obtain reflectance for each sampling site.

A 5"×5" spectral reflectance panel (SRM-990 Spectralon®, LabSphere, Inc. North Sutton, NH) was served as the calibration standard for converting the radiance to reflectance. The panel diffusely reflects nearly 100% of the incident light throughout the spectral range. The wavelength specific reflectance $Rr(\lambda)$ was calculated using the following equation:

$$Rr(\lambda) = \frac{L(\lambda)}{L_0(\lambda)} Cal(\lambda) \tag{4.1}$$

where: $L(\lambda)$ is the wavelength-specific radiance from the water surface, for each sample, which is measured by the spectroradiometer three time. $L_0(\lambda)$ is white reference that is collected by putting the reference panel above the water surface. The white reference is updated before each measurement of water sample. $cal(\lambda)$ is the calibration factor for reflectance panel that come out with the product.

At each location, a water sample was collected near the surface (20 cm in depth) immediately after the measurement of spectral data. To calculate SSC (g/l), the samples were oven-dried at 105°C for 12 hours and weighed before and after at the Sanmenxia hydrological station.

4.2.2 Data Analysis

We used the Pearson correlation coefficient (r) to indicate the correlation between studied variables (reflectance and SSC). To show the performance of regression models, we employed root mean square error (RMSE) (Wang and Lu, 2010). The Pearson correlation coefficient and RMSE were also used to compare different models. The R (R Core Team, 2013) plotbox tool was used to detect the outliers.

4.2.3 Spectral Mixing Approach

The spectral radiance/reflectance of a volume of turbid water can be conceptualized to be composite signal from the weighted sum of the primary components in water such as clear, non-phytoplankton suspended sediments (NPSS), and phytoplankton (Goodin et al., 1993). In our study, we considered two primary optical active consistent of water and sediment in the river water. The reflectance mixing equation is:

$$Rr_i = P_{si}SMI_s + P_{wi}SMI_w \tag{4.2}$$

where SMI_w and SMI_s are spectral mixing index of water and sediment, respectively, which are directly related to their masses/concentrations. P_{wi} and P_{si} are the standard reflectance spectra of water and sediment, respectively, which represent the standard reflectance spectra (water and sediment in this study).

The spectral mixing algorithm in our study involves two key steps. First, to translate the reflectance at each band to spectral mixing index based on the assumption that the mixed reflectance spectrum of a given pixel is a linear combination of the primary components in water. Second, to apply obtained spectral mixing index of sediment (SMI_s) in the first step to the SSC estimation model, in which the single band reflectance, band ratio, and arithmetic calculation of bands were widely used in conventional methods.

The selection of standard reflectance spectra of water(P_{wi}) and sediment(P_{si}) is very crucial. The spectral measurements of clean water and dry sediment (shown in Figure 4.2) were adopted as the standard reflectance spectra in this study.

4.3 Results

4.3.1 Spectral Characteristics of Sediment Laden Water

The valid spectral range of the spectroradiometer seemed to be about 400 nm to 950 nm according to our measured spectral data. Beyond this range, the signals displayed notable variations with wavelength. Hence, only the wavelength range between 400 nm and 950 nm was considered to determine water reflectance in this study. Figure 4.2 shows typical reflectance spectra measured in the field. Reflectance increased with increasing SSC between 400 nm and 950 nm, particularly between 550 nm and 850 nm. The peak reflectance was quite different among samples with different SSC values. For example, the peak reflectance was 0.18 g/l for SSC being 0.06 g/l and 0.26 g/l for SSC being 3.05 g/l.

In addition, the wavelength of peak reflectance shifted toward longer wavelength with increasing SSC. In general, there were two reflectance peaks for each spectrum; one was between 550 nm and 700 nm, and the other was between 750 nm and 850 nm. For the samples with very low SSC (e.g. $SSC = 0.06\ g/l$), the second peak was not stand out due to strong absorption of water. With increasing SSC, the two peaks increased, but the second one increased more than the first one did. Consequently, the second reflectance peak became higher than the first one when SSCs were higher than 1.18 g/l.

We use the Pearson's correlation coefficient (r) to indicate the correlation between SSC and reflectance along the wavelength. At each wavelength from 325 nm to 1075 nm with 1 nm interval, the Pearson's correlation are shown in Figure 4.3. Reflectance at 750 nm to 950 nm, with all r between SSC and reflectance being above

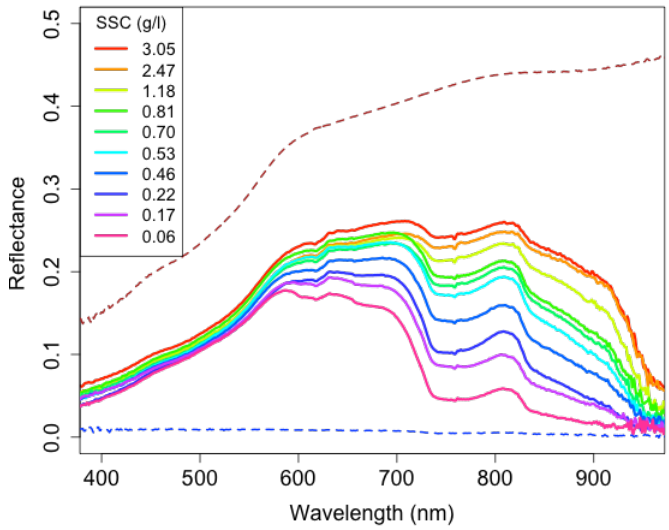

Figure 4.2: Reflectance profiles of samples with increasing SSC

0.7, seemed to be the proper range for SSC estimation.

To investigate possible relationship between water reflectance and SSC, 11 bands were simulated with even bandwidth of 50 nm from 400 nm to 950 nm (i.e. $Band\,1 : 400 - 450\ nm$, $Band\,2 : 450 - 500\ nm$, $Band\,3 : 500 - 550\ nm$, $Band\,4 : 550 - 600\ nm$, $Band\,5 : 600 - 650\ nm$, $Band\,6 : 650 - 700\ nm$, $Band\,7 : 700 - 750\ nm$, $Band\,8 : 750 - 800\ nm$, $Band\,9 : 800 - 850\ nm$, $Band\,10 : 850 - 900\ nm$, and $Band\,11 : 900 - 950\ nm$). The Figure 4.4 showed the scatter plots between SSC and reflectance for the simulated 11 bands. The nonlinear exponential trends showed up gradually from Band 1 to Band 10 with Pearson's correlation coefficient being 0.2477, 0.1994, 0.1945, 0.3136, 0.4629, 0.5257, 0.6791, 0.7474, 0.7651, 0.8317, and 0.8832. From Band 1 to Band 6, the trends were not very obvious with fluctuation at low SSCs. From Band 7, the trends between SSC and reflectance became very obvious. It means that the reflectance at wavelength above 700 nm are the effective

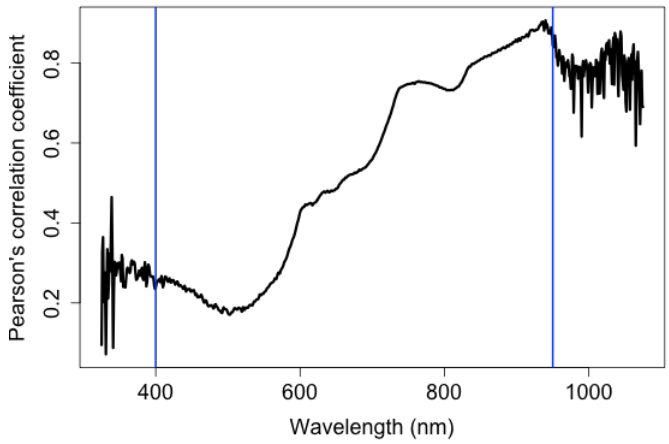

Figure 4.3: Correlation coefficient between SSC and Reflectance

bands to indicate the SSC.

To further investigate the possible relationship for application with available satellite image, we choose to simulate the visible and near infrared bands of Landsat ETM+ ($Band\,1 : 450 - 520\ nm$, $Band\,2 : 520 - 600\ nm$, $Band\,3 : 630 - 690\ nm$, and $Band\,4 : 760 - 900\ nm$). The Figure 4.5 showed the scatter plots between SSC and reflectance for simulated Landsat bands. The SSC and reflectance shows non-line an exponential relationship. And similar to the 10 bands simulation, the trends became more and more clear from Band 1 and Band 4 with Pearson correlation coefficient being 0.1942, 0.2811, 0.5077, and 0.7846. It was obvious that Band 4 showed the best correlation.

Most scatter plots for these bands including 11 bands set and Landsat bands (Figure 4.4 and Figure 4.5) showed non-linear trend between SSC and reflectance, especially at bands with wavelength $> 600\ nm$ that include Band 5 to Band 11 for 11 bands setting and Band 3 and Band 4 for Landsat setting.

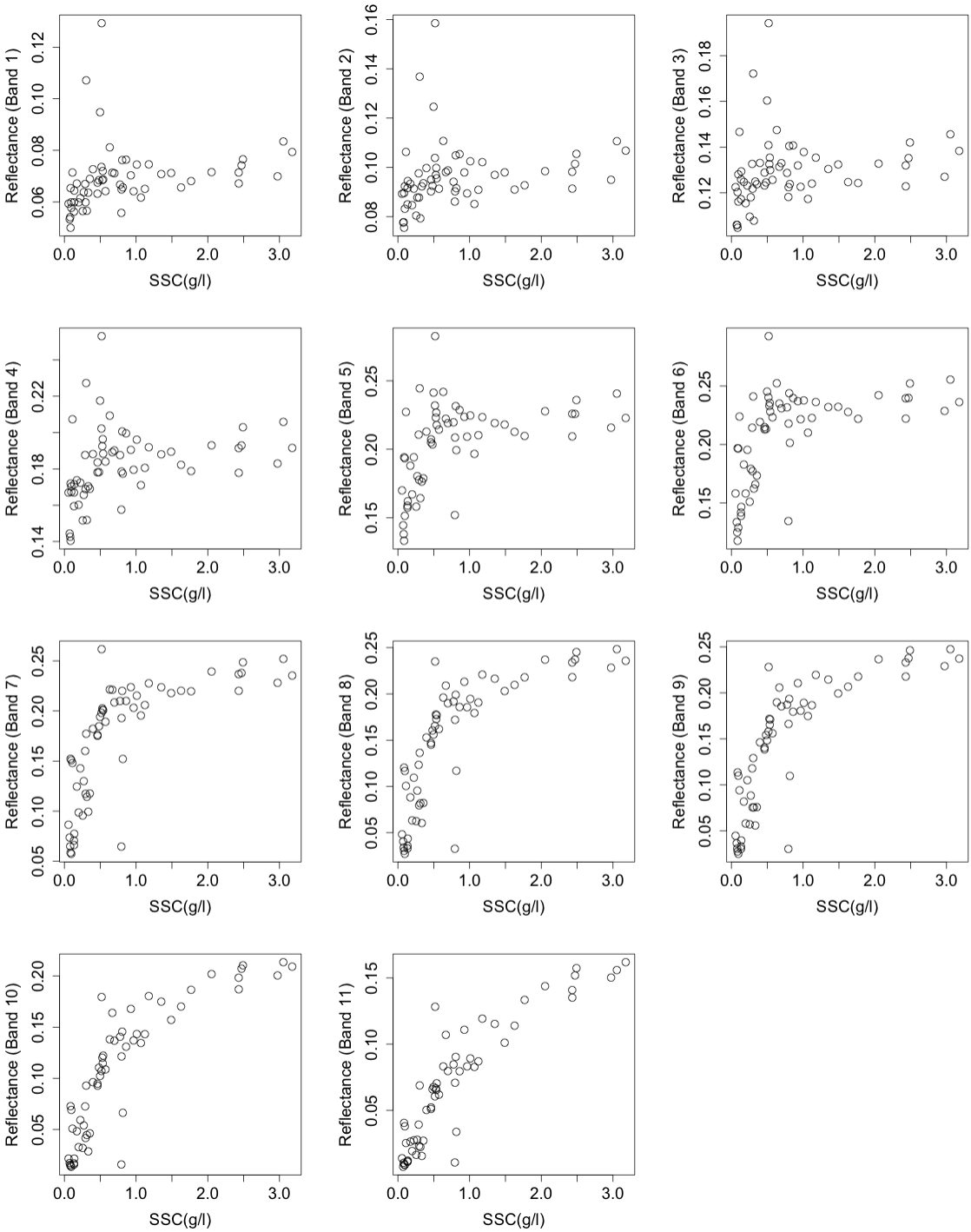

Figure 4.4: Scatter plots of Reflectance and SSC on 11 bands from 400 nm to 900 nm

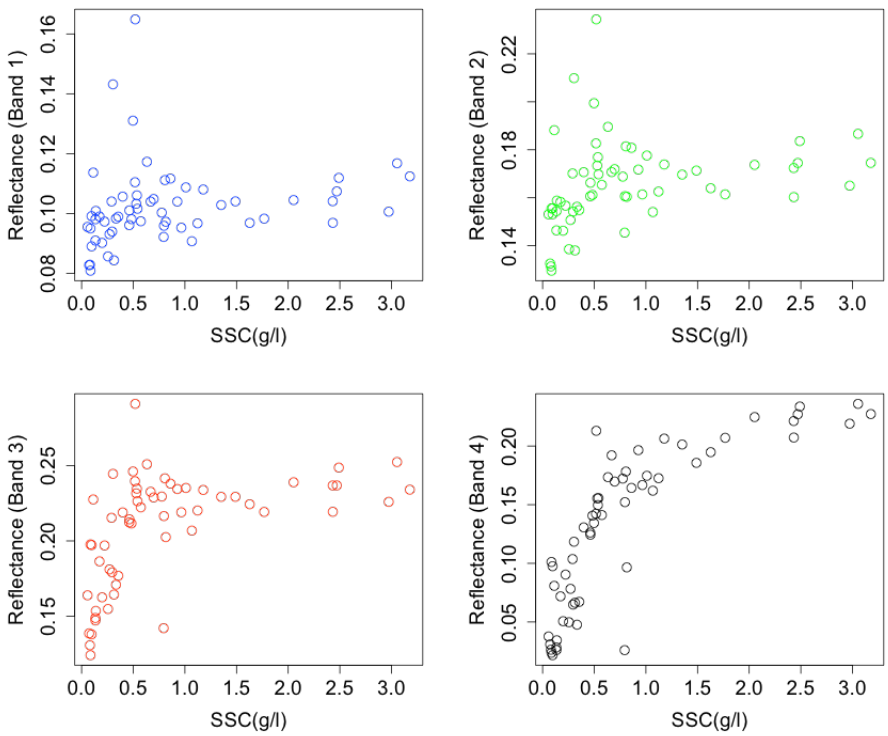

Figure 4.5: Scatter plots of Reflectance and SSC on 4 simulated Landsat bands

4.3.2 Single Band Model

In previous tank experiment, we interpreted the relation between SSC and reflectance by a physical-based exponential model well ($R^2 > 0.9$) as Eq.(4.3).

$$Rr(\lambda) = C_1(\lambda)(1 - e^{-\frac{SSC}{C_0(\lambda)}}) \tag{4.3}$$

where $Rr(\lambda)$ is wavelength-specific reflectance, $C_1(\lambda)$ and $C_0(\lambda)$ are wavelength-specific coefficients. Because the Landsat band4 shows the best correlation among all 4 bands, Band 4 were employed to build a single band model according to Eq.4.3. It could be written as

$$Rr_{B4} = C_1(1 - e^{-\frac{SSC}{C_0}}) \tag{4.4}$$

where Rr_{B4} is reflectance at Landsat Band 4, and C_1 and C_0 becomes constant.

Figure 4.6 (a) showed the Landsat band 4 reflectance and SSC. Figure 4.6(b) was the boxplot of residual of the exponential model [Figure 4.6(a), dashed line] between Landsat band 4 reflectance and SSC. According to the box plot statistics, the extreme of the lower whisker, the lower hinge, the median, the upper hinge and the extreme of the upper whisker were -0.050, -0.013, 0.004, 0.016, and 0.041. Among the 60 samples, there were samples #15, #17, #24, #30 and #52 [Figure 4.6 (a) marked in red] that were far apart from the other points, and the residual of these points were out the notches [Figure 4.6 (b) marked in red]. We considered these points out the extreme whisker in the boxplot outliers and excluded them in further analysis. In Figure 4.6 (a), the dashed line was the fitting by regression model using all 60 samples and the solid line represented the regression without outliers. The two fitting curves were close to each other and overlapped when the SSCS were relatively small($< 1.0\ g/l$), while the coefficient of the determination R^2 was improved from 0.785 (all samples) to 0.925 (outliers excluded).

Because the exponential model is not an extrapolation model, it could only predict SSC with corresponding reflectance less than $C_1(= 0.223\ g/l)$. In other word, the predictable SSC value were approximate $1.99 g/l$ that was estimated by the logarithm transformed linear model.

$$ln(SSC) = aRr_{B4} + b \tag{4.5}$$

where a and b were regression coefficients. We also built a linear model between logarithm transformed SSC and reflectancer Eq.(4.5). Figure 4.7 showed the regression

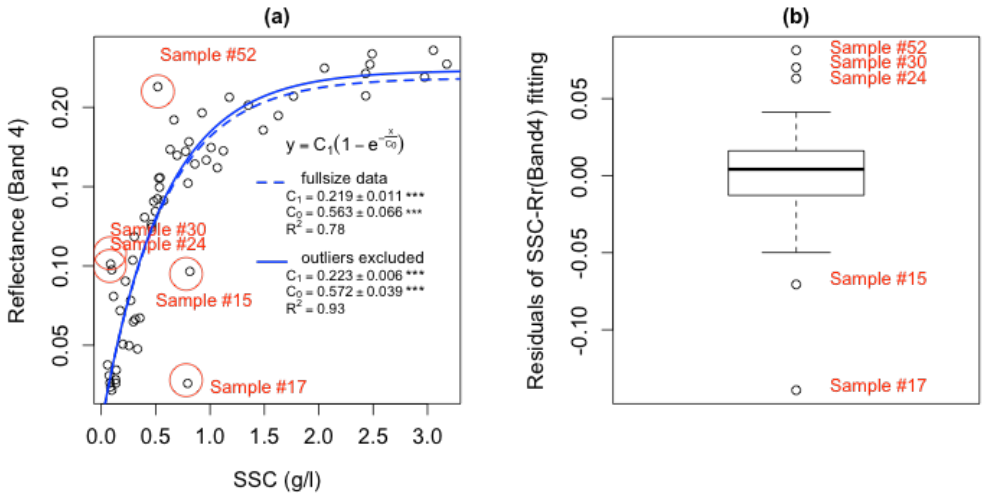

Figure 4.6: (a) the observation and regression of exponential model between SSC and simulated Landsat reflectance (Band 4). The dashed line was fitting using all field samples, and the solid line was fitting with outliers (circled) excluded, (b) boxplot of residual of the exponential model (dashed line) between Landsat band 4 reflectance and SSC. The hinges were versions of the first and third quartile, and the notches extend to $\pm 1.58\frac{IQR}{n}$, n is the sample size and IQR is then inter quantile range.

of the logarithm transformed model.

Figure 4.8 showed the comparison between observed and predicted SSCs for both logarithm transformed linear model and exponential model. The solid line in red was the $1:1$ reference line. As indicated, the logarithm model seemed overestimate SSC and the exponential model underestimated SSC. The coefficient of the determination (R^2) of the two models have no remarkable difference. It means that the logarithm transformed linear model is adequate compared to more complex exponential model when the single band information is employed.

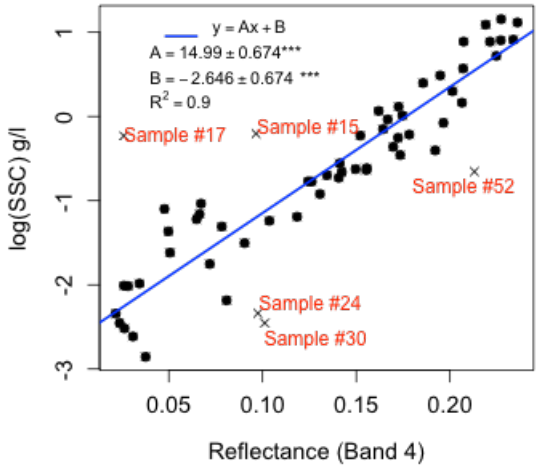

Figure 4.7: Regression of the logarithm transformed model by using the outliers excluded data. The outliers detected by using the exponential were marked

4.3.3 Model based on Spectral Mixing Algorithm

We applied the SMA approach to the field spectral measurements for simulated Landsat bands. Accordingly, Eq.(4.4) could be written into:

$$SMI_s = C_1(1 - e^{-\frac{SSC}{C_0}}) \tag{4.6}$$

where C_1 and C_0 are regression coefficients, SMI_s replace the Rr_{B4} in Eq.(4.4) to integrate the information at all available bands. Or, Eq.(4.6) could be transformed to an explicit form for SSC estimation:

$$SSC = C_0 lnC_1 - C_0 ln(C_1 - SMI_s) \tag{4.7}$$

Figure 4.9 was the simulated SMI_s in which the the spectral measurements of

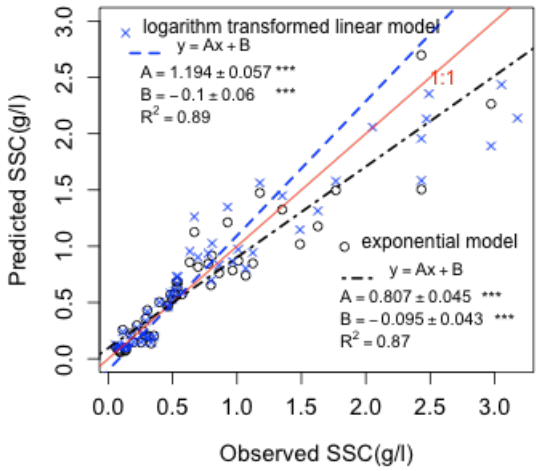

Figure 4.8: The comparisons between predicted and observed SSCs. The crosses and the dashed line were for logarithm transformed linear model and the circles and the dash-dot line were for exponential model.

clean water of dried sediment (shown in Figure 4.2) were adopted as the standard reflectance spectra. The solid line in Figure 4.9(a) was the regression curve by Eq. (4.6), while Figure 4.9 (b) indicated the comparison between predicted and observed SSCs. The comparison between predicted and observed SSC (dashed line in blue) was almost overlapped with the 1 : 1 reference line (solid line in red) with the slope being 0.983 ($R^2 = 0.86$).

4.4 Discussion and Conclusion

This study investigated how water reflectance varied with SSC at wavelength from 350 nm to 1100 nm by using the SSC and spectral measurements through a field survey conducted on the Yellow River.

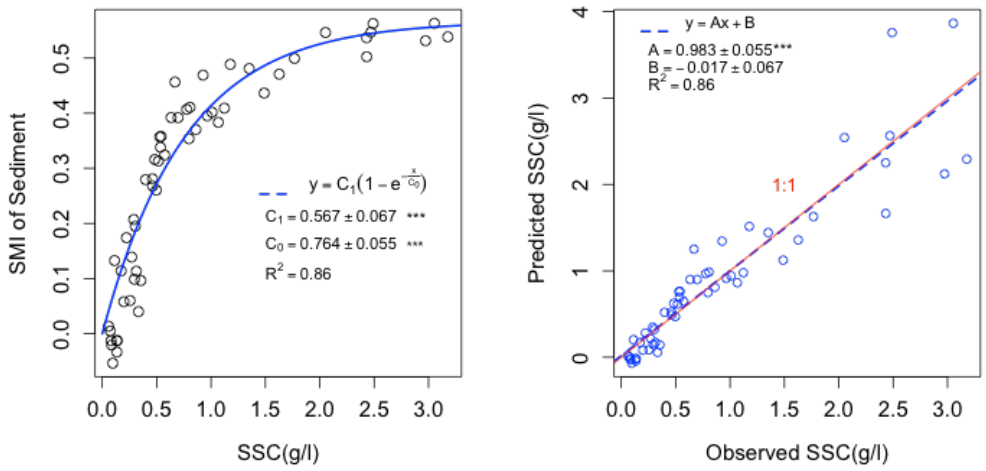

Figure 4.9: The relationship between SSC and Spectral Mixing Index of sediment (SMI_s), which were simulation using the reflectance of dry sediment as standard reflectance spectra of sediment(from Tank experiment)

Our results showed that reflectance at the wavelengths from 850 nm to 930 nm showed a strong correlation with Pearson correlation coefficient (r) all above 0.7. This result was consistent with Wang's studies on Yangtze River Wang et al. (2009b); Wang and Lu (2010), in which near-infrared (NIR) band was reported as the SSC indicator in turbid waters. They suggested that Landsat Enhanced Thematic Mapper Plus (ETM+) Band 4 (760 nm to 900 nm) and Terra Moderate-resolution Imaging Spectroradiometer (MODIS) Band 2 (841 nm to 876 nm) provide a relatively accurate SSC estimate in Yangtze River.

Based on our study, reflectance from 850 nm to 930 nm was recommended for SSC estimation model. Past studies suggest that linear relationships are effective for remotely sensing SSCs less than 0.05 g/l, but for values greater than this, curvilinear relationships are necessary Ritchie et al. (2003). With SSC being up to 3.1 g/l, we found that the water reflectance tended to increase with SSC asymptotically. In other

word, the increasing rate of reflectance went down and approached an asymptotic value [C_1 in Eq. (4.4)], close to which the reflectances showed no remarkable changes while the sediment load in water kept increasing. This finding is corroborated by past studies, which have found that different models are optimal for low and high SSCs Ritchie et al. (2003) or that models that work well at low concentrations can saturate at higher concentrations Ritchie et al. (2003); Chu et al. (2009); Ritchie and Cooper (1988); Topliss et al. (1990).

In our study, an exponential model and a logarithm transformed linear model were built for applications in the Yellow River. We established the models for the commonly used Landsat imagery that holds the longest time series data and public accessible. The field spectral measurements were simulated to band-integrated reflectance for Band 4 of Landsat TM/ETM+ setting. The regressions between the sampled SSC and simulated reflectance were then used to parameterize the models. There is no significant difference between the exponential and logarithm transformed linear model with R^2 being 0.93 and 0.90, respectively, which was also supported by the comparison between predicted SSC and observed SSC. The logarithm transformed linear model is advantageous for the application purpose with a simple format and capability of extrapolation use. The exponential model, however, was only valid when the reflectance measurement from the potential targets is within the saturation level that is approximately equal to C_1 of the exponential model.

Previous studies Ritchie et al. (2003); Topliss et al. (1990) indicated that multispectral models are preferable for remotely sensing SSC. Long Long and Pavelsky (2013) also suggested a near infrared band and a visible band used in combination (or other combinations) are more effective than a single band used alone. We introduced a spectral mixing algorithm to apply the multispectral information for estimating

the SSC. Because the reflectance of dry sediment and clean water was used as the standard reflectance (end-member) of the spectral mixing algorithm, the valid range of the exponential model between SSC and SMI_s is improved from reflectance being 0.219 to SMI_s being 0.567. The corresponding SSC are approximately 1.99 g/l and 347 g/l, respectively, according to the logarithm transformed linear model. Comparison between observed and predicted SSC showed that the exponential model with the spectral mixing algorithm obtained the best result in our study. The fitting between predicted SSCs and observed SSCs are almost overlapped with the 1:1 reference line while the slope of the fitting being 0.983 and the parameter for intersection is not significant.

This field study provided critical physical basis and instructional assistance for estimating SSC directly from satellite images in highly turbid rivers in terms of sensor selection, band selection, equation determination, as well as error analysis and reduction.

Chapter 5

Application of Spectral Mixing Algorithm to Landsat ETM+

Abstract

Using remote sensing to estimate suspended sediment concentrations (SSC) in inland waters has been less successful than for oceanic, coastal, and lake waters. In this study, we developed a spectral mixing algorithm for quantifying SSC in highly turbid inland waters. The daily SSC measurements from the field monitoring and satellite data from Landsat 7 ETM+ were used for developing an spectral mixing algorithm to remotely sense SSC in the Yellow River. The results showed that the relationship between SSC and an integrated spectral mixing index of sediment (SMI_s) that was derived from reflectance by using the spectral mixing approach, was more accurate and applicable than those from the conventional regression methods ($r = 0.71$ vs. $r = 0.62$, respectively). Our study indicated that the consideration of the two

primary components (water and sediment) in spectral mixing algorithm was adequate to estimate SSC in the Yellow River. Our study also showed that the satellite image-derived standard reflectance spectra of reference natural clean water could reduce the effect from lack of information on phytoplankton. We also used a spectral mixing algorithm based remote sensing approach to map out the SSC along the river for different seasons. These results indicated a high potential for the spectral mixing algorithm in effectively separating contribution of different primary components on the total reflectance.

5.1 Introduction

The Yellow River in China (Figure 5.1) is the fifth largest river in the world, and it is ranked the second in terms of sediment loads (10.8×10^8 ton/yr), contributing 6% of the estimated global river sediment flux to oceans (Milliman and Meade, 1983). Climate change and human activities have dramatically changed the physical and ecological structures of the river. Since 1950 the sediment load delivered by the Yellow River into the ocean has started to decrease due to various causes including climate change and damming of the river (Pang et al., 2011; Peng et al., 2010; Walling and Fang, 2003; Wang et al., 2007). The average sediment load into the sea was 6.53×10^8 $ton/year$ from 1960 to 2000. The amount has decreased to 1.51×10^8 $ton/year$ in the period from 2000 to 2005 (Pang et al., 2011). For such a river, knowledge on the transport mechanisms of suspended sediment is important for understanding the hydrologic, geomorphologic, and ecologic functioning of the river.

Suspended sediment concentration (SSC), the mass of sediment entrained within

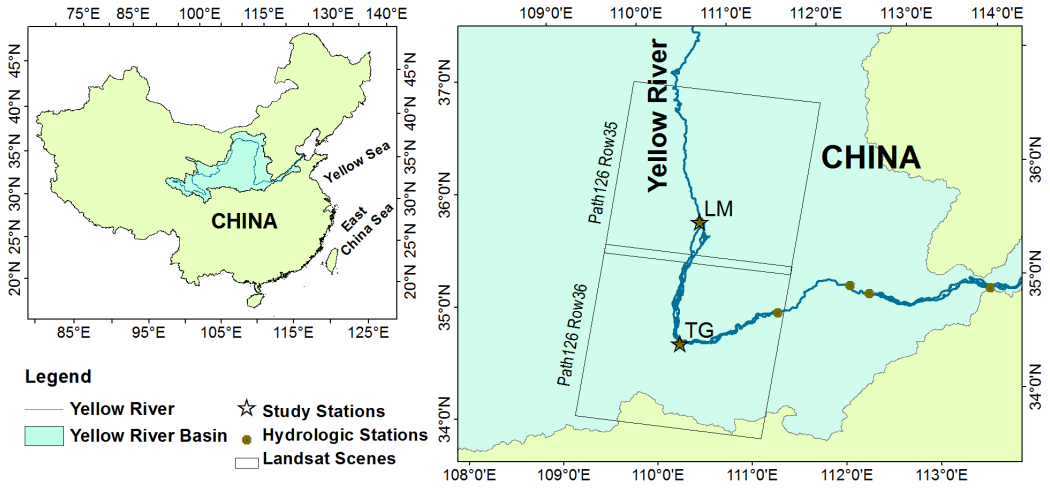

Figure 5.1: Map of the Yellow River basin showing the location of gauging stations along the mainstream

a unit volume of water, is a common measure of sediment transported in overland and river flows (Gray et al., 2000; Glysson et al., 2000). Because it is costly to build and maintain a SSC monitoring system, most of the world's rivers do not have suspended sediment data readily available. Of the rivers that have been gauged, not all have sediment being monitored (Syvitski et al., 2000). The Yellow River is among the only five large rivers (Yellow, Yangtze, Mississippi, Haihom, and Danube) that have adequate sediment data (Milliman and Meade, 1983). The current hydrologic monitoring system for collecting precipitation, discharge, and sediment data on the Yellow River was established in 1930s, though the earliest record can be traced back to 1919 at some locations (Yellow River Conservancy Commission, 2011).

However, the conventional *in situ* sampling method (Edwards and Glysson, 1988) still remains the main tool for sediment observation that is time consuming, labor intensive, and provides only point data. With constraints of sparse spatial and temporal sampling, data from the conventional ground observation were not enough for establishing sediment balance models (Walling and Fang, 2003). Since a long-term

effort to characterize the physical processes of the river flow and sediment discharge patterns of the Yellow River has been conducted with an annual Water Sediment Regulation Scheme (WSRS), whereby a controlled release of floodwaters from the Xiaolangdi Reservoir is used to expel sediments deposited in the reservoir and to scour the lower reaches of the river (Giordano et al., 2004). To characterize and evaluate the sediment transport in such a rapid delivery of a huge volume of river water and its effect on riverbed erosion in the lower reaches of the river, there is a clear and urgent need for monitoring the dynamic distribution of SSC with high spatial and temporal resolutions.

Remote sensing techniques have the inherent ability to provide spectral, spatial, and temporal information of surface variables and therefore are considered advantageous in measuring SSC comparing with the traditional *in situ* observation method. Various visible and near infrared (NIR) bands from satellite imagery have been proposed for estimating SSC because the reflectance of solar radiation from the water surface has been directly linked to the the amount of sediment in water (Chen et al., 2004; Dekker et al., 2002; Doxaran et al., 2002; Ritchie and Cooper, 1988). Remote sensing to monitor SSC in highly turbid inland rivers has been less successful than that for coastal, estuarine, lagoon, lake, and reservoir environments where SSC was lower (Zhou et al., 2006; Wang et al., 2011). For the limited studies on river flow, such as that for the Ganges-Brahmaputra Rivers (Islam et al., 2001), the Danube River (Onderka and Rodný, 2010), and the Yangtze River (Wang and Lu, 2010; Wang et al., 2009b), the river waters examinee were only moderately or mildly turbid waters (SSC around 1.2 g/l). For highly turbid waters, there are several difficulties in obtaining reliable results using remote sensing. Firstly, the relationships between SSC and reflectance reported in the literature are limited to SSC less than 2 g/l (Qu

et al., 2013). The annually-averaged SSC in the Yellow River from 1950 to 2007 was 26.78 g/l at Longmen (LM) and 30.36 g/l at Tongguan (TG) (Peng et al., 2010) (locations were shown in Figure 5.1). Further testing of the applicable range of the SSC-reflectance relationship is needed. Secondly, such relationships were obtained by empirical calibration of SSC against remote sensing data using linear or nonlinear regression techniques (Lathrop Jr and Lillesand, 1989; Liu et al., 2003). These models were site- and time-specific. It is not appropriate to extrapolate the empirical relationships to large rivers that usually span several satellite scenes where the flows are quite dynamic and variable. Thirdly, because inland rivers are more vulnerable to human activities, significant interactions exist among different optically active substances such as phytoplankton, dissolved organic matter, and other anthropogenic substances (Morel and Prieur, 1977).

Recently, several spectral mixture approaches have been proposed to overcome the limitations of the empirical regression equations (Sváb et al., 2005; Tyler et al., 2006; Oyama et al., 2007; Rudorff et al., 2006). The spectral mixing approach considers the mixed reflectance spectrum of a pixel covering water as a linear combination of that from three mixed components: clear water, non-phytoplankton suspended sediments, and phytoplankton. The information on the concentration of each component can be extracted effectively by a spectral mixing approach. Thus, the spectral mixing models were dependent only on the change in concentration of each component, and therefore less site- and time-specific than the regression methods. Oyama et al. (2007) showed that the spectral mixing model (spectral decomposition algorithm) could be applied to the Yellow River with reliable estimation for SSC up to 13 g/l. Similar to Oyamas spectral decomposition algorithm, we developed a spectral mixing algorithm based on a tank experiment (Qu et al., 2013), and established a robust model that

can be used in highly turbid water over large areas because the standard reflectance spectra of different sediment types could be separately identified and calibrated.

The objectives of this research were as follows: (1) to apply the spectral mixing algorithm model obtained from a tank experiment to Landsat 7 ETM+ images, (2) to investigate the possibility of using an imagery-derived standard reflectance spectra to eliminate the effect of other optical active constituents, and (3) to demonstrate the potential application of the spectral mixing algorithm model to map the SSC in the Yellow River for different seasons.

5.2 Materials and Methods

5.2.1 Study Area and Data

Two hydrological stations in the middle part of Yellow River: Tongguan (TG: 110.32604°E, 34.60448°N) and Longmen(LM: 113.68740°E, 34.90664°N) were selected for this study (Figure 5.1). The sites were representative of the highly turbid water of the Yellow River, where the river just passes through the Loess Plateau region, a land with serious soil erosion for a long time.

The daily SSC (g/l) and monthly median particle diameters at each hydrological station were obtained from the Yellow River Water Resource Commission for dates corresponding with available Landsat scenes. The measurement of SSC in the Yellow River hydrological monitoring system followed the Chinese National Standard Criteria: Code for River Suspended Sediment Measurement (Ministry of Water Resources of China, 1992) According to the Code, the SSCs at the gauging stations were averaged from samples that were collected from ten verticals at a certain cross-section of

the river and at three relative depths (sampling depth to water depth ratios) of 0.2, 0.6, and 0.8 for each vertical. Samples were analyzed by the conventional weighing method.

Landsat 7 Enhanced Thematic Mapper Plus (ETM+) scenes were chosen for this study. The Landsat 7 imagery has the longest time series and finest spatial resolution among currently publicly accessible satellites data and is available from the Global Land Cover Facility repository. All Landsat ETM+ scenes with cloud cover less than 3% were collected for the study area. A total of 105 images were collected, in which, 59 scenes were for LM (Path 035, Row 126), and 46 were for TG (Path 036, Row 126).

A series of subset imagery around each gauging station were extracted from the Landsat scenes. Digital Numbers (DNs) in a L1G product of Landsat 7 data was then converted to the top of the atmospheric (TOA) reflectance according to the Landsat 7 user book (Administration et al., 1979).Then, the sample pixels around the station were taken from the atmospheric corrected subset imagery as the band combination was set as Band 7 in blue, Band 5 in green, and Band 3 in red (Figure 5.3) to distinguish water from land.

The TOA reflectance was the sum of contributions from several components such as atmospheric attenuation, surface sun-glint, and other surface and subsurface reflections. For a study on the constituents in a water column, atmospheric correction is necessary in converting TOA reflectance to water reflectance. However, such corrections are quite difficult with simulation of radiative transfer processes involved, especially when *in situ* atmospheric conditions are unavailable. The Dark Object Subtraction (DOS) method had been widely used because it required no *in situ* field measurement during the satellite over-flight. For this study, we applied the atmo-

spheric correction of Wang et al. (2009b), developed for a SSC study on the Yangtze River, China. Based on the procedure, the water reflectance from Landsat ETM+ image was estimated by subtracting reflectance in Band 1 to Band 4 from reflectance in Band 7 (2080 nm to 2350 nm), in which water is indeed very close to "dark" due to very high absorption. Hence, it was assumed that whatever reflectance remains in Band 7 was entirely attributed to surface specular reflectance and aerosol path reflectance.

5.2.2 Spectral Mixing Algorithm

Conceptually, the spectral radiance/reflectance of a volume of turbid water can be considered a weighted sum of that of the primary components such as clear water, non-phytoplankton suspended sediments (NPSS), and phytoplankton (Goodin et al., 1993), which can be expressed as:

$$Rr(\lambda) = \sum_{i=1}^{n} SMI_i P_i(\lambda) \tag{5.1}$$

where $Rr(\lambda)$ is the wavelength-specific reflectance, $P_i(\lambda)$ is the standard wavelength-specific reflectance for component i, representing the characteristic spectral pattern or signature of the component, n is the number of the primary components, and SMI_i is the spectral mixing index for the i^{th} component and indicates the portion of its contribution to the total reflectance.

The development of the spectral mixing algorithm in our study involved two key steps. The first was to translate the reflectance in each band to a spectral mixing index (SMI) based on the assumption that the mixed reflectance spectrum of a given pixel

is a linear combination of that of the primary components in water. The second step was to apply the obtained SMI of sediment to the SSC estimation model, in which the single band reflectance, band ratio, and arithmetic operations of bands were obtained in the same manner as in conventional methods. In our tank experiment, the samples were made of distilled water and sediment. For that, the reflectance mixing equation is:

$$Rr(\lambda) = SMI_w P_w(\lambda) + SMI_s P_s(\lambda) \tag{5.2}$$

where SMI_w and SMI_s are spectral mixing indices of water and sediments, respectively, direct measures of their masses or concentrations, and $P_w(\lambda)$ and $P_s(\lambda)$ represent the distinctive spectral pattern or signature of clean water and sediment, respectively.

Using the Landsat data, the spectral mixing index of sediment (SMI_s) could be estimated by solving the following equation using a least squares method:

$$Rr(Bi) = SMI_w P_w(Bi) + SMI_s P_s(Bi) \tag{5.3}$$

where Bi denotes the i^{th} Landsat band. The choices for standard reflectance spectra of water and sediment are important in this procedure. We first conducted spectral measurement for clean water and dried sediment in laboratory conditions. Then it was assumed that the sediment is the dominate constitutein the central reach of the Yellow River and the sediment concentrations in the adjacent lakes was relatively low. Accordingly, we chose the lake water in the same Landsat scene to represent background water. Figure 5.2 showed the standard reflectance spectra of sediment and the "clean" water.

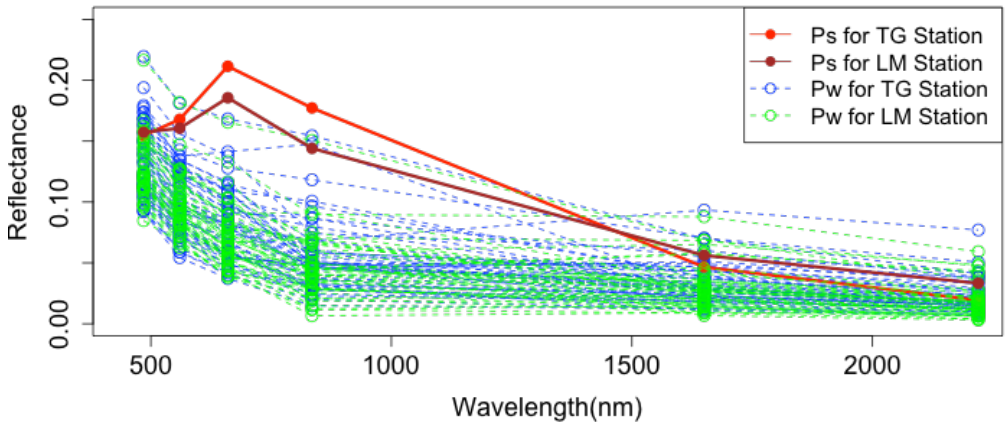

Figure 5.2: Image derived standard reflectance spectra (SRS) of clean water and laboratory measured SRS of dry sediments using the system shown in Figure 3.1, $P_w(\lambda)$ and $P_s(\lambda)$ are the distinctive spectral pattern or signature of clean water and sediment, respectively.

The relationship between SSC and reflectance was determined in our previous experiment with a physically-based exponential model ($R^2 > 0.9$, $F > 20$):

$$Rr(\lambda) = C_1(\lambda)(1 - e^{-\frac{SSC}{C_0(\lambda)}}) \tag{5.4}$$

where $C_1(\lambda)$ is the saturated reflectance, to which the reflectance approaches as SSC increases. $C_0(\lambda)$ represents the velocity to approach the saturation level. In other words, it indicates the upper limit of predictable SSC. In the laboratory, the upper limit (predictable) SSC for sediments from two locations on the Yellow River were 15 and 20 g/l. Here, we consider the reflectance curve of 30 g/l as the standard reflectance spectra of sediment.

$$P_s(\lambda) = C_1(\lambda)(1 - e^{-\frac{30}{C_0(\lambda)}}) \tag{5.5}$$

In the second step, we applied the obtained SMIs in the first step for estimating SSC by:

$$ln(SSC) = a + bSMI_s \tag{5.6}$$

where a and b are regression coefficients.

5.2.3 SSC spatial distribution

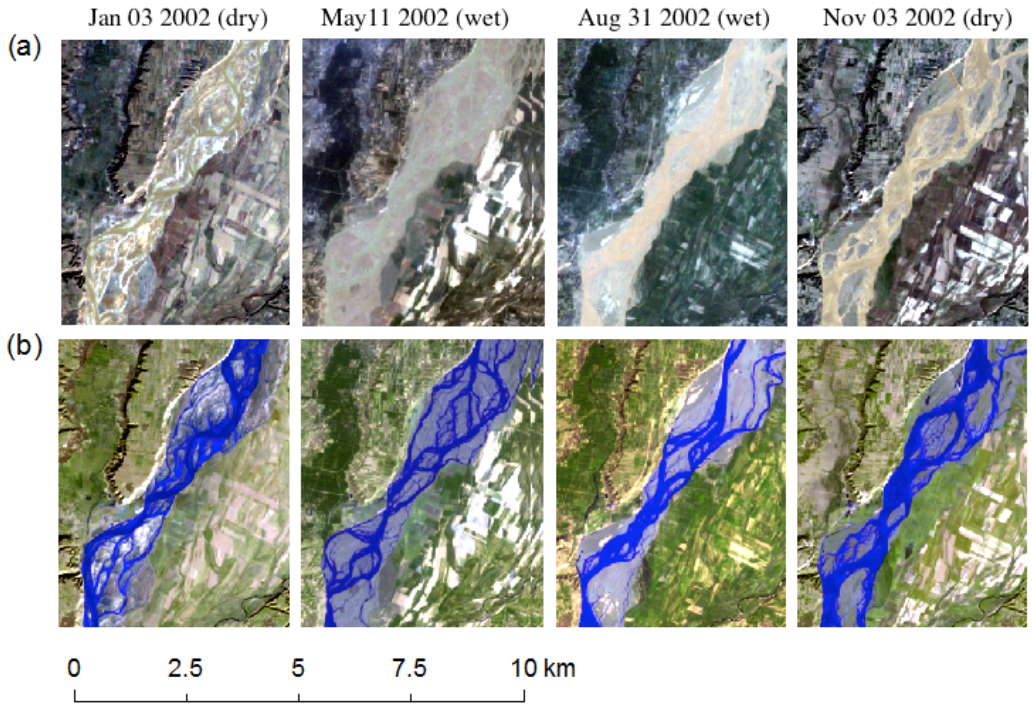

Figure 5.3: The representative Landsat 7 ETM+ image of river section for mapping of SSC distribution. (a) band combinations: Band 4 in red, Band 3 in green, and Band 2 in blue, (b) band combination: Band 7 in red, Band 5 in green, and Band 3 in blue

In order to demonstrate the advantages of the remote sensing method in providing spatial SSC information, a site located in the overlap area of the two Landsat scenes (1: LM Station, Path 126 Row 035; 2: TG Station, Path 126 Row 036) was chosen

to show the dynamic (seasonal) distribution of SSC along the stream. Four images on January 3, May 11, August 31, and November 3, 2002, covering both wet season (May through October) and dry season (November through April), were used to map the SSC distribution. For each image, we first used ERDAS Objective to extract the water bodies of the river, and then used the spectral mixing algorithm to estimate SSC for each pixel of the water bodies. ArcGIS was employed to map the SSC distribution by converting the SSC calculation to a raster file. Figure 5.3 shows the imagery for four selected dates by combining Band 3 in red, Band 2 in Green, and Band 1 in Blue to show the natural color and by combining Band 7 in red, Band 5 in Green, and Band 3 in Blue to highlight the water. The SSC values in upstream LM were 5.07 g/l, 0.91 g/l, 16.90 g/l, and 1.90 g/l for January 3, May 11, August 31, and November 3 2002, respectively. The corresponding SSC values in the downstream TG were 6.68 g/l, 4.90 g/l, 17.70 g/l, and 8.81 g/l, respectively.

5.3 Results

5.3.1 Spectral Reflectance of Water Samples

Values for SSC and reflectance of the waters in the Yellow River were plotted in Figure 5.4 and Figure 5.5 for each of the two stations. The reflectances for back ground water were also shown on the figures for reference. There seems to be no correlation between SSC and water reflectance in Band 1 (r=-0.015 for LM data, r=-0.161 for TG data). For Band 2 to Band 5, water reflectance increases with increasing SSC and tends to be constant or even decrease for SSC above 10 g/l. Compared to other bands, Band 3 and Band 4 produced the highest correlation for TG and LM data (for LM

data $r = 0.538$ at Band 3 and $r = 0.624$ at Band 4; for TG data $r = 0.589$ at Band 3 and $r = 0.397$ at Band 4), respectively. The result for LM data was consistent with the study on Yangtze River (Wang et al., 2009b) in which the water reflectance in Band 4 showed a significant power relation with SSC ($R^2 = 0.88, n = 24$). In Band 5 and Band 7, reflectance from the water in the Yellow River and the background water overlapped (in the two bottom sub-figures of Figure 5.4 and Figure 5.5) because of the high absorption of water in NIR range (760 nm to 900 nm) dominate the spectral pattern of reflectance. In Band 7, the reflectance was mainly attribution to water surface specular reflection.

The scatter plots between SSC and DOS-corrected water reflectance from Band 1 to Band 4 were shown in Figure 5.6. The DOS-corrected reflectance and SSC showed a consistent changing pattern with that of the TOA reflectance. There was no obvious improvement produced from the DOC-corrected reflectance.

5.3.2 The Spectral Mixing Algorithm

The spectral mixing index of sediments SMI_s were calculated from reflectance (both TOA reflectance and DOS-corrected water reflectance) and standard reflectance spectra of sediment and clean water for Band 1 to Band 4 using Eq (5.3). SSC and reflectance values was tested for normality by using the Shapiro-Wilk statistic. R software was used for statistical analysis (R Core Team, 2013). The Shapiro-Wilk test indicated that reflectance and SSC values did not follow normal distributions SSC was log (natural) transformed to develop the relation with SMIs Eq. (5.3). Figure 5.7 shows the regression results between the logarithm transformed SSCs and SMI_s (Eq. 5.6) for station LM and TG. Figure 5.7 (a) shows the SMI_s from the

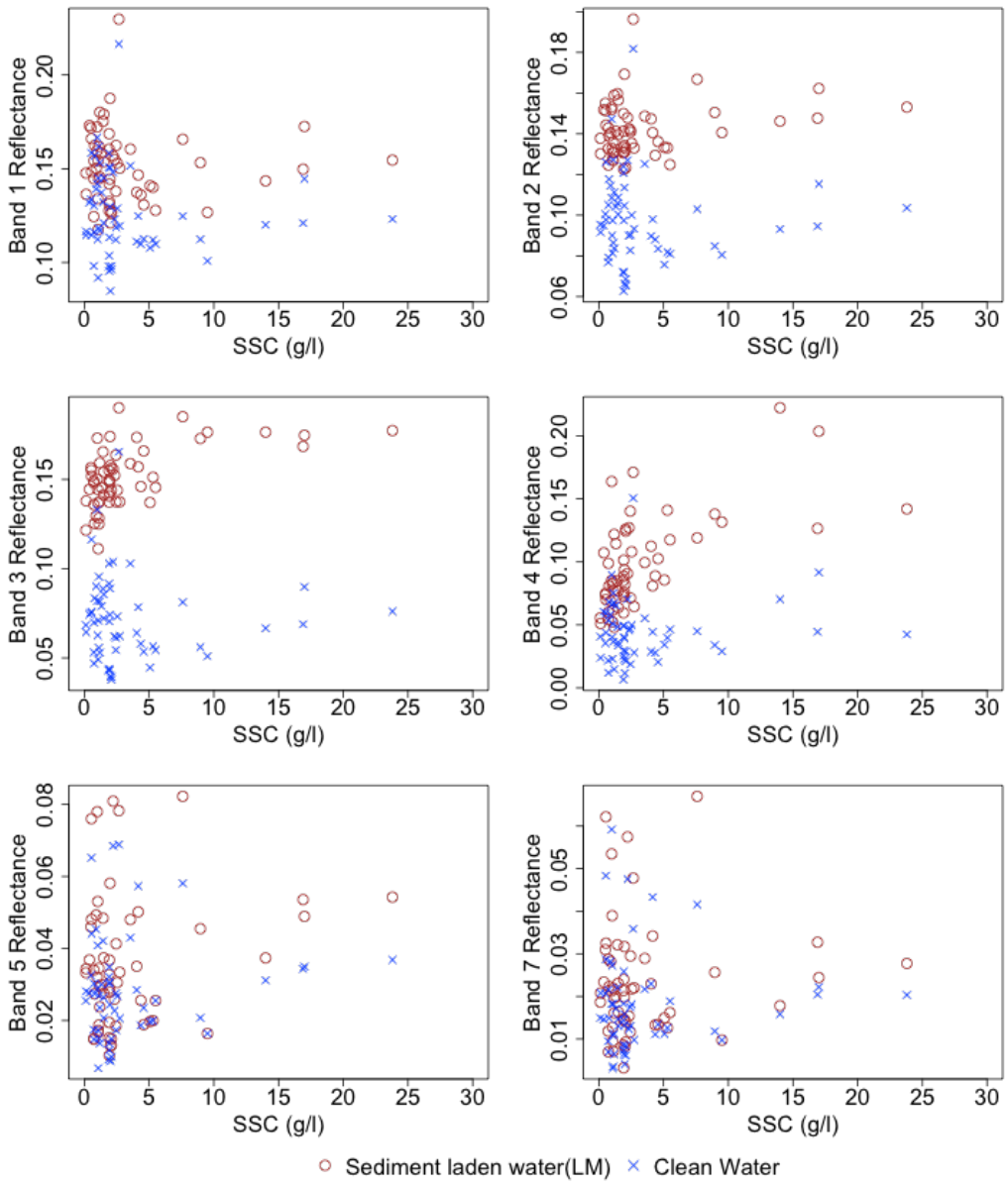

Figure 5.4: The TOA reflectance and corresponding SSC observed at the Longmen (LM) station of the Yellow River

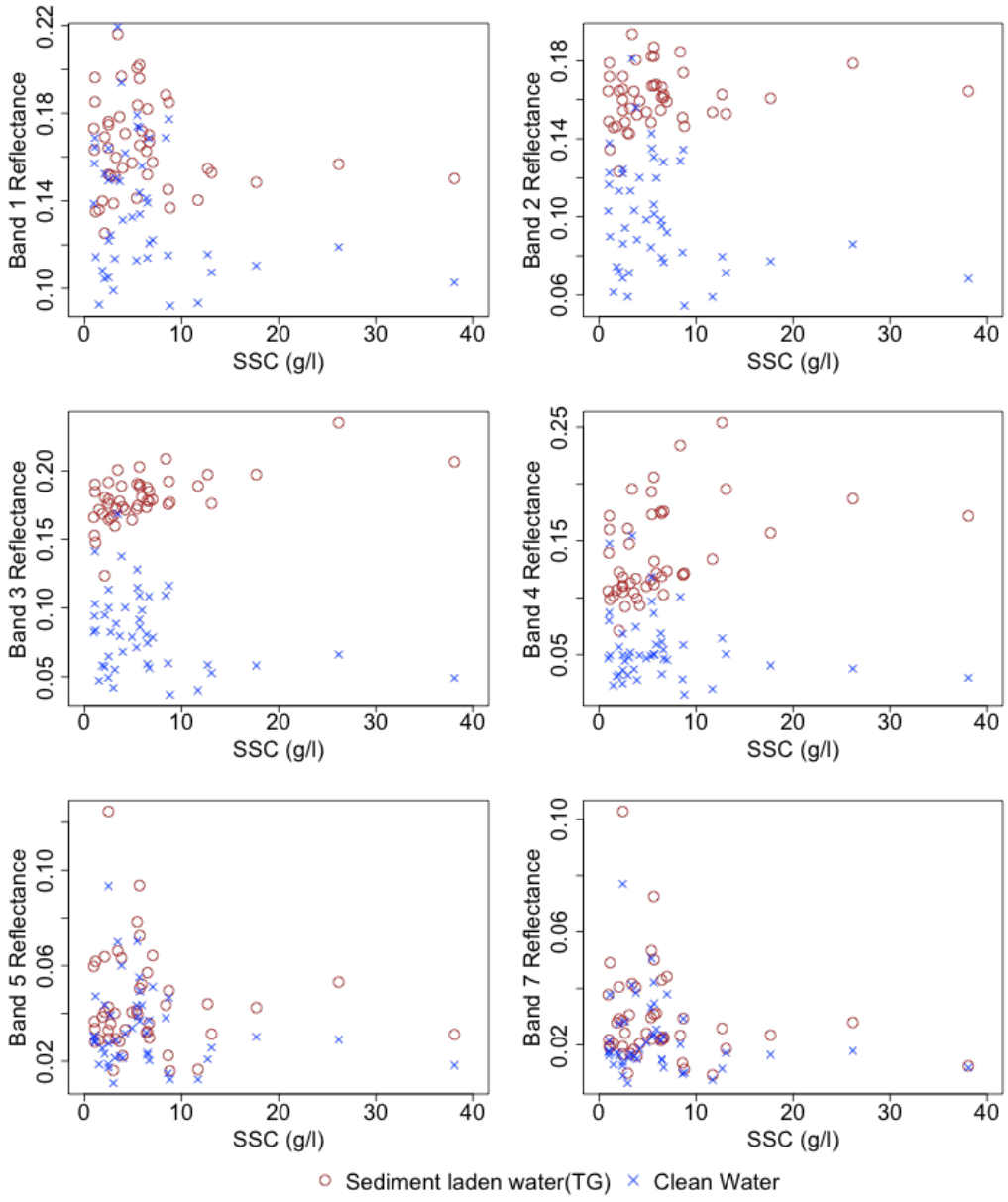

Figure 5.5: The TOA reflectance and corresponding SSC observed at the Tongguan (TG) station of the Yellow River

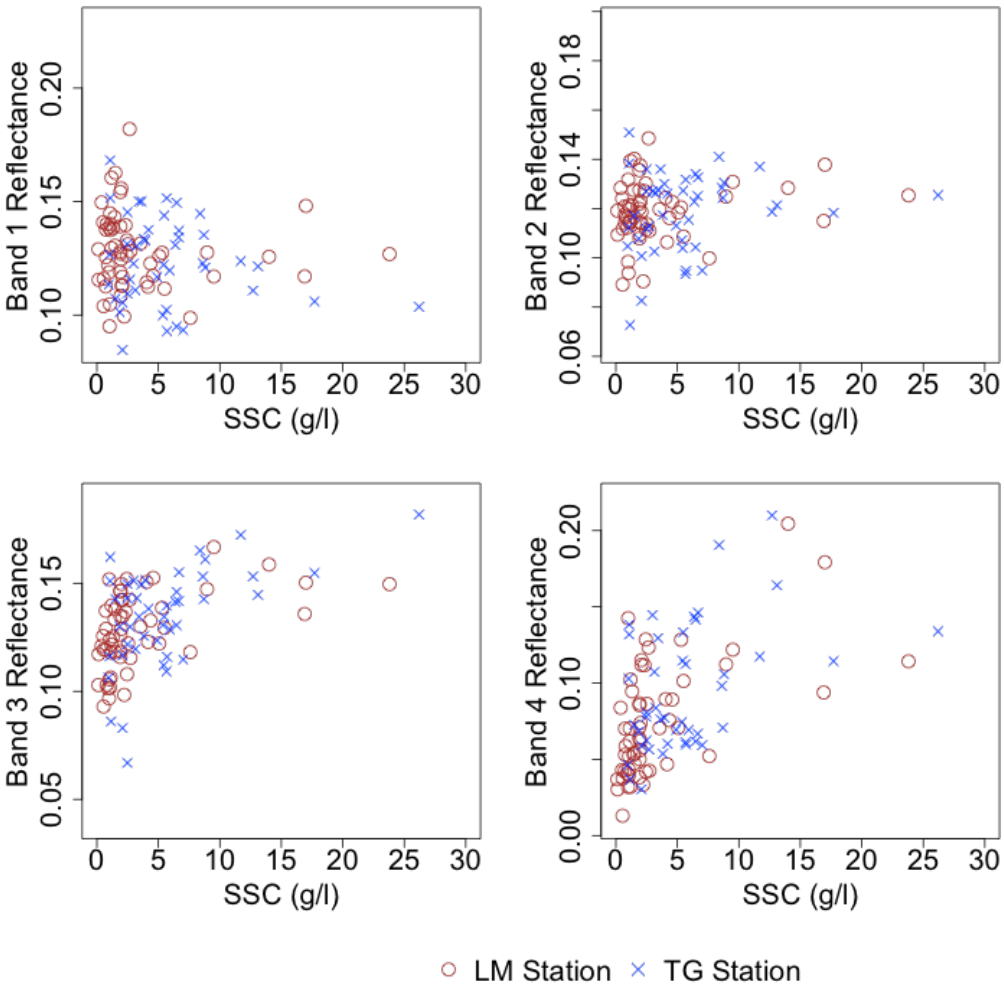

Figure 5.6: The DOS corrected water reflectance and corresponding SSC from Band 1 to Band 4

TOA reflectance and Figure 5.7 (b) shows the SMI_s from DOS-corrected water reflectance. Outlier analysis were performed by using the outliers package (Komsta, 2011) in R software (R Core Team, 2013). According to the test, three observations at the LM station (circled in Figure 5.7) hadresiduals from model fitting beyond the 99% probability. These points were excluded from further analysis in our study.

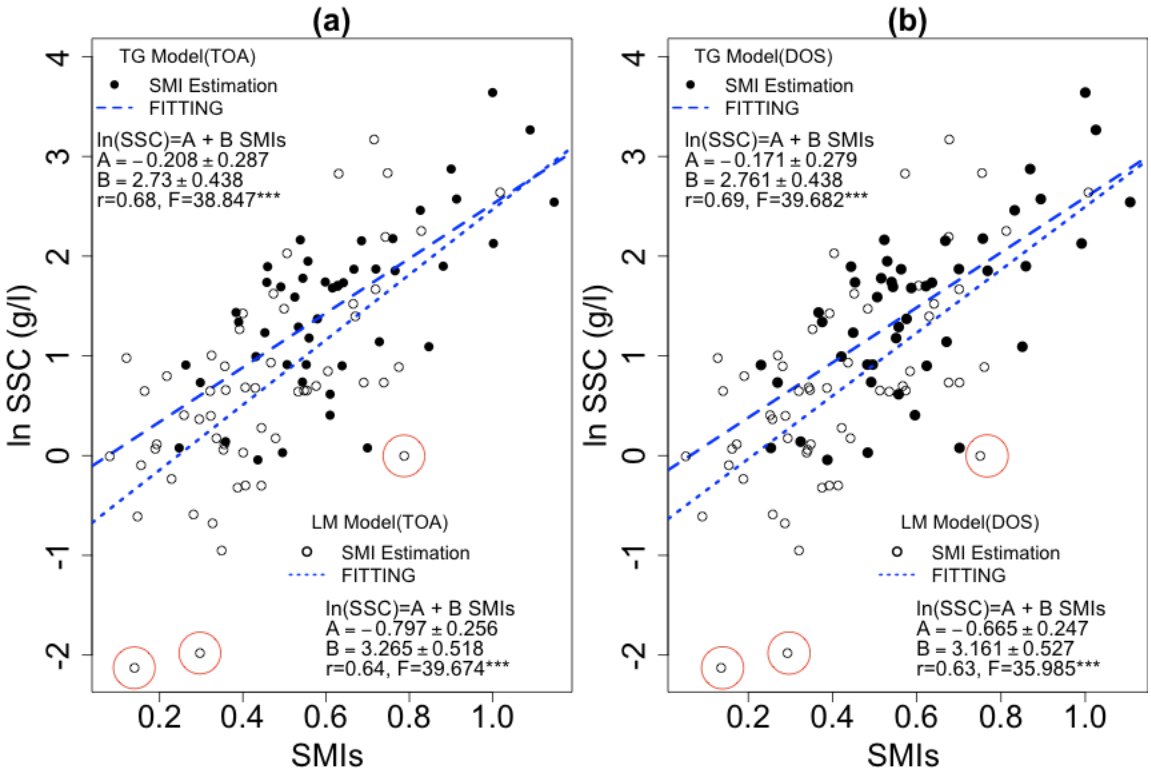

Figure 5.7: The relationship between logarithm transformed SSC and the spectral mixing index of sediment (SMI_s): (a) the SMI_s derived from TOA reflectance, (b) the SMI_s derived from the DOS-corrected reflectance.

The Dark Object Subtraction (DOS) method corrects only the additive scattering effect and not for the multiplicative transmittance effect (Mahiny and Turner, 2007), so its accuracy is limited. But, it is still widely used because of its simplicity and lack of a need of *in situ* calibration. In remote sensing studies of SSC in Yangtze

River, it was an effective approach for a reliable model ($R^2 = 0.88, n = 24$) (Wang et al., 2009b; Wang and Lu, 2010). The use of background lake water in the same satellite scenes as the standard reflectance spectrum of water had eliminated some affect from atmospheric variation. Therefore, the difference of the SSC and SMI_s correlation between using TOA reflectance or using DOS-corrected reflectance was not remarkable in our study. However, the DOS corrected reflectance make model for different stations showed more consistency with the regression parameters were closer (the parameter B in Eq (5.3) was 3.16 v.s. 2.76 for TG and LM TOA data, and 2.73 v.s. 3.26 for TG and LM DOS data).

Since little difference existed between LM and TG model, a LMTG model was constructed by combining the data for the LM and TG stations (Figure 5.8). The LMTG model was significant ($F = 117.07$, $P < 0.05$) as was the correlation coefficient ($r = 0.71$).

5.3.3 SSC Spatial Distribution

To demonstrate how the spectral mixing method would behave when applied to the entire river, we mapped the SSC for the overlap area of two adjacent images that covers the LM and TG stations. Figure 5.9 showed the histograms of estimated SSC in the studied water surface for the 4 bands of the LM image and the TG image, and joint 4 bands of the LM image and the TG image. Because the area for the Yellow River map was located between the LM and TG stations, the mean SSC in the study region (6.28 g/l, 1.38 g/l, 7.05 g/l, and 4.67 g/l) was calculated from the SSC observed at the LM station (5.07 g/l, 0.91 g/l, 16.90 g/l, and 1.90 g/l) and the TG station (6.68 g/l, 4.90 g/l, 17.7 g/l, and 8.81 g/l) for the Jan 03, May 11, Aug 31,

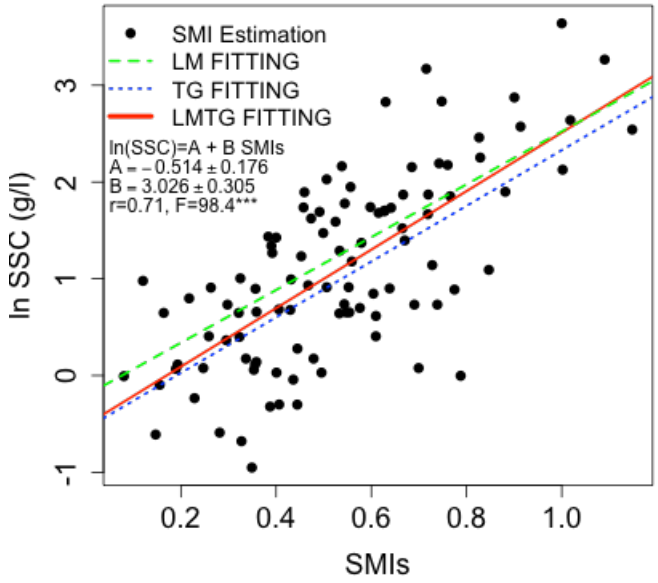

Figure 5.8: Regression model of SSC and SMI_s based on the joint TOA reflectance and SSC observations at the LM and TG stations of the Yellow River

and Nov 02 2002, respectively. But exception showed on Aug 31 that was 7.05 g/l in the study area while it was 16.90 g/l and 17.7 g/l in LM and TG, respectively. The estimated SSC from each LM and TG image and from the combined images showed similar distributions (Figure 5.9). For the SSC on Jan 03 and Aug 31, both the shape and magnitude of the distribution were similar. The SSC distribution on May 11 showed obvious differences between the two station images. The SSC estimated from the combined images was between the LM image estimates and the TG image estimates. The shape of the histograms from the combined images estimates were consistent with the histograms from the TG model. However, the the difference in the distributions were obvious from the dry season to wet season, that was further illustrated in Figure 5.10. In the dry season on Jan 03 and Nov 03, 2002, the water

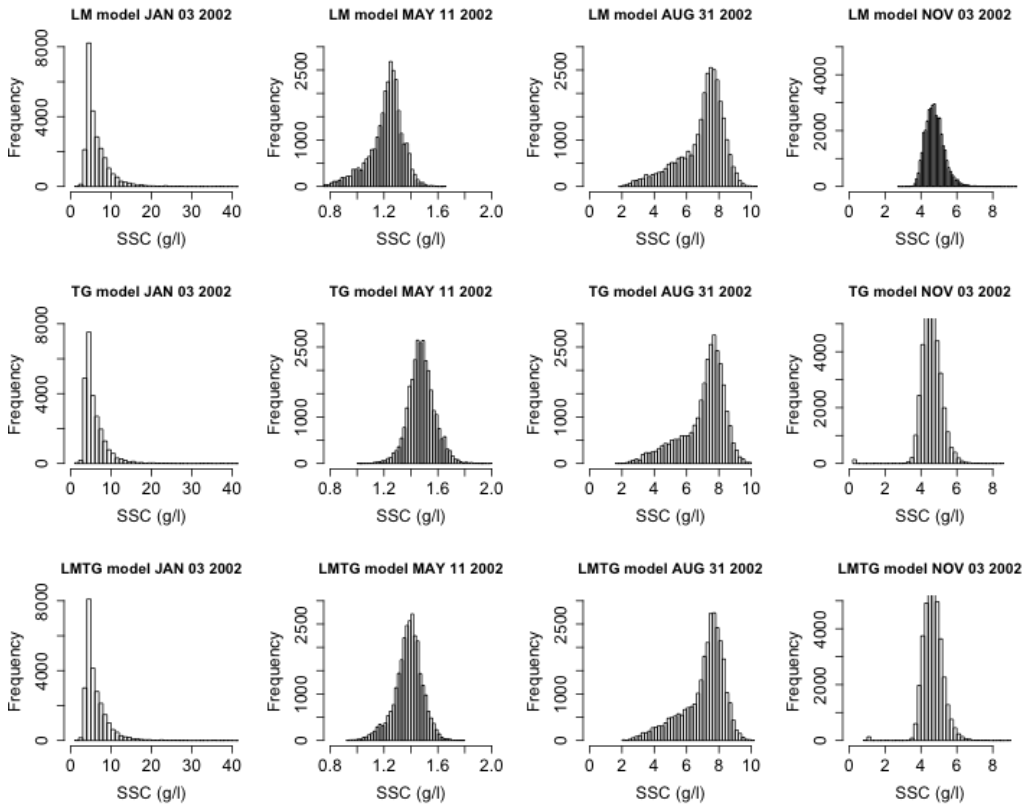

Figure 5.9: Histograms of SSC estimation using the LM model, TG model, and jointed LMTG model

in the center of the stream was relatively clean and high SSC was observed along the riverbank and in the narrow channels of the river. While in the wet season on May 11 and Aug 31, the situation almost reverses with high SSC in the center of the river and low SSC along the riverbank. This result indicates that the inflow from the upstream was high in sediment load caused by heavier soil erosion in up-bound watershed. In the dry season, the inflow water was relatively clean. As a seasonal river, the extent of the Yellow River changed dramatically between seasons.

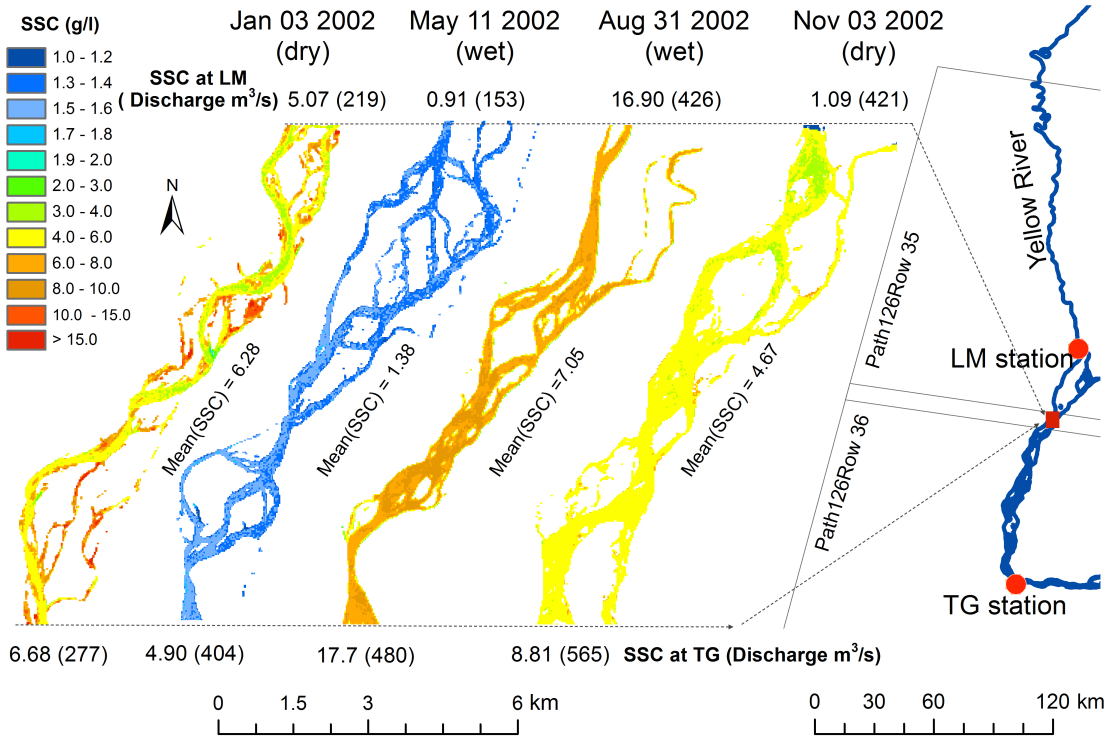

Figure 5.10: The SSC map for the sites located between LM and TG stations on the Yellow River

5.4 Discussion

How accurately SSC can be quantified by means of remote sensing relies on how optically active the parameter is and whether other parameters, if present, affect its spectral reflectance (Liu et al., 2003). In case of co-existence of several constituents, not all of them contribute to the recorded reflectance equally (Bowers et al., 1998). This study proposed a spectral mixing algorithm to estimate SSC from water reflectance. The spectral mixing method considers the mixed reflectance spectrum of a given pixel as a linear combination of contribution from each primary component. For each of the primary components, the standard wavelength-specific reflectance, referred to as standard reflectance spectra [P_w, P_s in Eq. (5.3)], represents the distinctive spectral pattern or signature of each component. The spectral mixing index [SMI_w, SMI_s in Eq. (5.3)] that is directly related to their masses or concentrations was used to construct the model. There are two essential considerations for this method: selection of primary components, and measurement of standard reflectance spectra for primary components.

5.4.1 Primary Components in the Yellow River Water

Water quality parameters that can be quantified by means of remote sensing fall into three groups: inorganic sediment particulates, phytoplankton pigments, and CDOM (Doerffer et al., 1999). Including water, there are four optically active substances. The complex interactions of four optically active substances result in difficulties for remote sensing of water quality in coastal and inland waters (Doxaran et al., 2002; Gin et al., 2002, 2003; Han, 1997; Lodhi et al., 1997b; Novo et al., 1989b). Thus, the ideal option for spectral mixing method is to consider all four primary components for

coastal and inland water. However, it is always difficult to get spectral information for all substances. Meanwhile, the contributions of individual primary components to the final spectral characteristic for a mixed water body also depend on their relative concentrations. In our study, we simply choose only water and sediment in the spectral mixing method. In fact, it is always necessary to select some from the domain of substances for the spectral mixing based method. For example, three primary components (clean water, non-phytoplankton suspended sediments , and phytoplankton) were used in a spectral decomposition algorithm to estimate the chlorophyll-α in Lake Kasumigaura, and the results are better than a conventional regression model (Oyama et al., 2007, 2009, 2010). They concluded that the influence of CDOM on the reflectance spectrum could be ignored in the case of Lake Kasumigaura (DOC: $3.2 mg/l$) according to the comparison of the reflectance spectrum between pure water and water samples from the lake.

DOC along the Yellow River mainstream is much lower than that in other world rivers (Ludwig et al., 1996) due to the low rainfall (Yang et al., 2004), low vegetation coverage (Wang et al., 2001), low organic matter content in the loess soils (Zhang et al., 2013) and the high absorption of DOC by high sediment load (Moreira-Turcq et al., 2003). According to Zhang et al. (2013), the DOC in the Yellow River varies from 1.6 mg/l to 3.8 mg/l. Because these values are not higher than the value for Lake Kasumigaura (Oyama et al., 2007), it is reasonable to ignore the effect of CDOM for the sediment estimation in the Yellow River. Beside sediment, phytoplankton is another major in-water constituents (Liu et al., 2003). Phytoplankton pigments consist mainly of chlorophyll a, b and c, of which chlorophyll a is derivable by means of remote sensing. Figure 5.2 showed the spectral curve of clean water from different images. Because the reflectance was retrieved from the locations where the water is

assumed to be clean with low sediment concentration year around, the variation of the curve was possibly due to changes of Chlorophyll α concentration and variation. This is consistent with the testing of the spectral decomposition algorithm (SDA) for different phytoplankton species by Oyama et al. (2010).

Lack of the consideration of phytoplankton will surely effect the accuracy of the method, but the ignore at the startup study about spectral mixing method in highly turbid river is acceptable for a reasonable estimation. Chlorophyll a concentration is only sensitive in narrow bands of imagery (Harrington and Repic, 1995). The spectral mixing method derives the mixing index from all available VIS and NIR bands ($450nm$-$900nm$), so effect of phytoplankton is relatively small. Meanwhile, we derive end-members of clean water from images to reduce the effect of chlorophyll a concentration and its variations within a water body.

For a more accurate estimation of the spectral characteristics of phytoplankton in the Yellow River is the interaction between SSC and phytoplankton should be thoroughly investigated in both laboratory spectral experiments and field survey-based studies. In practice, users can also set the primary components according to the conditions of their own study area when the spectral mixing method is used.

5.4.2 Measurement of standard reflectance spectra for Primary Components

The selection of standard reflectance spectra (P_s and P_w in Eq. 5.3) of a water body is important in the application of spectral mixing based methods. Generally, there are two alternative approaches for selecting standard reflectance spectra (refer to end-members in some studies) (Wu and Murray 2003): one is to use reference end-

members from laboratory (Oyama et al., 2007, 2009) or field-based measurements of the standard reflectance spectra, or a simulation from bio-optical models (Oyama et al., 2009); the other is to use image-derived standard reflectance spectra.

In this study, the the standard reflectance spectra for sediment were derived using the first approach by adopting the measurement from the laboratory because it is accurate and atmospheric effects could be ignored. However, we used the spectral measurement of high sediment concentration in water instead of measurement of dry sediment, which is commonly used to represent the standard reflectance spectra of sediment. In our previous study, we found that the standard reflectance spectra of high sediment-laden water (about 10 g/l) could obtain the better performance for highly turbid water (The $SSC > 2$ g/l).

We derived the standard reflectance spectra for water from the corresponding images. The spectral behavior of water parameters varies with the type of constituent (Liu et al., 2003). In Figure 5.2, it could be noticed that the reflectance of water from 400 nm to 700 nm (Landsat Band 1 to Band 3) is relatively high. It indicated there were other optical active constituents in water other than sediment. This could explain why the correlation between SSC and reflectance was weak in Band 1 and Band 2, with the reflectance relatively high in low sediment concentration that could be seen in Figure 5.4 and Figure 5.5 and in the relative study in the Yangtze River by Wang and Lu (2010); Wang et al. (2009b). Comparing the reflectance of clean water in Figure 5.4 and Figure 5.5, the high value of reflectance was consistent with that for sediment-laden water but was more obvious, which indicates the abnormal high reflectance of sediment laden water are due to the contribution of clean water. The spectral mixing method using image-derived standard reflectance spectra of clean water is promising to estimate the SSC with the effects from other optical active

constituents in water being eliminated. The correlation between SSC and spectral mixing method was improved compare to the correlation between SSC and single bands or reported band combinations or ratio (Max $r = 0.62$ between reflectance in Band 3 and SSC).

5.4.3 Potential Application

Compared to traditional field SSC measurements, this remote sensing approach can help map SSC across and along a river. For example, Figure 5.10 showed SSC variations along the Yellow River and the sediment over seasonal hydrological variations by using multi-temporal satellite images. Such SSC maps over a certain period of time may provide important information on sediment sources, effects of reservoir trapping, and channel erosion/deposition. In addition, remote sensing, jointly with rating curves which represents the regression relation between SSC and water discharge (Horowitz, 2003), can assist in building sediment budgets. Wang and Lu (2010) discussed the procedure for further application in this context.

There are two advantages of this method: (1) this method should be less site- and time-specific because the independent variable used in the spectral mixing model almost significantly varies with SSC concentrations and is less affected by the other constituents. Therefore, a model can be constructed in advance using a controlled experiment in the laboratory or a simulation can be achieved in advance by using a radiative transfer model of natural waters [Hydrolight ((Mobley and Mobley, 1994))]; (2) it is convenient to combine the bands information from different bands even from different satellites. In our study, we use combined band information from two scenes to estimate SSC. The histograms of sediment distribution estimated by the scene covers

LM (Path 126 Row 035) (LM model) and scenes covers TG (Path 126 Row 036) (TG Model) and both of them (LMTG Model) in Figure 5.9. Usually, the different model should be constructed when the different satellite images are used.

5.5 Conclusions

This paper presented a methodology to estimate water quality in a turbid river from Landsat ETM+ data, based on the spectral mixing algorithm. The key to successfully applying the spectral mixing based estimation model to satellite data is to select the end-member and an appropriate satellite-SRS for each end-member. Our study indicates that the use of natural clean water as the reference can improve the simulation by eliminating the effect by other optical active components in the water. In future work, some improvements will be crucial such as (1) the development of an accurate bio-optical model for satellite-SRS simulation or consideration of a nonlinear combination of end- members in a spectral mixture modeling approach for a water body. (2) This study ignored some factors such as particle size, shape, color, and mineral type (Gin et al., 2003; Warrick et al., 2004), as well as organic substances and chlorophyll (Han, 1997; Gin et al., 2003) that can affect the optical characteristics of turbid waters. In future studies, these factors should be considered to further improve the adaptive of the model. (3) In addition, the applicability of SMA to other cases (e.g. other satellite images, other waters) must also be tested. (4) Field investigations should be conducted to validate the estimation of SSC distribution along the river.

Bibliography

James G Acker, Alexander Vasilkov, Denis Nadeau, and Norman Kuring. Use of SeaWiFS ocean color data to estimate neritic sediment mass transport from carbonate platforms for two hurricane-forced events. *Coral Reefs*, 23(1):39–47, April 2004.

United States National Aeronautics Administration, Space, Goddard Space Flight Center, and EROS Data Center. Landsat data users handbook, 1979.

R Asadpour, L H San, M M Alashloo, and S Y M Alashloo. A statistical model for mapping spatial distribution of total suspended solid from THEOS satellite imagery over Penang Island, Malaysia. *Journal of Applied Sciences Research*, 8(1): 271–276, 2012.

K Avinash, B Jena, M S Vinaya, K S Jayappa, A C Narayana, and H Gangadhara Bhat. Regionally tuned algorithm to study the seasonal variation of suspended sediment concentration using IRS-P4 Ocean Colour Monitor data. *Egyptian Journal of Remote Sensing and Space Science*, 15(1):67–81, 2012.

E T Baker and J W Lavelle. The effect of particle size on the light attenuation

coefficient of natural suspensions. *Journal of Geophysical research*, 89(C5):8197–8203, 1984.

D S Bhargava and D W Mariam. Spectral reflectance relationships to turbidity generated by different clay materials. *Photogrammetric engineering and remote sensing*, 36(9):225–229, 1990.

D S Bhargava and D W Mariam. Light penetration depth, turbidity and reflectance related relationship and models. *ISPRS Journal of Photogrammetry and Remote Sensing*, 46(4):217–230, 1991.

C E Binding, D G Bowers, and E G Mitchelson-Jacob. Estimating suspended sediment concentrations from ocean colour measurements in moderately turbid waters; The impact of variable particle scattering properties. *Remote Sensing of Environment*, 94(3):373–383, 2005.

D G Bowers and C E Binding. The optical properties of mineral suspended particles: A review and synthesis. *Estuarine, Coastal and Shelf Science*, 67(1-2):219–230, March 2006.

D G Bowers, S Boudjelas, and G E L Harker. The distribution of fine suspended sediments in the surface waters of the Irish Sea and its relation to tidal stirring. *International Journal of Remote Sensing*, 19(14):2789–2805, November 1998.

D E Bowker and W G Witte. Evaluation of ERTS MSS digital data for monitoring water in the lower Chesapeake Bay area. *Remote sensing of earth resources.*, 4: 591–600, 1975.

H Buiteveld, JHM Hakvoort, and M Donze. Optical properties of pure water. In *Ocean Optics XII*, pages 174–183. International Society for Optics and Photonics, 1994.

R P Bukata, J H Jerome, A S Kondratyev, and D V Pozdnyakov. *Optical properties and remote sensing of inland and coastal waters*. CRC, 1995.

K L Carder, P Reinersman, R F Chen, F Muller-Karger, C O Davis, and M Hamilton. AVIRIS calibration and application in coastal oceanic environments. *Remote Sensing of Environment*, 44(2):205–216, 1993.

K L Carder, F R Chen, Z P Lee, S K Hawes, and D Kamykowski. Semianalytic Moderate-Resolution Imaging Spectrometer algorithms for chlorophyll a and absorption with bio-optical domains based on nitrate-depletion temperatures. *Journal of Geophysical Research-Oceans*, 104(C3):5403, 1999.

J Chen and W Quan. An improved algorithm for retrieving chlorophyll-a from the Yellow River Estuary using MODIS imagery. *Environmental monitoring and assessment*, pages 1–13, 2012.

S Chen, W Huang, W Chen, and X Chen. An enhanced MODIS remote sensing model for detecting rainfall effects on sediment plume in the coastal waters of Apalachicola Bay. *Marine environmental research*, 72(5):265–272, 2011a.

S Chen, W Huang, W Chen, and H Wang. Remote sensing analysis of rainstorm effects on sediment concentrations in Apalachicola Bay, USA. *Ecological Informatics*, 6 (2):147–155, 2011b.

X Chen, Y S Li, Z Liu, K Yin, Z Li, O W H Wai, and B King. Integration of multi-source data for water quality classification in the Pearl River estuary and its adjacent coastal waters of Hong Kong. *Continental Shelf Research*, 24(16): 1827–1843, 2004.

Z Chen, P J Curran, and J D Hansom. Derivative reflectance spectroscopy to estimate suspended sediment concentration. *Remote Sensing of Environment*, 40(1):67–77, 1992.

Zhimin Chen, Jim D Hanson, and Paul J Curran. The form of the relationship between suspended sediment concentration and spectral reflectance: its implications for the use of Daedalus 1268 data. *International Journal of Remote Sensing*, 12(1):215–222, 1991.

V K Choubey. The effect of properties of sediment type on the relationship between suspended sediment concentration and radiance. *Hydrological Sciences Journal/Journal des Sciences Hydrologiques*, 39(5):459–470, 1994.

Vena W Chu, Laurence C Smith, Asa K Rennermalm, Richard R Forster, Jason E Box, and Niels Reehy. Sediment plume response to surface melting and supraglacial lake drainages on the Greenland ice sheet. *Journal of Glaciology*, 55(194):1072–1082, 2009.

P J Curran and EMM Novo. The relationship between suspended sediment concentration and remotely sensed spectral radiance: a review. *Journal of Coastal Research*, 4(3):351–368, 1988.

P J Curran, J D Hansom, S E Plummer, and M I Pedley. Multispectral remote

sensing of nearshore suspended sediments: a pilot study. *International Journal of Remote Sensing*, 8(1):103–112, 1987.

A G Dekker, H J Hoogenboom, L M Goddijn, and T J M Malthus. The relation between inherent optical properties and reflectance spectra in turbid inland waters. *Remote Sensing Reviews*, 15(1-4):59–74, February 1997.

A G Dekker, R J Vos, and S W M Peters. Comparison of remote sensing data, model results and in situ data for total suspended matter (TSM) in the southern Frisian lakes. *Science of The Total Environment*, 268(1-3):197–214, 2001.

A G Dekker, R J Vos, and S W M Peters. Analytical algorithms for lake water TSM estimation for retrospective analyses of TM and SPOT sensor data. *International Journal of Remote Sensing*, 23(1):15–35, January 2002.

R Doerffer and J Fischer. Concentrations of chlorophyll, suspended matter, and gelbstoff in case II waters derived from satellite coastal zone color scanner data with inverse modeling methods. *Journal of Geophysical research*, 99(C4):7457–7466, 1994.

R Doerffer, K Sorensen, and J Aiken. MERIS potential for coastal zone applications. *International Journal of Remote Sensing*, 20(9):1809–1818, 1999.

D Doxaran, J M Froidefond, S Lavender, and P Castaing. Spectral signature of highly turbid waters: Application with SPOT data to quantify suspended particulate matter concentrations. *Remote Sensing of Environment*, 81(1):149–161, 2002.

D Doxaran, J M Froidefond, P Castaing, and M Babin. Dynamics of the turbidity maximum zone in a macrotidal estuary (the Gironde, France): Observations from

field and MODIS satellite data. *Estuarine, Coastal and Shelf Science*, 81(3):321–332, 2009.

David Doxaran, Jean-Marie Froidefond, and Patrice Castaing. Remote-sensing reflectance of turbid sediment-dominated waters. Reduction of sediment type variations and changing illumination conditions effects by use of reflectance ratios. *Applied Optics*, 42(15):2623–2634, 2003.

T K Edwards and G D Glysson. Field methods for measurement of fluvial sediment. *U.S.Geological Survey Open-File Report 86-531*, 1988.

M A Eleveld, R Pasterkamp, H J van der Woerd, and J D Pietrzak. Remotely sensed seasonality in the spatial distribution of sea-surface suspended particulate matter in the southern North Sea. *Estuarine, Coastal and Shelf Science*, 80(1):103–113, 2008.

Ligang Fang, Shuisen Chen, Hongqing Wang, Junping Qian, and Lixin Zhang. Detecting marine intrusion into rivers using EO-1 ALI satellite imagery: Modaomen Waterway, Pearl River Estuary, China. *International Journal of Remote Sensing*, 31(15):4125–4146, August 2010.

G Ferrier. A field study of the variability in the suspended sediment concentration-reflectance relationship. *International Journal of Remote Sensing*, 16(14):2713–2720, 1995.

GEMS. Improving Global Water Quality Monitoring: Techinial Advisor Paper No.1 United Nation Envrionmen Program-Global Envrionment Monitoring System. Technical report, 2003.

K Y H Gin, S T Koh, and I I Lin. Study of the effects of suspended marine clay on the reflectance spectra of phytoplankton. *International Journal of Remote Sensing*, 23(11), 2002.

K Y H Gin, S T Koh, and I I Lin. Spectral irradiance profiles of suspended marine clay for the estimation of suspended sediment concentration in tropical waters. *International Journal of Remote Sensing*, 24(16):3235–3245, 2003.

Mark Giordano, Z P Zhu, X M Cai, S Q Hong, X C Zhang, and Y P Xue. *Water management in the Yellow River Basin: background, current critical issues and future research needs*. IWMI, 2004.

G D Glysson, J R Gray, and L M Conge. Adjustment of Total Suspended Solids Data for Use in Sediment Studies - Building Partnerships (ASCE). *Proceeding of the ASCE*, pages 1–10, 2000.

D G Goodin, Luoheng Han, and R N Fraser. Analysis of suspended solids in water using remotely sensed high resolution derivative spectra. *Photogrammetric Engeering and Remote Sensing*, 58(4), 1993.

J R Gray, G D Glysson, and L M Turcios. *Comparability and reliability of total suspended solids and suspended-sediment concentration data*. USGS Water-Resources Investigations Rep. No. 00-4191, 2000.

Luoheng Han. Spectral reflectance with varying suspended sediment concentrations in clear and algae-laden waters. *Photogrammetric Engineering and Remote Sensing*, 63(6):701–705, 1997.

Luoheng Han and Donald C Rundquist. The response of both surface reflectance and the underwater light field to various levels of suspended sediments: preliminary results. *Photogrammetric Engineering and Remote Sensing*, 60(12):1463–1471, 1994.

Luoheng Han and Donald C Rundquist. Spectral characterization of suspended sediments generated from two texture classes of clay soil. *International Journal of Remote Sensing*, 17(3):643–649, 1996.

J Harrington and R L Repic. Hyperspectral and video remote sensing of Oklahoma lakes. In *Papers & Proceedings of Applied Geography Conferences - State University of New York at Binghamton*, pages 79–85, 1995.

J A Harrington Jr, F R Schiebe, and J F Nix. Remote sensing of Lake Chicot, Arkansas: Monitoring suspended sediments, turbidity, and Secchi depth with Landsat MSS data. *Remote Sensing of Environment*, 39(1):15–27, 1992.

F E Hoge and P E Lyon. Satellite retrieval of inherent optical properties by linear matrix inversion of oceanic radiance models: an analysis of model and radiance measurement errors. *Journal of Geophysical Research*, 101(C7):16631–16648, 1996.

Arthur J Horowitz. An evaluation of sediment rating curves for estimating suspended sediment concentrations for subsequent flux calculations. *Hydrological Processes*, 17(17):3387–3409, 2003.

M R Islam, Y Yamaguchi, and K Ogawa. Suspended sediment in the Ganges and Brahmaputra Rivers in Bangladesh: Observation from TM and AVHRR data. *Hydrological Processes*, 15(3):493–509, 2001.

Md A Islam, J Gao, W Ahmad, D Neil, and P Bell. Image calibration to like-values in mapping shallow water quality from multitemporal data. *Photogrammetric Engineering and Remote Sensing*, 69(5):567–575, 2003.

M Kaewmanee, T Choomnoommanee, and R Fraisse. Thailand Earth Observation System: Mission and Products. *Ratio*, 90:100, 2007.

S Khorram. Development of water quality models applicable throughout the entire San Francisco Bay and Delta. *Photogrammetric Engineering and Remote Sensing*, 51:53–62, 1985.

Nina E Kilham, Dar Roberts, and Michael B Singer. Remote sensing of suspended sediment concentration during turbid flood conditions on the Feather River, California—A modeling approach. *Water Resources Research*, 48(1):W01521, January 2012.

J T O Kirk. Dependence of relationship between inherent and apparent optical properties of water on solar altitude. *Limnol Oceanogr.*, 29(2):350–356, May 1984.

Lukasz Komsta. *outliers: Tests for outliers*, 2011. URL `http://CRAN.R-project.org/package=outliers`. R package version 0.14.

R G Lathrop. Use of Thematic Mapper data to assess water quality in Green Bay and central Lake Michigan. *Photogrammetric Engineering and Remote Sensing*, 52: 671–680, 1986.

R G Lathrop Jr and T M Lillesand. Monitoring water quality and river plume transport in Green Bay, Lake Michigan with SPOT-1 imagery. *Photogrammetric Engineering and Remote Sensing*, 55(3):349–354, 1989.

Zhongping Lee, Kendall L Carder, Curtis D Mobley, Robert G Steward, and Jennifer S Patch. Hyperspectral remote sensing for shallow waters. I. A semianalytical model. *Applied Optics*, 37(27):6329–6338, 1998.

Zhongping Lee, Kendall L Carder, Curtis D Mobley, Robert G Steward, and Jennifer S Patch. Hyperspectral remote sensing for shallow waters. 2. Deriving bottom depths and water properties by optimization. *Applied Optics*, 38(18):3831–3843, 1999.

Zhongping Lee, Kendall L Carder, and Robert A Arnone. Deriving inherent optical properties from water color: a multiband quasi-analytical algorithm for optically deep waters. *Applied Optics*, 41(27):5755–5772, 2002.

Carl J Legleiter, Dar A Roberts, W Andrew Marcus, and Mark A Fonstad. Passive optical remote sensing of river channel morphology and in-stream habitat: Physical basis and feasibility. *Remote Sensing of Environment*, 93(4):493–510, December 2004.

Carl J Legleiter, Dar A Roberts, and Rick L Lawrence. Spectrally based remote sensing of river bathymetry. *Earth Surface Processes and Landforms*, 34(8):1039–1059, June 2009.

Carl J Legleiter, Paul J Kinzel, and Brandon T Overstreet. Evaluating the potential for remote bathymetric mapping of a turbid, sand-bed river: 2. Application to hyperspectral image data from the Platte River. *Water Resources Research*, 47 (W09532):WR010592, September 2011.

G Li, X Li, H Wang, L Chen, and W Wen. Cross-comparison between China HJ1A-CCD and Landsat TM data. In *Geoscience and Remote Sensing Symposium (IGARSS), 2011 IEEE International*, pages 4130–4133. IEEE, 2011.

Yansui Liu, Md Anisul Islam, and Jay Gao. Quantification of shallow water quality parameters by means of remote sensing. *Progress in Physical Geography*, 27(1): 24–43, March 2003.

M A Lodhi, D C Rundquist, L Han, and M S Kuzila. The potential for remote sensing of loess soils suspended in surface waters. *Journal of the American Water Resources Association*, 33(1):111–117, 1997a.

Mahtab A Lodhi, Donald C Rundquist, Luoheng Han, and Mark S Kuzila. The Potential for Remote Sensing of Loess Soils Suspended in Surface Waters. *Journal of the American Water Resources Association*, 33(1):111–117, 1997b.

Mahtab A Lodhi, Donald C Rundquist, Luoheng Han, and Mark S Kuzila. Estimation of suspended sediment concentration in water using integrated surface reflectance. *Geocarto International*, 13(2):11–15, June 1998.

C M Long and T M Pavelsky. Remote sensing of suspended sediment concentration and hydrologic connectivity in a complex wetland environment. *Remote Sensing of Environment*, 129:197–209, 2013.

T Lorthiois, D Doxaran, and M Chami. Daily and seasonal dynamics of suspended particles in the Rhône River plume based on remote sensing and field optical measurements. *Geo-Marine Letters*, 32(2):89–101, 2012.

Wolfgang Ludwig, Jean Luc Probst, and Stefan Kempe. Predicting the oceanic input of organic carbon by continental erosion. *Global Biogeochemical Cycles*, 10(1):23–41, 1996.

R Ma and J Dai. Investigation of chlorophyll-a and total suspended matter concentrations using landsat ETM and field spectral measurement in Taihu Lake, China. *International Journal of Remote Sensing*, 26(13):2779–2795, 2005.

R Ma, J Tang, and J Dai. Bio-optical model with optimal parameter suitable for Taihu Lake in water colour remote sensing. *International Journal of Remote Sensing*, 27 (19):4305–4328, 2006a.

R Ma, J Tang, J Dai, Y Zhang, and Q Song. Absorption and scattering properties of water body in Taihu Lake, China: Absorption. *International Journal of Remote Sensing*, 27(19):4277–4304, 2006b.

A S Mahiny and B J Turner. A comparison of four common atmospheric correction methods. *Photogrammetric Engineering and Remote ...*, 2007.

A Mannino, M E Russ, and S B Hooker. Algorithm development and validation for satellite-derived distributions of DOC and CDOM in the US Middle Atlantic Bight. *Journal of Geophysical research*, 113(C7):C07051, 2008.

S Maritorena, A Morel, and B Gentili. Diffuse reflectance of oceanic shallow waters: Influence of water depth and bottom albedo. *Limnology and Oceanography*, 39(7): 1689–1703, 1994.

J M Martinez, J L Guyot, N Filizola, and F Sondag. Increase in suspended sediment discharge of the Amazon River assessed by monitoring network and satellite data. *Catena*, 79(3):257–264, December 2009.

Bunkei Matsushita and Takehiko Fukushima. Methods for retrieving hydrologically

significant surface parameters from remote sensing: a review for applications to east Asia region. *Hydrological Processes*, 23(4):524–533, February 2009.

John D Milliman and Robert H Meade. World-wide delivery of river sediment to the oceans. *The Journal of Geology*, pages 1–21, 1983.

Ministry of Water Resources of China. *Code for measurements of suspended sediment in open channels (GB50159-92)*. GB 50159-92. China Planning Press, Beijing, 1992.

Curtis D Mobley and Charles D Mobley. *Light and water: Radiative transfer in natural waters*, volume 592. Academic press San Diego, CA, 1994.

P F Moreira-Turcq, P Seyler, J L Guyot, and H Etcheber. Characteristics of organic matter in the mixing zone of the Rio Negro and Rio Solimões of the Amazon River. *Hydrological Processes*, 17(7):1393–1404, 2003.

A Morel and S Maritorena. Bio-optical properties of oceanic waters- A reappraisal. *Journal of Geophysical research*, 106(C4):7163–7180, 2001.

A Morel and L Prieur. Analysis of variations in ocean color. *Limnology and Oceanography*, 22:709–722, 1977.

Andre Morel, Bernard Gentili, Herve Claustre, Marcel Babin, Annick Bricaud, Ras Josephine, and Fanny Tieche. Optical properties of the "clearest" natural waters. *Limnology and Oceanography*, 2(1):217–219, September 2007.

E M M Novo, J D Hansom, and P J Curran. The effect of viewing geometry and wavelength on the relationship between reflectance and suspended sediment concentration. *International Journal of Remote Sensing*, 10(8):1357–1372, 1989a.

EMM Novo, J D Hansom, and P J Curran. The effect of sediment type on the relationship between reflectance and suspended sediment concentration. *International Journal of Remote Sensing*, 10(7):1283–1289, 1989b.

Evlyn Márcia Leão Moraes Novo, Carlos Alberto Steffen, and Cláudia Zuccari Fernandes Braga. Results of a laboratory experiment relating spectral reflectance to total suspended solids. *Remote Sensing of Environment*, 36(1):67–72, 1991.

M Onderka and M Rodný. Can suspended sediment concentrations be estimated from multispectral imagery using only image-derived information? *Journal of the Indian Society of Remote Sensing*, 38(1):85–97, 2010.

Sylvain Ouillon, Pascal Douillet, Anne Petrenko, Jacques Neveux, Cécile Dupouy, Jean-Marie Froidefond, Serge Andréfouët, and Alain Muñoz-Caravaca. Optical Algorithms at Satellite Wavelengths for Total Suspended Matter in Tropical Coastal Waters. *Sensors*, 8(7):4165–4185, July 2008.

Y Oyama, B Matsushita, T Fukushima, T Nagai, and A Imai. A new algorithm for estimating chlorophyll aconcentration from multispectral satellite data in case II waters: a simulation based on a controlled laboratory experiment. *International Journal of Remote Sensing*, 28(7):1437–1453, April 2007.

Y Oyama, Y Oyama, B Matsushita, B Matsushita, T Fukushima, T Fukushima, J Chen, T Nagai, and A Imai. Testing the spectral decomposition algorithm (SDA) for different phytoplankton species by a simulation based on tank experiments. *International Journal of Remote Sensing*, 31(6):1605–1623, 2010.

Youichi Oyama, Bunkei Matsushita, Takehiko Fukushima, Kazuo Matsushige, and Akio Imai. Application of spectral decomposition algorithm for mapping water

quality in a turbid lake (Lake Kasumigaura, Japan) from Landsat TM data. *ISPRS Journal of Photogrammetry and Remote Sensing*, 64(1):73–85, January 2009.

Chongguang Pang, Wei Yu, Yang Yang, and Danxiu Han. An improved method for evaluating the seasonal variability of total suspended sediment flux field in the Yellow and East China Seas. *International Journal of Sediment Research*, 26(1): 1–14, April 2011.

Tamlin M Pavelsky and Laurence C Smith. Remote sensing of suspended sediment concentration, flow velocity, and lake recharge in the Peace-Athabasca Delta, Canada. *Water Resources Research*, 45:W11417, January 2009.

Jun Peng, Shenliang Chen, and Ping Dong. Temporal variation of sediment load in the Yellow River basin, China, and its impacts on the lower reaches and the river delta. *Catena*, 83(2-3):135–147, November 2010.

Liqin Qu, Tingwu Lei, Duihu Ning, Daniel Civco, and Xiusheng Yang. Spectral Mixing Algorithm for Quantifying Suspended Sediment Concentration in the Yellow River: Simulation based on Controlled Laboratory Experiment. *International Journal of Remote Sensing*, 2014, Under Review.

R Core Team. *R: A Language and Environment for Statistical Computing*. R Foundation for Statistical Computing, Vienna, Austria, 2013. URL `http://www.R-project.org/`.

R Raaj, M Ramalingam, S K Ghosh, and U C Kothyari. Mapping of suspended sediments using site specific seasonal algorithms. *Journal of the Indian Society of Remote Sensing*, 36(1):61–68, 2008.

J C Ritchie and C M Cooper. Comparison of measured suspended sediment concentrations with suspended sediment concentrations estimated from Landsat MSS data. *International Journal of Remote Sensing*, 9(3):379–387, 1988.

J C Ritchie, F R Schiebe, and J R McHenry. Remote sensing of suspended sediments in surface waters. *Journal of American Society of Photogrammetry*, 42(12):1539–1545, 1976.

J C Ritchie, P V Zimba, and J H Everitt. Remote sensing techniques to assess water quality. *Photogrammetric Engineering and Remote Sensing*, 69(6):695–704, 2003.

Jerry C Ritchie and Charles M Cooper. Algorithm for estimating surface suspended sediment concentrations with Landsat MSS digital data. *Water Resources Bulletin*, 27(3):373–379, 1991.

Jerry C Ritchie, Charles M Cooper, and Jiang Yongqing. Using landsat multispectral scanner data to estimate suspended sediments in Moon Lake, Mississippi. *Remote Sensing of Environment*, 23(1):65–81, October 1987.

Jerry C Ritchie, Charles M Cooper, and Frank R Schiebe. The relationship of MSS and TM digital data with suspended sediments, chlorophyll, and temperature in Moon Lake, Mississippi. *Remote Sensing of Environment*, 33(2):137–148, August 1990.

C S Roeslerl and M J Perry. In situ phytoplankton absorption, fluorescence emission, and particulate backscattering spectra determined from. *Journal of Geophysical research*, 100(C7):13–279–13–294, 1995.

C M Rudorff, E M L M Novo, and L S Galvão. Spectral mixture analysis of inland tropical amazon floodplain waters using EO-1 hyperion. In *International Geoscience and Remote Sensing Symposium (IGARSS)*, pages 128–133. IEEE, 2006.

Federico Santini, Luigi Alberotanza, Rosa Maria Cavalli, and Stefano Pignatti. A two-step optimization procedure for assessing water constituent concentrations by hyperspectral remote sensing techniques: An application to the highly turbid Venice lagoon waters. *Remote Sensing of Environment*, 114(4):887–898, April 2010.

F R Schiebe, J A Harrington Jr, and J C Ritchie. Remote sensing of suspended sediments: the Lake Chicot, Arkansas project. *International Journal of Remote Sensing*, 13(8):1487–1509, 1992.

T J Schmugge, W P Kustas, J C Ritchie, T J Jackson, and A Rango. Remote sensing in hydrology. *Advances in Water Resources*, 25(8-12):1367–1385, 2002.

R C Smith and K S Baker. Optical properties of the clearest natural waters(200-800 nm). *Applied Optics*, 20(2):177–184, 1981.

R P Stumpf and J R Pennock. Calibration of a general optical equation for remote sensing of suspended sediments in a moderately turbid estuary. *Journal of Geophysical research*, 94(C10):14363–14–371, 1989.

R P Stumpf and J R Pennock. Remote estimation of the diffuse attenuation coefficient in a moderately turbid estuary. *Remote Sensing of Environment*, 38(3):183–191, 1991.

E Sváb, A N Tyler, T Preston, M Présing, and K V Balogh. Characterizing the

spectral reflectance of algae in lake waters with high suspended sediment concentrations. *International Journal of Remote Sensing*, 26(5):919–928, 2005.

M Sydor and R A Arnone. Effect of suspended particulate and dissolved organic matter on remote sensing of coastal and riverine waters. *Applied Optics*, 36(27): 6905–6912, 1997.

J P Syvitski, M D Morehead, D B Bahr, and T Mulder. Estimating fluvial sediment transport: The rating parameters. *Water Resources Research*, 36(9):2747–2760, 2000.

S Tassan. Local algorithms using SeaWiFS data for the retrieval of phytoplankton, pigments, suspended sediment, and yellow substance in coastal waters. *Applied Optics*, 33(12):2369–2378, 1994.

S Tassan and R Sturm. An algorithm for the retrieval of sediment content in turbid coastal waters from CZCS data. *International Journal of Remote Sensing*, 7(5): 643–655, 1986.

B J Topliss, C L Almos, and P R Hill. Algorithms for remote sensing of high concentration, inorganic suspended sediment. *International Journal of Remote Sensing*, 11(6):947–966, 1990.

A N Tyler, E Sváb, T Preston, M Présing, and W A Kovács. Remote sensing of the water quality of shallow lakes: A mixture modelling approach to quantifying phytoplankton in water characterized by high-suspended sediment. *International Journal of Remote Sensing*, 27(8):1521–1537, 2006.

R Espinoza Villar, J M Martinez, J L Guyot, P Fraizy, E Armijos, A Crave, H Bazán, P Vauchel, and W Lavado. The integration of field measurements and satellite observations to determine river solid loads in poorly monitored basins. *Journal of Hydrology*, 444-445:221–228, 2012.

V Volpe, S Silvestri, and M Marani. Remote sensing retrieval of suspended sediment concentration in shallow waters. *Remote Sensing of Environment*, 2011.

A Vrieling. Satellite remote sensing for water erosion assessment: A review. *Catena*, 65(1):2–18, 2006.

D E Walling and D Fang. Recent trends in the suspended sediment loads of the world's rivers. *Global and Planetary Change*, 39:111–126, 2003.

D E Walling, A L Collins, and R W Stroud. Tracing suspended sediment and particulate phosphorus sources in catchments. *Journal of Hydrology*, 350(3-4):274–289, 2008.

F Wang, B Zhou, J Xu, L Song, and X Wang. Application of neural network and MODIS 250 m imagery for estimating suspended sediments concentration in Hangzhou Bay, China. *Environmental Geology*, 56(6):1093–1101, 2009a.

Fan Wang, Bin Zhou, Xingmei Liu, Gendi Zhou, and Keli Zhao. Remote-sensing inversion model of surface water suspended sediment concentration based on in situ measured spectrum in Hangzhou Bay, China. *Environmental Earth Sciences*, 67(6):1669–1677, February 2012.

G Wang, J Qian, G Cheng, and Y Lai. Eco-environmental degradation and causal

analysis in the source region of the Yellow River. *Environmental Geology*, 40(7): 884–890, 2001.

Houjie Wang, Zuosheng Yang, Naishuang Bi, and Haidong Li. Rapid shifts of the river plume pathway off the Huanghe (Yellow) River mouth in response to water-sediment regulation scheme in 2005. *Chinese Science Bulletin*, 50(24):2878–2884, 2005.

Houjie Wang, Zuosheng Yang, Yoshiki Saito, J Paul Liu, Xiaoxia Sun, and Yan Wang. Stepwise decreases of the Huanghe (Yellow River) sediment load (1950–2005): Impacts of climate change and human activities. *Global and Planetary Change*, 57(3-4):331–354, June 2007.

J J Wang and X X Lu. Estimation of suspended sediment concentrations using Terra MODIS: An example from the Lower Yangtze River, China. *Science of The Total Environment*, 408(5):1131–1138, February 2010.

J J Wang, X X Lu, S C Liew, and Y Zhou. Remote sensing of suspended sediment concentrations of large rivers using multi-temporal MODIS images: an example in the Middle and Lower Yangtze River, China. *International Journal of Remote Sensing*, 31(4), 2010.

Jian Jun Wang, Xi Xi Lu, Soo Chin Liew, and Yue Zhou. Retrieval of suspended sediment concentrations in large turbid rivers using Landsat ETM+: an example from the Yangtze River, China. *Earth Surf Process Landforms*, 34(8):1082–1092, June 2009b.

Menghua Wang, Wei Shi, and Junwu Tang. Water property monitoring and assess-

ment for China's inland Lake Taihu from MODIS-Aqua measurements. *Remote Sensing of Environment*, 115(3):841–854, March 2011.

J A Warrick, LAK Mertes, and D A Siegel. Estimating suspended sediment concentrations in turbid coastal waters of the Santa Barbara Channel with SeaWiFS. *International Journal of Remote Sensing*, 25(10):1995–2002, 2004.

Jonathan A Warrick, Paul M DiGiacomo, Stephen B Weisberg, Nikolay P Nezlin, M Mengel, Burton H Jones, J Carter Ohlmann, Libe Washburn, Eric J Terrill, and Katie L Farnsworth. River plume patterns and dynamics within the Southern California Bight. *Continental Shelf Research*, 27(19):2427–2448, 2007.

D G Wren, B D Barkdoll, R A Kuhnle, and R W Derrow. Field techniques for suspended-sediment measurement. *Journal of Hydraulic Engineering*, 126(2):97–104, 2000.

Dawen Yang, Chong Li, Heping Hu, Zhidong Lei, Shixiu Yang, Tetsuya Kusuda, Toshio Koike, and Katumi Musiake. Analysis of water resources variability in the Yellow River of China during the last half century using historical data. *Water Resources Research*, 40(W06502):WR002763, 2004.

Yellow River Conservancy Commission. Statistis of flow and sediments measurements from the major hydrological stations in the Yellow River Basin (1919-1951,1991-1998). March 2011.

Zhifeng Yu, Xiaoling Chen, Bin Zhou, Liqiao Tian, Xiaohong Yuan, and Lian Feng. Assessment of total suspended sediment concentrations in Poyang Lake using HJ-1A/1B CCD imagery. *Chinese Journal of Oceanology and Limnology*, 30(2):295–304, March 2012.

You Yuming and Hou Min. Remote sensing analysis of the suspended sediment transport in Lingdingyang. *China Ocean Engineering*, 6(3):331–349, 1992.

D G Zawada, C Hu, T Clayton, Z Chen, J C Brock, and F E Muller-Karger. Remote sensing of particle backscattering in Chesapeake Bay: A 6-year SeaWiFS retrospective view. *Estuarine, Coastal and Shelf Science*, 73(3):792–806, 2007.

L J Zhang, L Wang, W J Cai, D M Liu, and Z G Yu. Impact of human activities on organic carbon transport in the Yellow River. *Biogeosciences*, 10(4):2513–2524, 2013.

W Zhou, S Wang, Y Zhou, and A Troy. Mapping the concentrations of total suspended matter in Lake Taihu, China, using Landsat-5 TM data. *International Journal of Remote Sensing*, 27(6):1177–1191, 2006.

W Zhu, Q Yu, Y Q Tian, R F Chen, and G B Gardner. Estimation of chromophoric dissolved organic matter in the Mississippi and Atchafalaya river plume regions using above-surface hyperspectral remote sensing. *Journal of Geophysical research*, 116(C2):C02011, 2011.